ELECTRICAL, OPTICAL AND ACOUSTIC DIAGNOSTICS OF ATMOSPHERIC PRESSURE GAS DISCHARGES

A thesis for the degree of

PHILOSOPHIAE DOCTOR

Presented to

DUBLIN CITY UNIVERSITY

By

Níall O'Connor
School of Electronic Engineering
Dublin City University

Research Supervisor:

Dr. Stephen Daniels

External Examiner: Dr. James L. Walsh
Internal Examiner: Prof. Patrick J. McNally

April 2011

Declaration

I hereby certify that this material, which I now submit for assessment on the programme of study leading to the award of Philosophiae Doctor is entirely my own work, that I have exercised reasonable care to ensure that the work is original, and does not to the best of my knowledge breach any law of copyright, and has not been taken from the work of others save and to the extent that such work has been cited and acknowledged within the text of this work.

....

Níall O'Connor, 19th April 2011

Abstract

This thesis presents original diagnostic investigations of atmospheric pressure gaseous discharges, operating in flowing helium and helium with low concentrations (0.1 - 1 %) of gas admixtures, together with novel biomedical surface functionalisations.

The initial body of this work focuses on comprehensive electrical and optical diagnostics of the operation of an industrial scale dielectric barrier discharge (DBD), maintained in a 10 l/min flow of both helium and helium with 1% admixed oxygen. The experimental results reveal a coupling between the power dissipated in the discharge and the discharge homogeneity which, in turn, correlates to a shift in the power supply operating frequency and species optical emission intensities. The shift in the operating frequency is shown to be dependent upon increased charge deposition on the electrodes, as the input power is increased, thus changing the overall system capacitance through charge-voltage LIssajous figure analyses. Furthermore it is demonstrated that the gas temperature did not exceed approximately 380-410 K over the full parameter space, in the helium discharge, through model fitting of the first negative system of the N_2^+ band around 391.4 nm.

A real-time, PC based monitoring diagnostic system has been developed which is used to perform long term analyses of a laboratory DBD chamber in helium and helium with 0.1% admixtures of both oxygen and nitrogen. Post analysis of the results, through multivariate analysis of the large experimental datasets, show that rapid system characterisations are faciltated using this method, the outcomes of which are compared with both global and fluid model outputs within the literature.

Passive acoustic diagnostics of a plasma jet system, together with signal analysis in the time, frequency and time-frequency domains are explored. Here it is found that flow induced mode transitions from buoyant, through laminar, to turbulent regimes may be identified using time-frequency scalogram plots. It is shown that the scalogram plots may also be used to identify the point at which power coupling together with the plume length are maximised. The transition into a fully turbulent plume structure is shown to be accompanied by low frequency acoustic signals which modulate the acoustic first harmonic in the time-frequency domain. Moreover, a non invasive measurement of the power coupled into the discharge is demonstrated through passive acoustic sensing whilst the jet flow is laminar.

Finally, surface modifications of disposable plastics for biosensor applications are performed. In this work it is shown that the density of packing of both 40 nm and 80 nm gold nanoparticles may be tailored, through variation of the gas input flow rate of a linear field jet, in order to enhance the optical signal according to the Mie theory for light extinction at a metal nanoparticle interface. The functionalisation using long chain polethyleneglycol has also been demonstrated to provide a protein repellent surface for non-specific protein binding reduction.

Acknowledgments

The are numerous people whom I wish to acknowledge without whose support this thesis would not have been possible.

Foremost, I wish to thank my supervisor, Dr. Stephen Daniels, for his tireless support, both academic and moral, throughout the past four years.

I have benefited greatly from input from my fellow students and academic members in the N.C.P.S.T. and School of Electronic Engineering. Discussions with Dr. Muhammad Iqbal, Dr. Vic Law, Dr. Vladimir Milosavljević, Dr. Bernard Keville, Prof. Miles Turner, Dr. Jim Conway, Dr. Felipe Soberon, Prof. Paddy McNally and Mossey Kelly have been particularly fruitful.

Also, I wish to thank those who facilitated and contributed to work carried out at the School of Mechanical Engineering at U.C.D.: Dr. Denis Dowling, Dr. Barry Twomey, Dr. John Tynan and Dr. Amsarani Ramamoorthy.

My work was greatly aided by the technical team at the university. For this I thank James Lalor, Pat Wogan, Billy Roarty, Robert Clare and Liam

Meany.

I would like to thank also, my brothers, Stephen and Christopher, and sister, Sinead, for their great support and putting up with me over the years. To Joanne, thank you for your understanding and patience!

Finally, I would like to thank my mother, Patricia, whose continued support and endless encouragement has guided me through my life.

THE THOUGHT-FOX (Ted Hughes - 1957)

I imagine this midnight moments forest:
Something else is alive
Beside the clocks loneliness
And this blank page where my fingers move.

Through the window I see no star:
Something more near
Though deeper within darkness
Is entering the loneliness:

Cold, delicately as the dark snow,
A foxs nose touches twig, leaf;
Two eyes serve a movement, that now
And again now, and now, and now

Sets neat prints into the snow
Between trees, and warily a lame
Shadow lags by stump and in hollow
Of a body that is bold to come

Across clearings, an eye,
A widening deepening greenness,
Brilliantly, concentratedly,
Coming about its own business

Till, with a sudden sharp hot stink of fox
It enters the dark hole of the head.
The window is starless still; the clock ticks,
The page is printed.

Contents

List of Figures

List of Tables

Nomenclature

Acronyms

AFM : Atomic Force Microscope

APD : Atmospheric Pressure Discharge

APGD : Atmospheric Pressure Glow Discharge

APLFJ : Atmospheric Pressure Linear Field Jet

APP : Atmospheric Pressure Plasma

APPJ : Atmospheric Pressure Plasma Jet

DBD : Dielectric Barrier Discharge

EEDF : Electron Energy Distribution Function

FD : Filamentary Discharge

FNS : First Negative System

FWHM : Full Width at Half Maximum

GPIB	:	General Purpose Interface Bus
GUI	:	Graphical User Interface
ICCD	:	Intensified Charge Coupled Detector
IR	:	Infra Red
MFC	:	Mass Flow Controller
MOSFET	:	Metal Oxide Semiconductor Field Effect Transistor
NP	:	Nanoparticle
OAUGDP	:	One Atmosphere Uniform Glow Discharge Plasma
OES	:	Optical Emission Spectroscopy
PDP	:	Plasma Display Panel
PECVD	:	Plasma Enhanced Chemical Vapour Deposition
PEG	:	Poly (ethylene glycol)
PET	:	Poly (ethylene teraphthalate)
PMT	:	Photomultiplier Tube
SEM	:	Scanning Electron Microscope
SPR	:	Surface Plasmon Resonance
SPS	:	Second Positive System
STFT	:	Short Term Fourier Transform
UV	:	Ultraviolet
UV-VIS	:	Ultraviolet-Visible
VUV	:	Vacuum Ultraviolet
WT	:	Wavelet Transform

CHAPTER 1

Introduction

1.1 Introduction and motivation

Owing to the need for more economic and ecologically sound processing technologies in the biomedical, textile, aerospace, agricultural and food handling industries, there has been somewhat of a renaissance in the use of Atmospheric Pressure Plasmas (APPs) to generate active species which may be beneficial to the processes of sterilization, decontamination and enhancement of materials [1, 2]. Some of the main criteria driving the resurgence are listed below [2].

- APPs do not require expensive vacuum equipment, as in the case of low pressure plasma systems.
- They may be operated in open air, allowing continuous feed processing.

- A versatile variety of configurations, types and geometries are available to meet the needs of specific applications. For instance the reel to reel One Atmosphere Uniform Glow Discharge Plasma (OAUGDP™) for polymer web processing [3] and the handheld plasma torch [4], used in biomedical applications.

This proliferation in the exploitation of APPs necessitates the provision of diagnostics, that are flexible and of low cost, to coincide with the criteria presented above. A particularly attractive quality of a plasma diagnostic methodology is that it be non-invasive i.e. the methodology does not cause a disturbance to the operation of the plasma system; such is the case when electrical probes are used [5]. Current and voltage monitoring, optical emission spectroscopy (OES) and passive acoustic sensing are diagnostic approaches which meet such demands. Also, given the versatility of open air plasma treatments and the absence of the necessity of vacuum equipment, new avenues in plasma surface modifications may be exploited.

1.2 Thesis contributions

In this thesis the aforementioned diagnostic methodologies are employed to gain a better understanding of the operation of various atmospheric pressure plasma devices. An addition to this work is the use of APPs to produce novel biomedical sensor surface modifications. The contributions from this work are as follows:

1.2 Thesis contributions

1. A comprehensive electrical and optical characterisation of an industrial scale APP system has been performed. Whilst the literature contains a large body of such characterisations on experimental APP devices, there has been little work on industrial scale APPs. In general these systems are less versatile than laboratory plasmas and therefore must be operated within well defined windows in order to facilitate process outcomes. The outcomes of this work show that the discharge spatial homogeneity is determined by the power coupled into the discharge and charge deposition on the electrodes which in turn influences the discharge chemistry. Furthermore, it is shown, through high resolution optical emission spectroscopy, that the gas temperature in a helium discharge does not exceed approx. 380-410 K. These results are useful in defining process windows in which particular future surface treatments may be performed.

2. A, PC based, real time monitor and multivariate method for performing electrical (current/voltage) and optical (OES) investigations of APPs has been developed. Within the literature, investigations into the performance of APP systems are generally confined to post analysis of the experimental results and the use of bivariate methods. The results of the experiments show that the trends associated with the coupling between the electrical and optical parameters (and hence the discharge chemistry) of a laboratory dielectric barrier discharge (DBD) are effi-

ciently and succinctly revealed, through the application of the diagnostic methodology, in long term analyses of helium, helium/nitrogen and helium/oxygen discharges. It is also shown that the method facilitates comparisons between fluctuations in these parameters of each of the individual discharge chemistries.

3. Novel passive acoustic diagnostics together with modern, time-frequency, signal processing techniques have been used in the analysis of the performance of an atmospheric pressure plasma jet (APPJ) device. Here it shown that flow mode transitions and the point of maximal power coupling are easily identified using time-frequency scalograms as opposed to conventional Fourier transformations. It is further demonstrated that remote power measurements of plasma jets are made possible, using time domain acoustic sensing, whilst the jet flow is laminar.

4. The final outcomes of this thesis demonstrate that an APPJ device may be used to modify plastic surfaces for biosensing applications. Tailoring of the plasmonic enhancement of a disposable plastic has been demonstrated by varying the surface density of packing of aerosol injected gold nanoparticle colloids. The retention of the protein repellent properties of surface deposited long chain polyethylene glycol (PEG1000) has further been demonstrated in this work also.

1.3 Structure of the thesis

The thesis is structured as follows. The proceeding chapter provides a discussion of the elementary physics and chemistry of atmospheric pressure gas discharges and their classifications. Chapter three describes the APP laboratory systems which were designed for the course of this work. Chapters four through seven present investigations and results of the methods outlined in the previous section. Finally, in chapter eight, conclusions are drawn and future developments discussed.

CHAPTER 2

Atmospheric pressure gaseous discharges

2.1 Introduction

The term plasma was coined by Irving Langmuir in 1928 [6] and is often referred to as the fourth state of matter. As temperature input to a substance is increased, molecules and or atoms within the substance become more energetic and phase transformation occurs in the sequence: solid, liquid, gas and then to plasma. In the latter stages, molecules in the gas dissociate to form a gas of atoms and then a gas of freely moving charged particles, electrons and positive ions. The plasma state is characterized by a mixture of electrons, ions, and neutral particles moving in random directions that, on average, is electrically neutral (i.e. the number of electrons $n_e \cong n_i$, the number of ions).

In addition, plasmas are electrically conducting due to the presence of these free-charge carriers and can attain electrical conductivities larger than those of metals such as gold and copper [7].

The plasma state is the most abundant state of matter found in nature. Commonly observed plasmas include Aurora Borealis and lightning, whilst the sun is in effect a huge ball of plasma. Plasmas are generally classified according to their level of ionization (electron or ion density) and the temperature (energy) of the electrons and neutrals [2, 8]. In general, the electrons, due to their much smaller mass, approximately 1/1900 times that of a proton, have energies far greater than those of the ionic or neutral species. This means they can participate in highly energetic reactions with the supporting gas whilst the gas temperature remains extremely low and often close to room temperature. Figure 2.1 details the classification of different plasmas according to electron densities and temperatures. The atmospheric pressure plasmas of interest within this thesis are glow type discharges, with electron densities in the range of 10^8 to 10^{13} cm^{-3} and electron temperatures of between 1 and 8 eV (1 eV ~ 11,000 K). Since the electron density is extremely low with respect to the gas density (~ 10^{19} cm^{-3}) in these discharges, the collisions of high energy electrons with the background gas are not enough to bring about thermodynamic equilibrium and the gas remains cold. Discharges of this kind are extremely important when temperature sensitive materials are involved. However, as the electron density becomes comparable to the gas density, an arc is formed (another commonly observed plasma) which represents a plasma

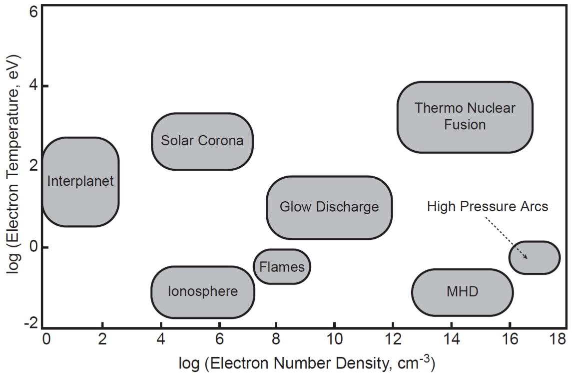

Figure 2.1: *Nomenclature of different plasma states with respect to electron temperature and electron density on a log - log scale*

which is very close to thermodynamic equilibrium (c.f. right side of figure 2.1).

Plasmas offer two main characteristics for practical applications. They can have temperatures and energy densities greater than those produced by ordinary chemical means. Furthermore, plasmas can produce energetic species that can initiate chemical reactions difficult or impossible to obtain using ordinary chemical mechanisms. The energetic species generated are numerous, e.g. charged particles (electrons and ions), atomic and molecular radicals, highly reactive neutral species such as reactive atoms (e.g., O, F, etc.), excited atomic states, reactive molecular fragments and photons of energies ranging from the far IR to VUV. The plasma produced species can then be utilised to participate in chemical and physical reactions with their surrounding environment e.g. gases or solid substrates [1, 7, 9, 10] and in the production of radiation for discharge lamps and lasers [11].

Applications of plasma can provide major benefits over existing material treatment methods. Often, processes can be performed that are not possible in any other manner. Plasma can provide an efficiency increase in processing methods and very often can reduce environmental impact in comparison to more conventional processes.

However, traditional plasma treatments and applications have generally been performed at pressures much lower than atmospheric pressure, which necessitates the use of expensive vacuum equipment and excludes continuous treatment of substrates over batch treatment [1, 12, 13]. Therefore, the replacement of such systems with those which operate at atmospheric pressure in open air environments represents an extremely attractive alternative to current plasma industries [10]. The transition to generation of plasmas at atmospheric pressure is not easy though. The low density and reduced collisions of hot electrons at low pressure makes it relatively easy to sustain nonthermal plasmas whereas, at atmospheric pressure, collisions of hot electrons are much increased which greatly increases the possibility of arc formation. Furthermore, high voltages are necessary to facilitate breakdown also.

In order to classify and diagnose atmospheric pressure gaseous discharges, it is critical to understand the discharge breakdown mechanisms, volt-ampere characteristics and the physical and chemical processes which result. Therefore the following sections seek to elucidate these concepts as they shall be discussed in further chapters.

2.2 Physics and chemsitry of gas discharge breakdown

2.2.1 Electron avalanche formation

In reality the electrical breakdown of a gaseous medium is, generally, a complex, multistage phenomenon but can be explained by the following idealised experiment shown in figure 2.2. In figure 2.2 a DC power supply of voltage V is connected across two electrodes separated by a gap distance d. The gap is filled with an ideal, pure gas at pressure P. The gas will usually contain a certain amount of 'seed' electrons which are generated by background ionization processes such as cosmic radiation [14]. These electrons are subject to an acceleration, in the direction away from the cathode, due to the applied

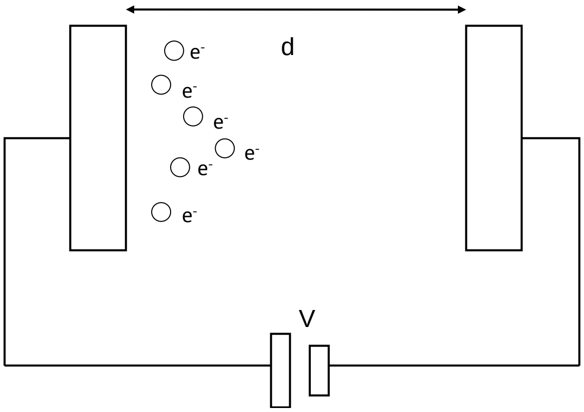

Figure 2.2: *Schematic of gas discharge breakdown*

electric field E (which is considered uniform) given by

$$E = \frac{V}{d} \tag{2.1}$$

The velocity of the electrons is determined by both the directed motion due to the applied field and a random thermal motion due to collisions with the gas molecules. The net velocity, due to the applied field, is known as the drift velocity, v_d where:

$$v_d = -\mu E \tag{2.2}$$

The symbol μ is the mobility of the electron, which is a function of the pressure and hence the density n_0 of the background gas.

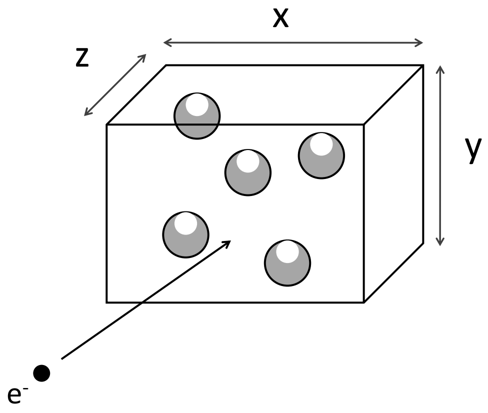

Figure 2.3: *Electron collision with background gas*

Next we consider the situation where an electron is travelling through a volume of neutral gas atoms (see figure 2.3). Here we take the gas atoms to be stationary with respect to the impinging electron. A volume xyz of gas will contain $n_0 \times xyz$ atoms, each of cross section $\sigma = \pi r^2$, where r is the atomic radius. In this idealised situation, a collision will occur between an electron and a gas atom when the z axis extends as far as λ_m, the electron mean free path between collisions (less than 1 μm at atmospheric pressure in helium). At this point a surface xy will be virtually obscured by gas atoms, thus we have [15]:

$$n_0 xy \lambda_m \sigma = xy \tag{2.3}$$

or

$$\lambda_m = \frac{1}{\sigma n_0} \tag{2.4}$$

If the kinetic energy, T, gained by the electron is at or above the the energy required to ionize a neutral atom , V_i, an electron may be released from the atom. Such electrons may be accelerated by the applied field to create further ionization events leading to a multiplication of electrons or an *electron avalanche* which evolves in both space and time [2, 16]. This process is depicted in figure 2.4 [15].

2.2.2 Townsend Breakdown

The number of ionization events per unit length by electron impact, α, is, in general, a function of the type of gas,the gas pressure and the applied electric field and was determined semi-empirically by Townsend, giving the following formula

$$\alpha = pAexp({-}^{Bp}/_{E}) \tag{2.5}$$

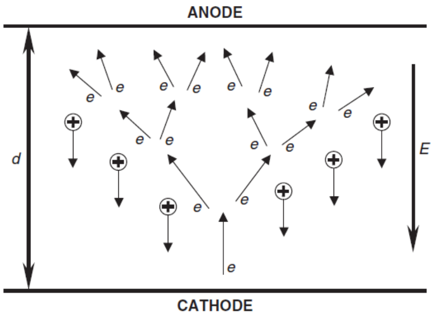

Figure 2.4: *Electron avalanche multiplication*

where A and B are specific to the type of gas and α is the *Townsend ionization coefficient* [14, 15]. The production of electrons along the direction of the electric field with respect to the axial distance from the cathode is given by

$$\frac{dne}{dx} = \alpha n_e \tag{2.6}$$

n_e being the number of electrons created along the gas gap length. Integration of 2.6 leads to

$$n_e(x) = n_{e0} exp(\alpha x) \tag{2.7}$$

where n_{e0} is the initial number of electrons present in the gas.

As electron avalanches propagate through the gas, ionization leads to the production of ions which are accelerated by the applied field towards the cathode. Ion bombardment of the cathode can lead to secondary emission of electrons, which cause further avalanching through the discharge gas due to acceleration by the externally applied field. The discharge becomes self sustaining if the amount of secondary electrons produced by these avalanches exactly balances the amount of ions lost to the cathode i.e.

$$\gamma n_{e0}[exp(\alpha d) - 1] = n_{e0} \tag{2.8}$$

or

$$\alpha d = ln(1 + {}^{1}\!/\!{}_{\gamma}) \tag{2.9}$$

In equations 2.8 and 2.9, γ is the *secondary electron emission coefficient* [14, 15]. If we take the planar geometry shown in figure 2.2 then for the breakdown voltage, V_b we get $V_b = Ed$, thus combining equations 2.5 and 2.9 we get the Paschen's Law for gas discharges [17]

$$V_b = \frac{Bpd}{ln(Apd) - ln[ln(1 + \gamma^{-1})]} \tag{2.10}$$

The characteristic curve for electrical breakdown of argon (A = 13 mm^{-1}Torr^{-1},

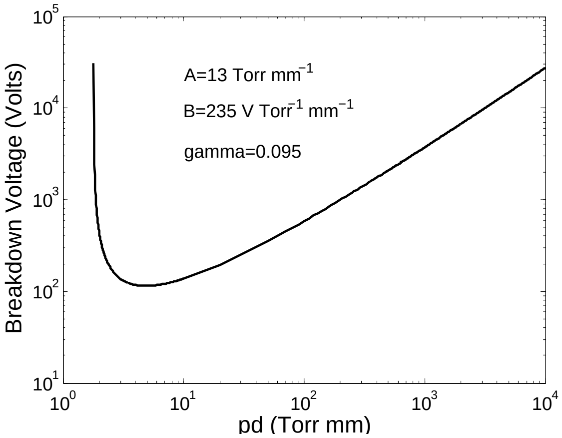

Figure 2.5: *Calculated Paschen curve for argon*

B = 235 $\text{Vcm}^{-1}\text{Torr}^{-1}$ and $\gamma \approx 10^{-2}$) is shown in figure 2.5. It can be seen that at low *pd* values, the gas is almost in the state of a vacuum and so the breakdown voltage goes to infinity (no collisions of the electrons with the background gas can occur). The curve reaches a minimum where the ideal gas breakdown conditions are realised and then rises as the gas becomes more dense and hence behaves more as an insulator [14, 17]. Usually, gaseous discharges are formed and operated around the curve minimum in figure 2.5 (the Stoletov point [8]), which corresponds to the optimal power efficiency (minimum breakdown voltage) in creating and sustaining the Townsend discharge.

2.2.3 Spark and streamer breakdown of gases

The theory of gas breakdown in the previous section generally applies to gas gaps with low *Pd* values; however, experiments in the 1930s and 1940s [18] had shown that a new model was required for the breakdown mechanism at *Pd* values greater than 200 torr cm (values typical of atmospheric pressure discharges). It was found that the time lag from breakdown to the formation of conducting gas could not be explained by the ion dominated plasma development mechanism of the Townsend theory [14, 19]. In 1940, J. M. Meek developed a new theory to elucidate the formation of such discharges [18]. In the so called ‘streamer’ theory, the electric fields generated by the electron avalanche must be considered due to the large space charges developed at high Pd values. The development of such a discharge is shown in figure 2.6 [20].

The field generated by the electron avalanche head begins to modify the field

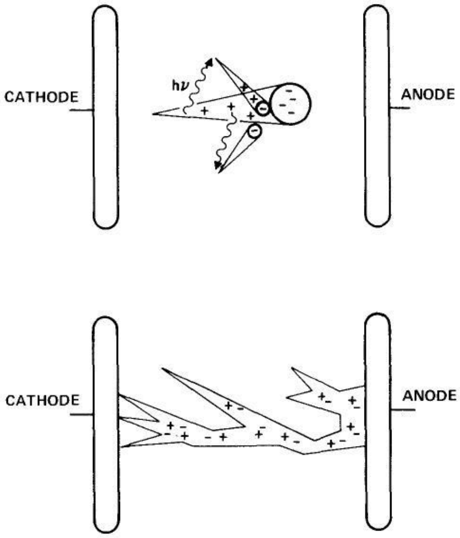

Figure 2.6: *Streamer breakdown in APDs at high pd values*

across the gap before the avalanche reaches the anode. If the space charge field due to the charge head is taken to be spherical we have

$$E = \frac{Qe}{4\pi\epsilon_0 r^2} \tag{2.11}$$

where e is the elementary charge, Q the number of charges in the head, r its radius and ϵ_0 the relative permittivity of the gas. The radius, r, of the avalanche is related to the time, t, after the initiation of the avalanche and the diffusion coefficient, D, by Raether [14]

$$r = \sqrt{4Dt} \tag{2.12}$$

When the field generated by the electron avalanche becomes comparable to or greater than the applied field, secondary avalanches can develop in front of the streamer head and outside of the streamer due to photoionisation, causing the rapid development of a highly conducting channel (see figure 2.6). The criterion for such a streamer or filament to develop is known as the *Raether criterion* given by [20]

$$\frac{\alpha d_{crit}}{p} = 20 + ln(d_{crit}) \tag{2.13}$$

Where d_{crit} is the critical distance the avalanche head must travel to form a streamer filament and is determined by the gas type [20]. The speed of streamer formation is of the order of 10^6 ms^{-1}, close to the electron drift velocity, whereas discharges involving the Townsend mechanism proceed at speeds in the region of 10^3 ms^{-1} [19, 20].

2.2.4 Glow discharge

Returning to the breakdown mechanism of section 2.2.2 if the applied field is further increased once the discharge becomes self sustaining continuous ion bombardment of the cathode occurs, generating further electrons which are accelerated away from it. As they increase in number a special type of discharge structure may develop termed a *glow discharge.* The glow attribute occurs due to large levels of recombination of excited particles and hence initially they were used for lighting applications [2, 8].

The glow discharge current rises rapidly, after ion bombardment of the

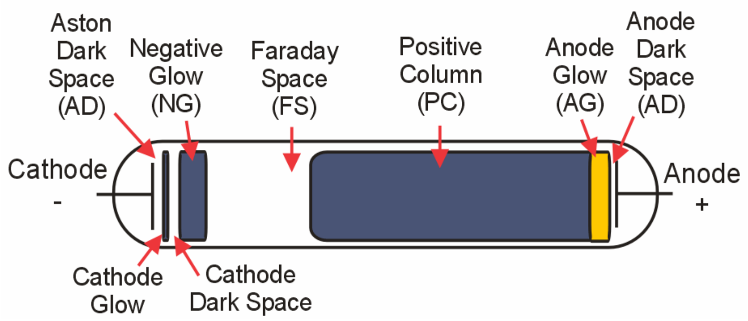

Figure 2.7: *Luminous structure of the glow discharge.*

cathode causes it to be self sustaining, independent of the gas voltage and the cathode remains cold throughout (this is not the case for arc discharges (see figure 2.9). Figure 2.7 presents a diagram of the luminous structure which develops when a glow discharge forms. The dimensions of the features within the image are proportional to the mean free path of the particles which cause their formation and hence this structure is more easily visualised at low pressures rather than at atmospheric pressure.

The luminous structure can be explained by considering the motion of the electrons. As they are accelerated away from the cathode, they have not acquired enough energy to cause atomic excitation leading to the Aston dark space being formed. They then gain further energy from the electric field and atomic and molecular excitations occur leading to the formation of a glow space - Cathode glow.

The electrons are then further accelerated from the cathode glow and acquire enough energy to cause ionisation of the gas particles. Very little atomic excitation occurs as a result and hence the cathode dark space is formed. The large increase in electron density leads to shielding of the electric field and so the electrons in the reduced field, just outside of the cathode dark space, participate in atomic and molecular excitations once again leading to the negative glow being formed [2, 7, 8].

The Faraday dark space is a region of low electron density leading to an increase in the electric field and the formation of the large quasi-neutral region of the positive column where the average electron energy grows to 1-2 eV and excitation processes occurring once again. Similar field and density changes are responsible for the anode dark space and anode glow also.

The structure and formation of the glow discharge is well known for several decades and most plasma applications are based around this knowledge [1]. Therefore many studies of homogeneous dielectric barrier discharges (see section 2.3.2) have sought to discover if the glow discharge mechanism is responsible for formation of such discharges [3, 21–23].

2.2.5 Physical and chemical processes due to gas breakdown

As stated in the introductory section, gas discharge breakdown results in the production of a large variety of atomic/molecular, ionic and excited species that may be used in physical and chemical reactions which may not be realisable by any other conventional means. The production of some of these species with reference to the geometry of figure 2.4 is shown in figure 2.8.

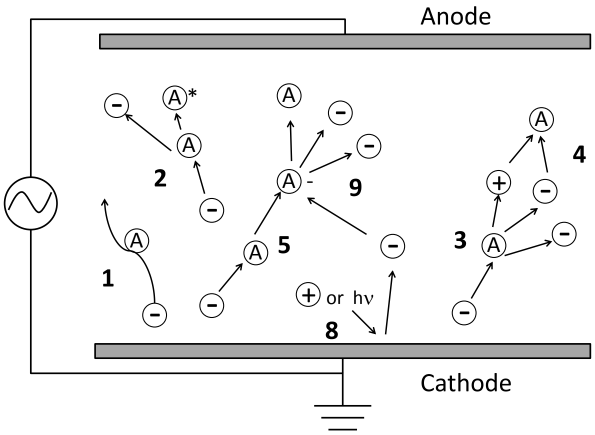

Figure 2.8: *Physical and chemical reactions in a gas discharge. In the figure ⊕ are positive ions, Ⓐ- negative ions, ⊖ electrons, Ⓐ neutral species and Ⓐ* excited neutral species. The numbers in the figure refer to those reactions in table 2.1.*

A synopsis of the most important gas discharge physical and chemical mechanisms is given in table 2.1 [7]. The number of plasma chemical processes can be enormous and so the reactions listed should not be considered exhaustive. The reactions of table 2.1 are not only important in the production of chemically reactive species in atmospheric pressure discharges (APDs) but also in the propagation and stability of the discharge itself. With reference to the previous three sections, reactions 3, 4, 7, 8, 13 and 14 are obviously important in the initial breakdown and in sustaining the discharge. It will also be shown that in discharges at atmospheric pressure, reactions 5, 10 and 11 have a significant role to play in the breakdown mechanism and sustaining

Table 2.1: Physical and chemical processes in plasma

Electronic and Atomic/Molecular reactions		
Reaction	Description	Number
$e^-_{fast} + A_{slow} \rightarrow e^-_{slower} + A_{faster}$	Elastic collision	(1)
$e^- + A \rightarrow e^- + A^*$	Excitation by electrons	(2)
$e^- + A \rightarrow e^- + A^+ + e^-$	Electron impact ionization	(3)
$e^- + A^+ \rightarrow A$	Electron - ion recombination	(4)
$e^- + A \rightarrow A^-$	Electron attachment	(5)
$e^- + A_2 \rightarrow A^- + A$	Dissociative attachment	(6)
$e^- + A_2 \rightarrow A^+ + A + e$	Dissociative ionization	(7)
$A^* or A^+ + B \rightarrow A + e^-$	Secondary electron emission	(8)
$e^- + A_2 \rightarrow A_2 + 2e^-$	Detachment	(9)
Atomic, Molecular and photonic reactions		
Reaction	Description	Number
$M^* + A_2 \rightarrow M + 2A$	Penning dissociation	(10)
$M^* + A_2 \rightarrow M + A_2^+ + e^-$	Penning ionization	(11)
$M^\pm + A \rightarrow M + A^\pm$	Charge transfer	(12)
$M^- + A^+ \rightarrow MA$	Ionic recombination	(13)
$h\nu + A \rightarrow e^- + A^+ or A^*$	Photoionization and excitation	(14)

the homogeneity of the discharge.

The photonic emissions in reaction 14 can provide comprehensive information associated with the plasma produced species, electron energies and discharge type, through the use of optical emission spectroscopy (OES) [24].

2.3 Classification of atmospheric pressure gas discharges

Atmospheric pressure discharges (APDs) are classified according to their volt-ampere generative characteristic and topology. The classification due to the volt-ampere characteristic is shown in figure 2.9. These plasmas include corona discharges [2], from D to E in figure 2.9, Dielectric Barrier Discharges (DBDs); including Filamentary Discharges (FDs) and ozonizers [25], from E to H in figure 2.9 and arc jets, from H to K. More recent developments include the Atmospheric Plasma Jet (APJ)[26], from F to K, the Atmospheric Pressure Glow (APG) [21, 27] discharge from D to G, and the One Atmosphere Uniform Glow Discharge Plasma (OAUGDP) [3], from F to H in figure 1. Each of the plasma classifications from C to H share common properties i.e. they are all non-thermal, non-equilibrium plasma and are produced in air or noble gas with halogen admixtures.

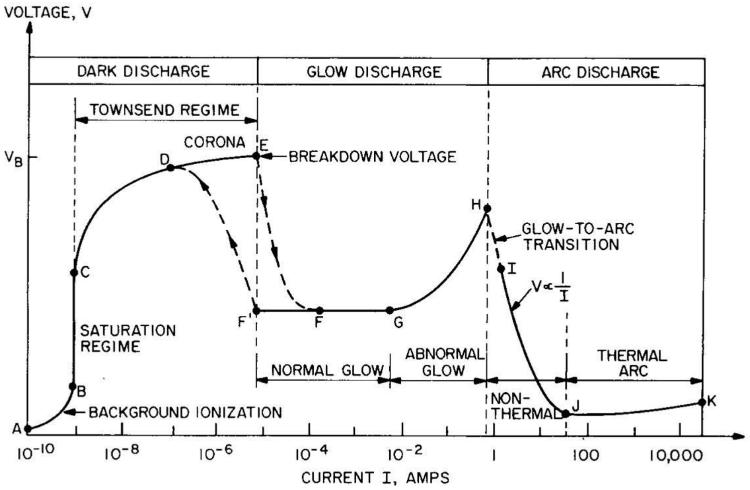

Figure 2.9: *Volt-ampere classification of APDs*

2.3.1 Corona discharges

Corona discharges are formed by large, non-uniform electric fields at pointed conducting surfaces or thin wires. The discharge can be created using several geometrical arrangements: parallel coaxial cylinder, concentric spheres, parallel wires or parabolic tip to plane (or by combining one half of each arrangement e.g. parallel wire anode to planar cathode). These discharges are always highly non-uniform. A region of weak luminosity develops at the anode or cathode depending on whether the discharge is a positive or negative corona. In the former case ionization is provided by the formation of a cathode directed streamer and in the latter by the Townsend breakdown mechanism, in which a multiplication of avalanches occurs and continuity of the plasma

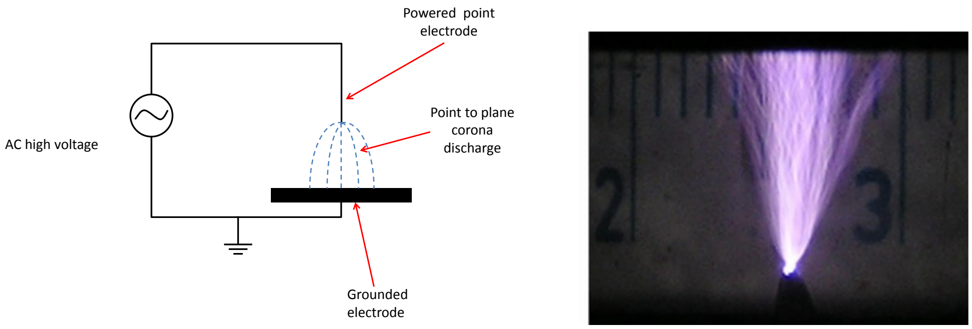

(a) AC driven corona schematic **(b)** Image of corona discharge

Figure 2.10: *Schematic and image of a point to plane corona discharge*

current is propagated by secondary electron emission due to ion impact at the cathode [2].

As an example we take the general equation which was formulated in [28] to describe the current-voltage characteristic of a corona in point to plane configuration (see figure 2.10)

$$I = K(V - V_0)^n \tag{2.14}$$

In equation 2.14 I is the discharge current, V the applied voltage, V_0, the corona inception voltage and K a constant, both of which are functions of the discharge geometry and ambient conditions. The constant, n, varies from 1.5 to 2 [28].

For a discharge using a 50μm point radius, steel pin electrode, on a planar copper ground plate in air, an empirical relation for the constants in 2.14 were determined as

$$K = C_1 S^{-0.41} \tag{2.15}$$

and

$$V_0 = C_2 S^{0.51} \tag{2.16}$$

where $C_1 = 0.525\ \mu\text{Amm}^{0.41}$ and $C_2 = 0.759\ \text{kV}^{-1.6}\text{mm}^{-0.51}$ and S is the pin to plate gap distance. The volt-ampere characteristic for this configuration is shown in figure 2.11 for gas gap distances of 10 - 100 mm (the current is prevented from rising too high by using a large resistance in series with the circuit).

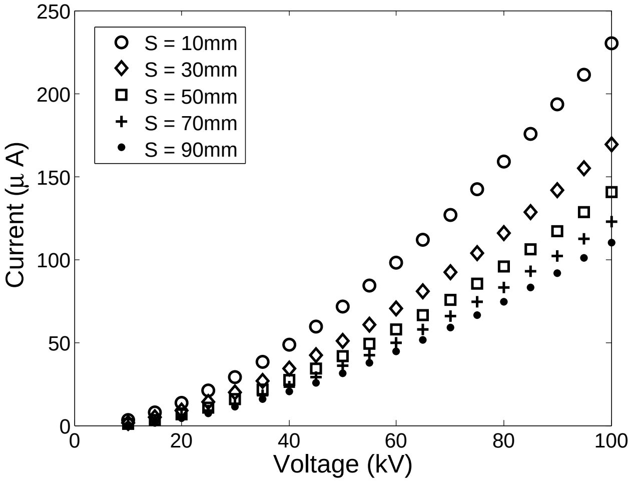

Figure 2.11: *Volt-ampere characteristics of the point to plane corona discharge in ref [28]*

It can be seen from this figure and figure 2.9 that even when very large voltages (~ 10-100 kV) are used, the current and hence the power coupling into the corona discharge remains quite small. It would seem reasonable from figure 2.11 that the efficiency of the discharge would be increased by decreasing the gap distance and increasing the applied voltage. However, if the distance between the anode and cathode is not sufficiently large (depending on the particular corona geometry) then the result is not a corona but the formation of a spark channel, resulting in highly non-uniform plasma and local overheating; both of which are unacceptable for most applications [2].

This undesirable effect of the corona may be eliminated by using a pulsed voltage, applied at sufficiently spaced intervals to enable streamer formation but prevent electron avalanches to breach the discharge gap; thus preventing spark channel formation. The pulsed discharge mode is usually preferred as it offers greater power transfer efficiency and a means to increase mean electron energies. Increased electron energies are necessary to the decrease the fraction of the input power going into vibrational excitation of the gas molecules (vibrational energies are generally much less than 1 eV) and to stimulate ionization and dissociation of molecules [7]. Because of the limitations of the corona discharge, it is generally invoked in gas cleaning applications and surface treatments where uniformity is not paramount [1, 2].

2.3.2 Dielectric barrier discharges

Introduction

As an alternative to the pulsed corona approach, streamer to spark formation may be prevented by covering one or both of the electrodes in an insulating dielectric barrier. The dielectric barrier capacitance and charge build up on its surface prevents the transition to arc formation through current limitation [2]. These types of APDs feature most prominently in the course of this thesis, consequently they require the most discussion.

DBDs have, historically, been termed 'silent discharges' [25, 29] as, whilst in operation, there is a notable absence of spark generation, which produces local overheating, generating local shock waves and noise. This feature makes DBDs extremely attractive to industrial applications where noise pollution levels must be kept to a minimum [2]. The dielectric barrier discharge was first conceived and implemented by Siemens for the production of ozone [25] (see figure 2.12). Since then concentrated research has resulted in applications such as: gas abatement and treatment of volatile organic compounds [30],

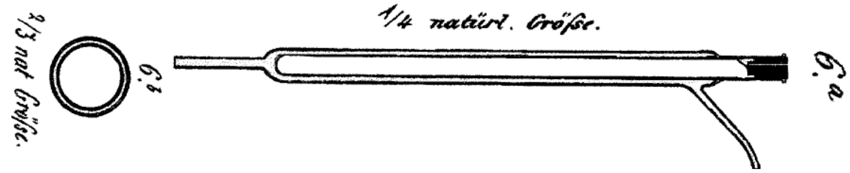

Figure 2.12: *Siemens 'ozonator'*

materials surface modification [31], etching of photoresist [32], gas discharge lasers [33], UV and VUV lamps [34] and plasma display panels, PDPs [35]. At large *Pd* values, DBDs usually take on a highly non-uniform appearance whereby the discharge is formed according to the streamer mechanism (see section 2.2.3) [36].

Formation of homogeneous DBDs

Dielectric barrier discharges can assume many configurations, of which the example shown in figure 2.13 is the most common. This discharge configuration consists of two planar electrodes, one driven by an AC or pulsed DC high voltage power supply and the other connected to ground. Each electrode is covered with a film or coating of dielectric material, the presence of which prevents the rapid formation of arc or spark discharges through current limitation [23, 37]. The transient discharge is usually formed under high voltage AC (~ kHz) excitation, by the Townsend mechanism (see section 2.2.2) where electron avalanches lead to a homogeneous breakdown followed by charge deposition on the electrodes and choking of the discharge. Each separate discharge occurs once or more per half cycle (depending on the drive parameters) and lasts of the order of μs. A typical current voltage trace for homogeneous DBD in helium is shown in figure 2.14.

The formation of a homogeneous DBD at atmospheric pressure is not obvious [22]. The gas gap breakdown usually results in a multitude of non-uniform ‘filaments’ or breakdown channels [36]. Each channel corresponds to

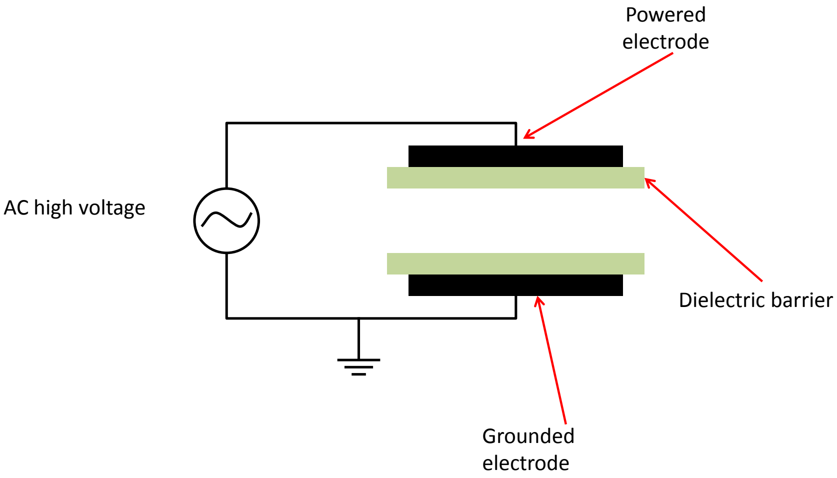

Figure 2.13: *AC driven dielectric barrier discharge schematic*

a single transit breakdown or coupling of streamers. The filaments or 'micro discharges' which result generally have diameters of the order of 100 μm. Micro discharges are extinguished when charge accumulates on the dielectric electrode, thus creating an opposing electric field which 'chokes' the discharge. Micro discharges are usually of very short duration, of the order of ns, and cause ionization and excitation both within and outside the channel through diffusion of highly energetic species. However homogeneous, stable glow-type discharges (like those discussed in the previous paragraph) may be formed under special conditions: through the use of noble gases or noble gas admixtures [3, 21, 22], 50 Hz [21], audio frequency [3, 22, 38, 39] or RF excitation [40] and current limitation techniques [37, 41].

The first homogeneous DBDs, i.e. those which possessed no obvious fila-

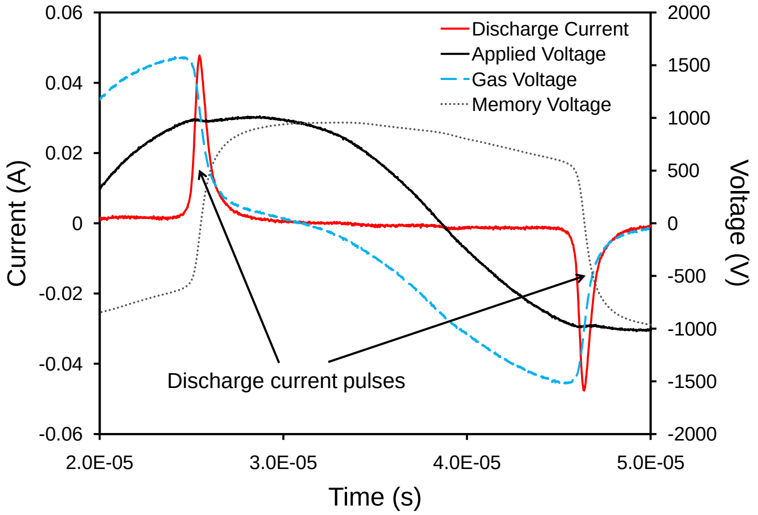

Figure 2.14: *Typical current voltage characteristic of a homogeneous DBD*

mentary or micro discharge structures, at atmospheric pressure were reported by Okazaki's group at Sophia University, Tokyo using brush [42] or mesh backed electrodes [21]. Using these configurations, stable discharges could be formed in helium, air, oxygen and nitrogen which were termed atmospheric pressure glow discharges (APGDs).

Following this work, Massines et al.[22, 43, 44] through experimentation and fluid modelling, proposed the theory that stable glow discharges formed in helium and nitrogen require a sufficient preionisation from electrons and ions remaining in a positive column between discharges (helium)[22, 43] and metastable species (nitrogen) [43, 44]. They showed that the Penning ionisation due to metastable species, which thermally diffuse at speeds much lower than the accelearted electrons, acts to inhibit the rapid formation of streamers and hence slows down the ionisation mechanism, preventing spark or arc formation [43]. In tandem with this work Roth et al. [3, 8] proposed that the drive frequency may be tailored to prevent ions from being lost between discharges thus allowing the formation of a homogeneous discharge in helium at gas gap distances of up to 2 cm.

Besides preionisation effects and those associated with the drive circuitry, further modelling [45–47] and experimental works [47, 48] analysed the effect of surface charge trapping on the homogeneity and physics of the DBD. In [46, 48] it was found that electrons in shallow traps on the dielectric surface can significantly influence the discharge structure during the voltrage reversal and breakdown whilst, in [47], long term instabilities could be modelled through varying the secondary electron emission coefficient of a simple zero dimensional model. Figure 2.15 shows a comparison between inhomogeneous and homogeneous DBDs within the same atmospheric pressure plasma system studied in this work. Throughout studies in further chapters of this thesis, the factors associated with the formation of homogeneous DBDs outlined above shall be taken into account.

2.3.3 Cold atmospheric pressure plasma jets

Whilst atmospheric pressure dielectric barrier discharges have found use in many modern applications, the relatively newer development of cold atmo-

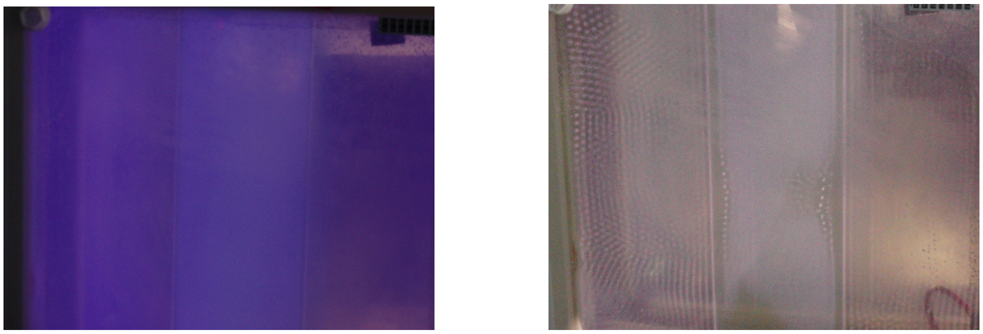

(a) Homogeneous DBD **(b)** Inhomogeneous DBD

Figure 2.15: *Comparison between homogeneous and inhomogeneous DBDs*

spheric pressure plasma jets (APPJs) [26] represent a far more versatile alternative when the materials to be treated cannot be confined between the electrodes of the DBD system [26, 49]. The jet is usually struck within a cylindrical dielectric tube through the application of RF or pulsed DC high voltage to an inner or outer cylindrical electrode whilst another electrode remains grounded and through the use of noble gases and gas admixtures [26, 49].

The most useful feature of APPJs is their ability to introduce plasma excited atomic and molecular species to substrates far away from the source of excitation, thus minimising the potential for arcing or high voltage drops across the substrate. Thus they are particularly suitable for use in the relatively new discipline of plasma medicine, where they are already being developed for numerous applications from bacterial sterilization to animal tissue treatment[50–54].

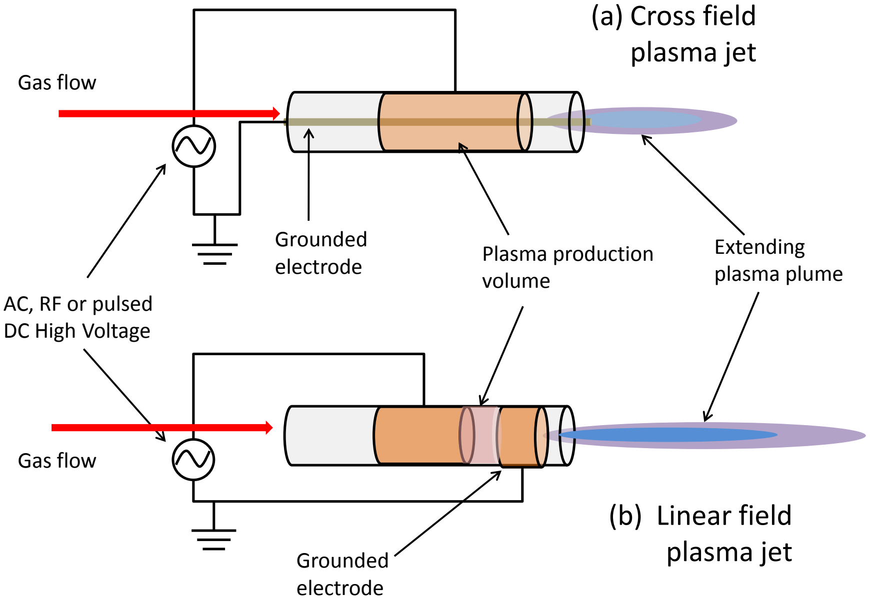

Figure 2.16: *Schematics of the topologies of (a) cross field and (b) linear field atmospheric pressure plasma jets*

There are two main configurations of such plasma jet devices (see figure 2.16): those where the applied field is perpendicular to the gas flow (cross field) and where the applied field is parallel to the gas flow (linear field) [55].

In [55] it has been shown that when the jet is in the linear field configuration a more reactive chemistry and higher electron temperatures result further downstream of the plume excitation, therefore, in recent years, research and applications of APPJs has focused on the linear field form of the jet [50, 56–60].

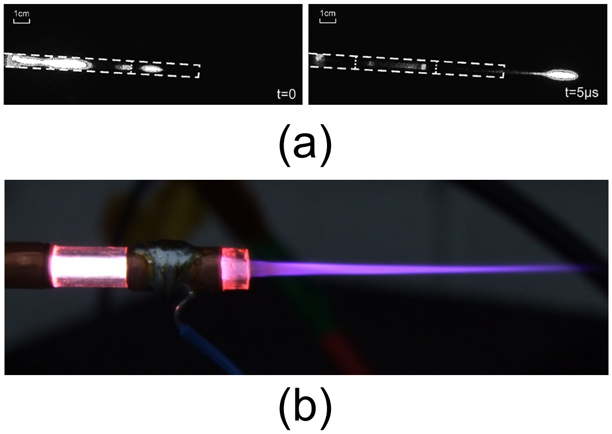

Figure 2.17: *Digital images of two APPJ sources in operation: (a) ICCD image with 100 ns second exposure time (b) Still camera image with 1 ms exposure time*

Whilst, ostensibly, the plume produced by the linear field jet appears continuous (c.f. figure 2.17 (b)) it is actually formed by either one or a number of discrete breakdown events which propagate at hypersonic velocities [56] (c.f. figure 2.17 (a)) when viewed through high speed imaging. This structure of the jet has been attributed to a streamer like mechanism of generation [61] as described in section 2.2.3.

As with DBDs, APPJ discharge breakdown, structure and chemical reactivity are sensitive to the type of high voltage excitation [55, 61–63] and both gas flow and gas composition [59, 62–64].

2.4 Conclusions

In this chapter a review of the major features associated with the formation, stability and chemical reactivity of the most common and current atmospheric gaseous discharges has been presented. From the foregoing review it is clear that each type of atmospheric discharge can be analysed through myriad diagnostic methodologies. Each discharge type is subject to and produces multiple physical phenomena (electrical, optical and fluid dynamical) which may be monitored using various sensors to diagnose its performance. Therefore this thesis seeks to apply this knowledge in the analysis of the performance of different atmospheric discharges through novel diagnostic methodologies with a view to achieving a better understanding of their operation and enhancement of discharge processing outcomes.

CHAPTER 3

Atmospheric pressure plasma tool design

3.1 Introduction

In order to evaluate the diagnostic methodologies and carry out surface modifications within the course of work for this thesis, the design and construction of two atmospheric pressure plasma sources was necessary. The following presents a full description of the design of these sources and method of operation.

3.2 Experimental dielectric barrier discharge chamber

3.2.1 DBD chamber design

The design of a dielectric barrier discharge chamber was implemented to carry out controlled diagnostic experiments on a DBD source over varying discharge parameters. This chamber construction was similar to those in references [22, 37, 65, 66]. A schematic of the inner chamber construction is shown in figure 3.1 whilst the outer chamber is detailed in 3.2.

The cylindrical chamber was constructed of stainless steel of 110 mm inner diameter and 120 mm outer diameter and measured 200 mm in height. The cylindrical electrodes were made of stainless steel and measured 44 mm in diameter and 15 mm in height. The electrodes were chamfered at the edges to prevent field localisation whilst high voltages were applied. Stainless steel screws were embedded in the electrodes to allow vertical adjustment of the inter-electrode spacing. Both of the entire electrode assemblies were housed in Teflon to prevent arcing to the surrounding chamber walls. Dielectric materials were fixed to the electrodes using high-vacuum silicon based grease, as in [37].

Three line of sight ports were positioned radially to the electrode axis to allow multiple optical diagnostic access whilst the entire discharge could be

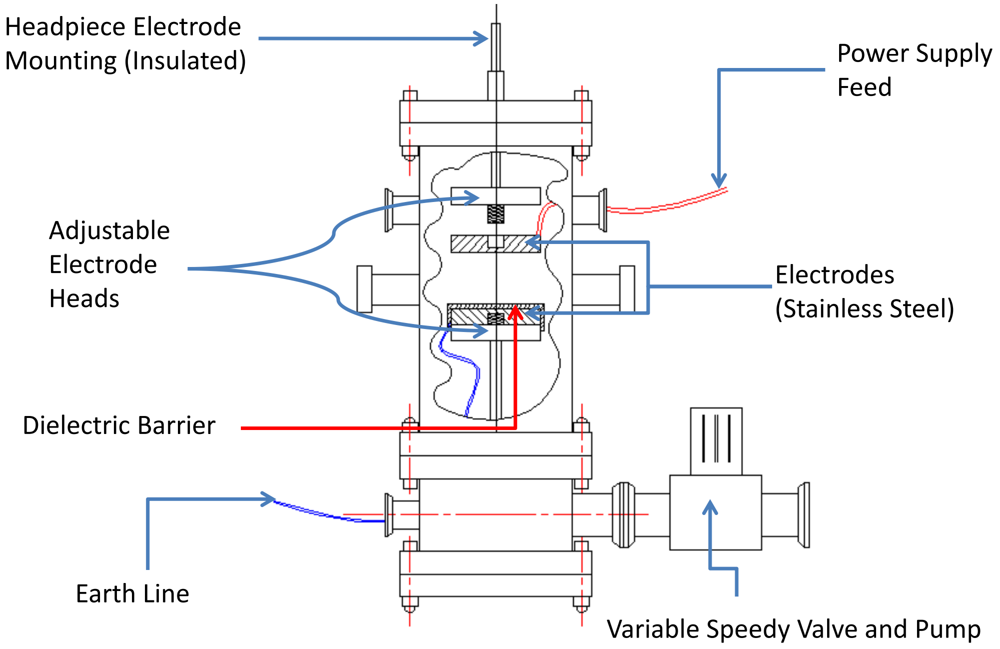

Figure 3.1: *Inner experimental DBD chamber construction*

viewed through a quartz window, at the front, to allow observation of the discharge in operation and taking of digital images. Two mass flow controllers, 0-10,000 sccm (standard cubic centimeters) and 0-500 sccm respectively, were constructed to flow helium gas and helium gas admixtures through the entire chamber whilst a roughing pump was used to evacuate the chamber and maintain the atmospheric pressure under gas flow.

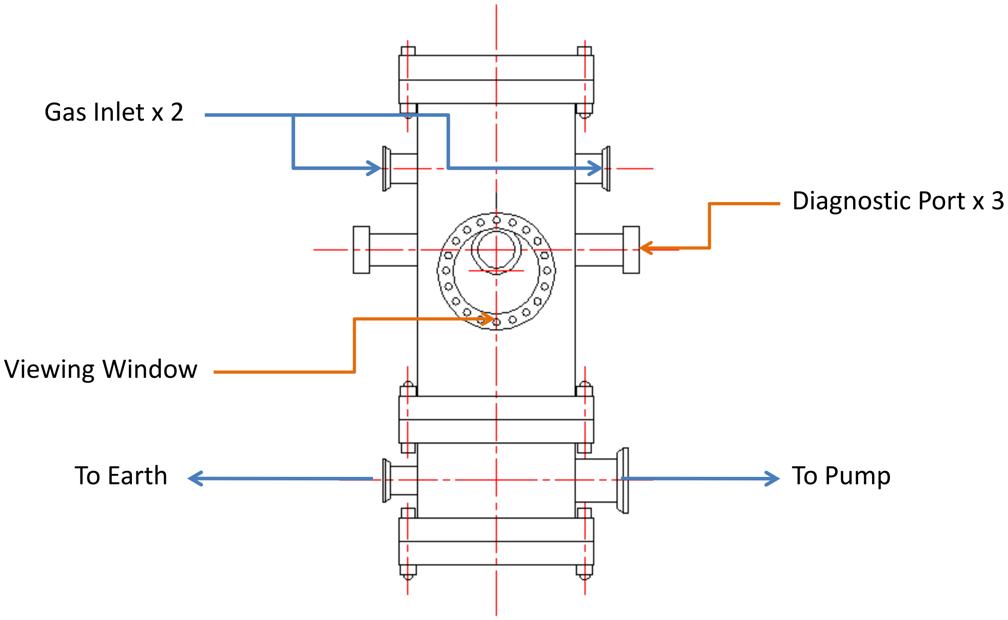

Figure 3.2: *APGD chamber construction*

3.2.2 DBD high voltage power supply

The power supply to generate the discharge consisted of a signal generator, power amplifier, ferrite transformer and tuned resonant circuit array, the details of which are shown in figure 3.3.

A spectrally pure high voltage sinusoidal output was produced using the following methodology. An external square wave signal is fed into the power amplifier (Thurlby Thandar Instruments), the output of which drives the primary of an in house designed ferrite e-type cored transformer (1:100 turns

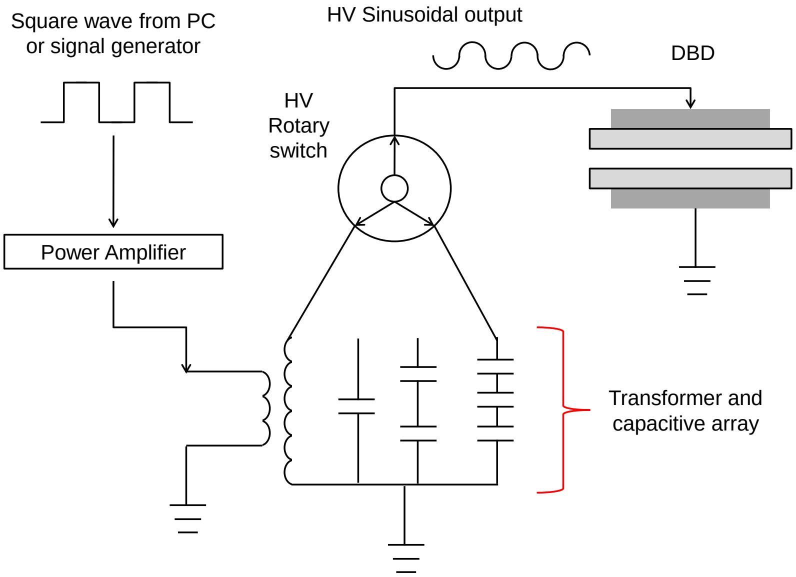

Figure 3.3: *DBD high voltage circuit schematic*

ratio). The output from the secondary of the transformer is fed into the resonant circuit array which consists of a set of high voltage capacitors whose values have been empirically selected to isolate the first harmonic of the output signal at a set of pre-determined frequencies, *f*, from 5-75 kHz according to equation 3.1. The resonant circuit is configured in parallel to the DBD system.

$$f = \frac{1}{2\pi\sqrt{L(C_1 + C_2)}} \tag{3.1}$$

In equation 3.1, L, is the secondary inductance, C_1, the capacitance of the resonant circuit and C_2 the capacitance of the DBD system. It is clear from equation 3.1 that the maximum frequency which can be applied to the DBD system is when C_1 is equal to zero. The values of the capacitive array can be selected using a high voltage rotary switch in order to frequency match the resonant frequency of the output filter to that of the drive. An example of the power spectral density of a 32 kHz signal is shown in figure 3.4. In this figure it can be seen that the second and subsequent harmonics of the output are more than some 30 dB below the first.

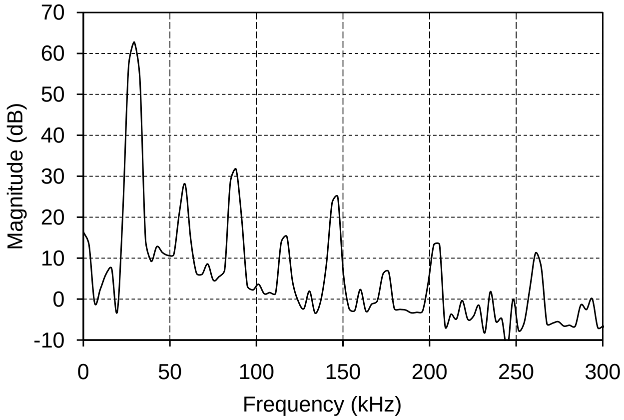

Figure 3.4: *Power spectral density of 32 kHz output from the in house designed power supply*

3.3 Linear field jet design

The linear field jet design was similar to that of [50, 55, 59]. However, in other experimental linear field jet systems, the ability to inject precursors in the form of micron sized aerosols is not generally incorporated. Therefore this linear field jet design investigated two methods of precursor injection *viz.* mechanical injection through the use of forced gas nebuliser and using an ultrasonic nebulisation chamber.

3.3.1 Linear field jet power supply unit

The drive circuitry is a modification of our previous design [67] to include pulse position modulation of the transformer primary input. The high voltage power supply consists of a dual LM555 [68] timer driven IRF540 n-channel MOSFET [69] circuit. The power output (0 - 60 W) can be twofold controlled using both pulse position modulation, through the coupled 555 timers, and by varying the D.C. input voltage. The details of the power supply unit are featured in the circuit schematic of figure 3.5.

The 555 timer to the left of the schematic is configured to operate as an astable multivibrator at a set frequency of approximately 50 Hz through the use of resistors R1, R2 and R4, diodes D1 and D2 and capacitor C4 [68]. Initially, when the power is switched on using the switching pot R4, capacitor C4 is uncharged. The capacitor is then charged through R1, D1 and the left side of R4 (R_L). The on time of the output is then given by [67, 68]

$$t_{on} = ln2(R1 + R_L)C4 \tag{3.2}$$

Where ,*ln*, indicates the natural logarithm. When the capacitor charges to 2/3 of the input voltage, it is discharged through the right side of R4 (R_L)

D2 and R2, pulling the output low for a time

$$t_{off} = ln2(R2 + R_R)C4 \tag{3.3}$$

The frequency of operation is then fixed at

$$f = \frac{1}{t_{on} + t_{off}} = \frac{1}{ln2(R1 + R2 + R4)C4} \tag{3.4}$$

Therefore the left hand 555 timer circuit acts as a constant frequency square wave source with variable duty cycle (0 - 95%). The values used here are R1 = R2 = R4 = 1kΩ, and C4 = 1μF giving a frequency of 48 Hz.

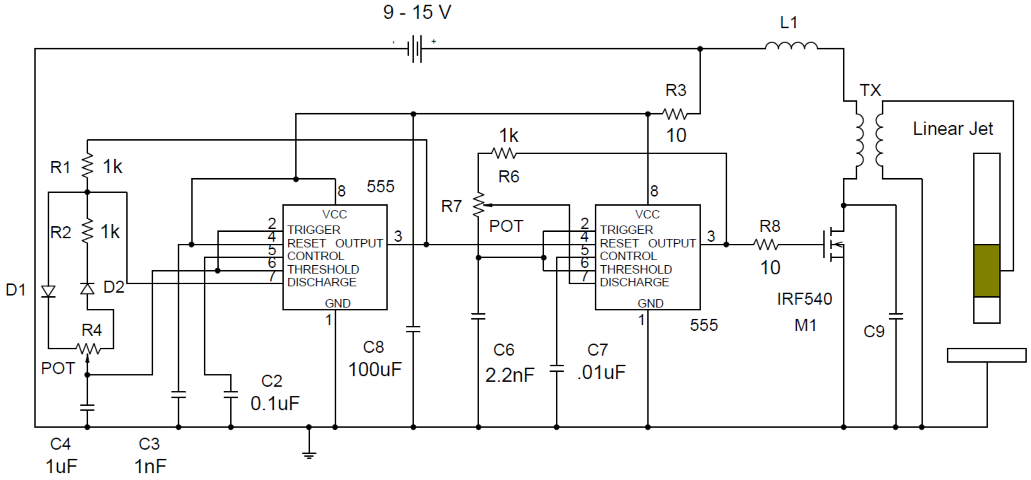

Figure 3.5: *APLFJ power supply unit design*

The second timer is configured as an astable vibrator to operate at a fixed frequency through the use of R6, R7 and C6. The operating frequency of this timer is fixed to the empirically determined resonant frequency of the combination of L1, C9 and the transformer primary inductance (approx. 31 kHz). Through suitable choice of L1 (in this case 6 μH) this value may be adjusted according to equation 3.1. The overall inductance was estimated to be approximately 12 μH therefore using a 2.2 μF capacitor the resonant frequency was tuned to be approximately 31 kHz according to equation 3.1. The output of this timer drives the gate of the MOSFET and is modulated by the output of the first timer.

The MOSFET is switched by the modulated output of the second timer, allowing current to flow through the primary of TX, which in turn induces a high voltage, of up to 15 kV peak to peak, in the secondary coil. The transformer (TX) is a home made 1:120 turn ferrite E-type core flyback with a 0.1 mm air gap.

Using the power supply, the average power coupled into the discharge can be dually controlled both by varying the amplitude of the high voltage pulses on the secondary of the drive circuit and through modulation of the pulses using the potentiometer at R4. Typical current and voltage waveforms of the discharge in operation with 6.5 kV peak to peak voltage are shown for a modulation duty cycle of approximately 60% in figure 3.6.

3.3.2 Atmospheric Pressure Linear Field Jet Source

The linear field jet is constructed of a 100 mm glass tube, inner diameter 2mm and outer diameter 4 mm. The concentric outer electrodes are made of copper

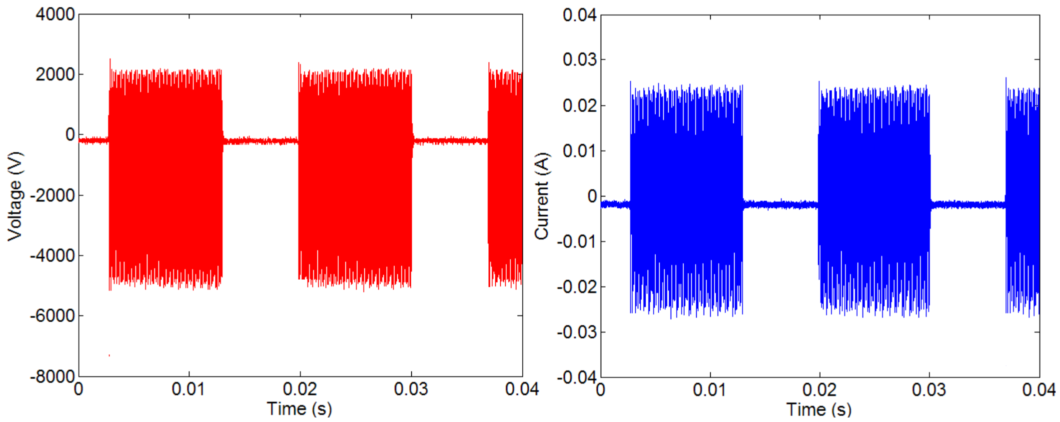

Figure 3.6: *Typical current and voltage waveforms for a duty cycle of c. 60%*

tape. The driven electrode is 20 mm in length. The grounded electrode is 10 mm in length and is terminated at 2 mm from the output end of the tube. The two electrodes are spaced 10 mm apart. The high voltage power supply causes the gas to break down within the central core of the glass capillary, generating an external plume of plasma radicals and excited species which interact with the substrate.

The device incorporated two modes of precursor nebulisation injection systems. Mechanical nebulisation was performed using a modified airbrush. In this mode aerosols were formed by forcing a secondary gas flow through the airbrush barrel, creating a venturi draw which pulled the precursor from an attached flask and forced it through a small orifice. However, no estimation of aerosol particle sizes could be drawn using this method.

The second method used ultrasonic nebulisation. Deposition precursors

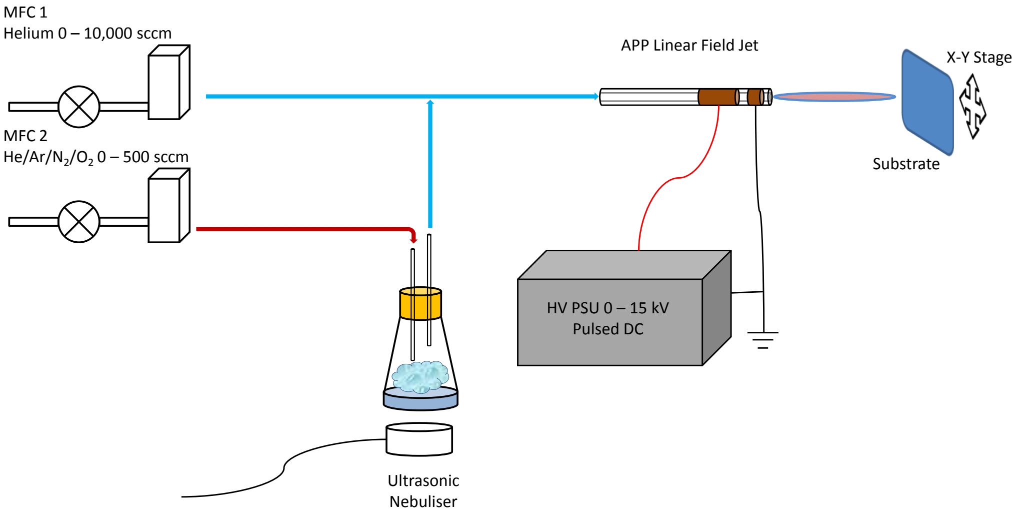

Figure 3.7: *APLFJ and precursor delivery system*

are introduced into a conical flask. An external ultrasonic nebuliser (Asia mist, frequency 1.7 MHz) is used to generate cold precursor aerosols within the flask. The aerosol particle diameter, D, may be determined by evaluating the longitudinal wavelength, λ , produced at the surface of the liquid using equation 3.5 [70]

$$\lambda = \left(\frac{8\pi\sigma}{\rho\nu^2}\right)^{\frac{1}{3}} \tag{3.5}$$

where ρ is the liquid density, σ the liquids surface tension and ν the ultrasonic wave frequency. The particle diameter, D, is then given by

$$D = 0.34\lambda \tag{3.6}$$

The primary feed gas flow into the linear field jet is maintained through

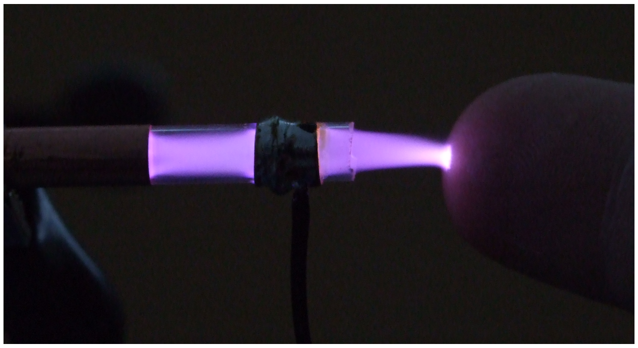

Figure 3.8: *Image of plume in contact with human skin*

mass flow controller MFC 1. The flow can be continuously varied from 0 - 10,000 sccm. A secondary flow is introduced into the conical flask or modified airbrush through MFC 2 (0 - 500 sccm). The secondary gas is normally helium but other gases may be used depending upon the surface treatment type. The total volumetric flow of added precursors, in the case of ultrasonic nebulisation, is determined by the volume of liquid introduced into the flask, the container size and the secondary flow rate from MFC2.

An electronically controlled x-y stage is used to adjust the position of substrates downstream of the plasma plume to ensure homogeneous treatment times over the substrate surface. An example of the non-thermal nature of the plume is shown in figure 3.8 where the plume was generated under maximum power coupling and is in contact with human skin.

CHAPTER 4

Electrical and optical diagnostics of an industrial scale atmospheric pressure plasma surface treatment tool

4.1 Introduction

Recently [1, 3, 13], large volume atmospheric pressure plasmas (APPs) have been shown to be an economically viable alternative to low pressure plasma surface treatment methods. The nonequilibrium, nonthermal nature of APP treatments makes them ideal for polymer surface modifications. Contemporary materials processing applications include: polymer adhesion enhancement [71], biocompatible coatings of implants [72] and photoresist etching [10, 73]. Characterisation of homogeneous atmospheric pressure dielectric barrier discharges (DBDs) has been carried out since 1990 [27] and has since incorporated extensive optical and electrical analysis techniques. These include fast intensified charge coupled detector (ICCD) imaging [22, 38, 74] and the use of a photomultiplier tube [38, 74] to resolve time varying discharge events, optical emission spectroscopy [75, 76] and current and voltage waveform analysis [22, 38, 44, 74].

However, limited diagnostics have been performed on industrial scale atmospheric pressure plasma processing tools. With the commercial exploitation of this technology it is increasingly important to apply and develop techniques which will correlate the atmospheric pressure plasma electrical and optical parameters with the properties of the deposited coatings. Thus, the objective of this study is to determine the effect of varying process parameters *viz.* applied power, discharge gas composition on discharge characteristics and chemistries.

4.2 Atmospheric pressure plasma system and diagnostics

4.2.1 Industrial scale atmospheric pressure plasma chamber

The diagnostics were carried out on the Dow Corning® SE-1100 AP4 atmospheric pressure plasma system [77] at the Mechanical Engineering Department of University College Dublin. An image of the system is shown in figure

4.1. It comprises two separate, vertically oriented parallel-plate plasma chambers together with an automatic, reel-to-reel polymer film handling system. The electrode gap width is 5 mm. The electrodes are made of toughened glass with dielectric housing. Each set of electrodes contains a conductive saline solution in order to couple the applied power to the dielectric barriers.

The input power to the plasma system may be varied continuously from 0-2000 W using a Vetaphone ac power supply, which operates in the frequency range 15-25 kHz. The power supply has a frequency agile impedance matching circuit, rather than altering inductor and capacitor elements. Circuit resonance is maintained using a pick-up coil on the transformer secondary winding, which sends the load voltage and current magnitude and phase to the frequency matching circuitry. Here the supply frequency is adjusted to ensure that the real component of the two complex impedances are of the same value and the imaginary component of the impedances is of the same but of opposite sign ($|\pm jx|$). At this point maximum real and minimum reactive power transfer is achieved between the two impedances. Manual valved rotameters are used to control gas flows. Helium and O_2 (when used) gas flow rates were maintained at of 10 l/min and 0.1 l/min respectively. A syringe pump may be used to supply the liquid precursor to 2 atomisers positioned at the top of the plasma deposition chamber. Poly (ethylene teraphthalate) (PET) film of width 10 cm and 50 m in thickness, available from AB Supplies Ltd. (UK), was passed through the electrodes using the integrated polymer film handling system at a speed of 1.5 m/min. At a film speed of 1.5 m/min,

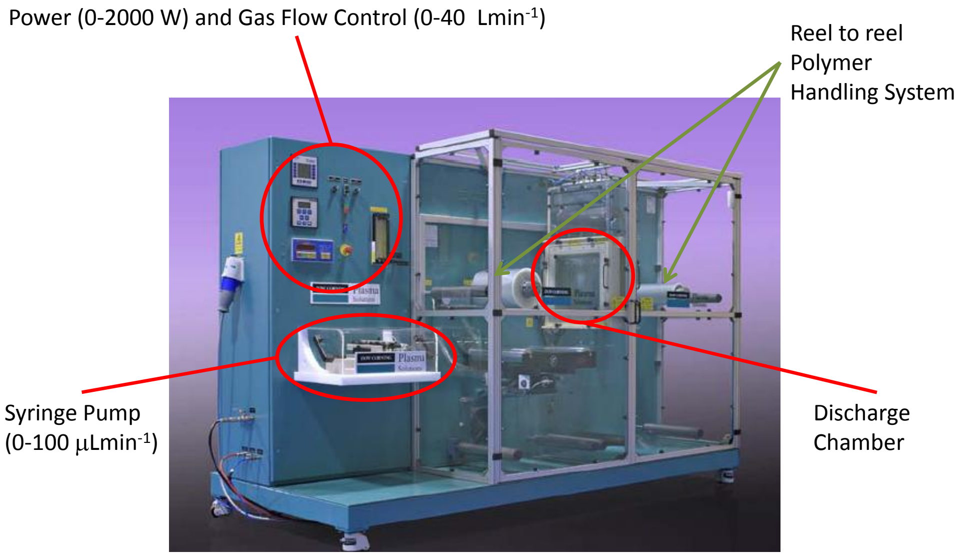

Figure 4.1: *Dow Corning ® SE-1100 AP4 atmospheric pressure plasma system*

the residence/deposition time of a polymer section is approx. 25 s per pass.

4.2.2 Diagnostics

The diagnostic set-up is detailed in figure 4.2. Current and voltage values were measured using a Pearson 6585 (1A: 1V) fast current monitor and a North Star PVM-5 (1kV: 1V, Bandwidth 80 MHz) high voltage probe respectively. Current and voltage measurements were obtained between the output of the RF power supply and the dielectric electrodes. A photomultiplier tube (PMT) (RCA 931A) with a rise time of 1 ns and a spectral range from 300 to 800 nm was used to measure the temporally resolved total emission from the discharge through a 1 mm^2 circular aperture. The PMT was mounted perpendicular to the transparent face of one of the electrodes. As the PMT is imaging through a non-UV transparent surface the effective spectral range is 400 to 800 nm. The electrical and PMT signals were collected on a Tektronix TDS3034C oscilloscope and transferred to a PC where they were processed using a LabVIEW™ program. Optical emission spectroscopy (OES) was carried out using two Ocean Optics USB4000 UV/VIS spectrometers. A high resolution (0.05nm), low bandwidth (320-420 nm) spectrometer was used to obtain spectra in the UV range whilst a low resolution (1 nm), large bandwidth (300-900 nm) spectrometer was used to collect spectra across the whole UV-VIS range. The spectra were collected via a fibre optic and collimating lenses mounted vertically above the discharge. A digital camera was used to obtain images of the discharge through the electrodes.

4.3 Experimental results

The experiments consisted of using the multi-diagnostic methodology, set out in section 4.2.2, to examine variations in the plasma optical and electrical parameters in two operating regimes. Initially, the effect of systematically altering the applied power (400 to 2000 W - as measured by the internal power supply circuitry) in a pure helium (He) plasma with a flow rate of 10 lmin^{-1} was examined. Then the discharge optical and electrical parameters were examined in a helium/oxygen (He/O_2) plasma (helium flow rate - 10 lmin^{-1}, oxygen flow rate 0.1 lmin^{-1}) for the same applied powers. These

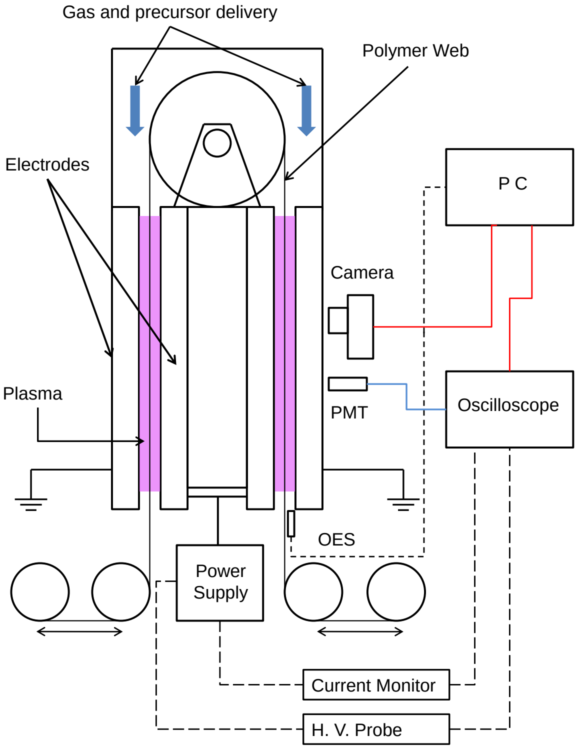

Figure 4.2: *Diagnostics of the Labline™ atmospheric pressure plasma deposition tool*

plasma chemistries are important in various polymer surface modifications e.g. enhanced adhesion properties and decreasing gas permeability of polymer films [7]. For all experiments the discharge chamber was subject to a prolonged period (30 minutes) of flushing with helium gas at a flow rate of 20 lmin^{-1}. As stated in section 4.2.2, the entire data sets for each of the optical and electrical parameters were taken synchronously. Throughout the experiments, the polymer film was passed through the system at a speed of 1.5 mmin⁻1, corresponding to usual operating conditions [78].

4.3.1 Electrical characterisation

Power and frequency dependence

The power dissipated in the plasma was determined by means of the charge-voltage Lissajous method originally proposed by Manley [79] and re-derived by Falkenstein and Coogan [80] to include stray capacitive effects. The charge, $Q(t)$, coupled through the discharge over a single period, T, was found through integration of the discharge current *I(t)*, in the LabVIEW™ program as a measurement capacitor could not be configured into the plasma tool. It is given by

$$Q(t) = \int_{t}^{t+T} I(t)dt \tag{4.1}$$

The total charge, breakdown voltage and chamber capacitances may be determined from the slopes and intersections of the Lissajous trace. The determination of these values from the slopes of the trace is shown in figure 4.3. In the figure, C_{die} is the capacitance of the dielectric barriers, C_{stray} the stray capacitance and C_{tot} the capacitance of the barriers in series with the gas gap. $V_b r$ is the gas gap breakdown voltage. The energy, E, coupled into the discharge is determined through evaluating the area of the figure. The discharge power is then found through multiplication by the frequency, *f*, of the applied voltage. A typical Lissajous figure for a He/O_2 plasma at an applied power

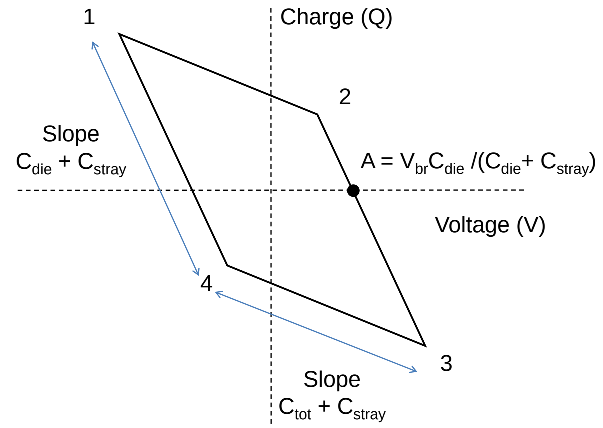

Figure 4.3: *A typical charge-voltage Lissajous figure*

of 1.5 kW is shown in figure 4.4.

The discharge efficiency, i.e. the percentage of the applied power coupled into the discharge, E_D may then be evaluated using equation 4.2

$$E_D = \frac{P_D}{P_A} \times 100(\%) \tag{4.2}$$

where P_D is the discharge power and P_A is the applied power. This is shown for the two chemistries in figure 4.5. As can be seen from this figure, at low applied powers i.e. less than 900W for He and less than 1200W for He/O_2, the efficiency of power coupling into the discharge is around 15% and 20 % respectively. There is a clear transition between powers of 900 - 1200W (He) and 1200 - 1600W (He/O_2) whereby the discharge efficiency rises to approximately steady values of 42% (He) and 50% (He/O_2). The power loss

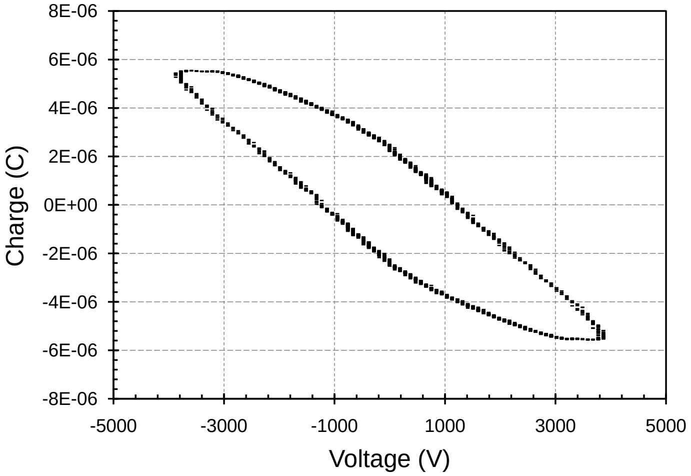

Figure 4.4: *Measured Lissajous trace in He/O_2 discharge at 1.5kW applied power*

is most likely due to ohmic heating in the supply leads and the electrodes themselves.

The abrupt change in the discharge efficiency for the two plasma chemistries results in some interesting features associated with the plasma tool drive circuitry. Figure 4.6a depicts the change in the plasma drive frequency, due to the agile match system, with increasing applied power whilst figure 4.6b shows the variation in the peak voltage across the discharge electrodes for the same applied powers.

It was observed that varying the plasma applied power resulted in a negative shift in the drive frequency of the power supply i.e. as applied power increases, the frequency decreases. This shift coincides with the shift associated with the discharge efficiency variation. The drive frequency scales linearly

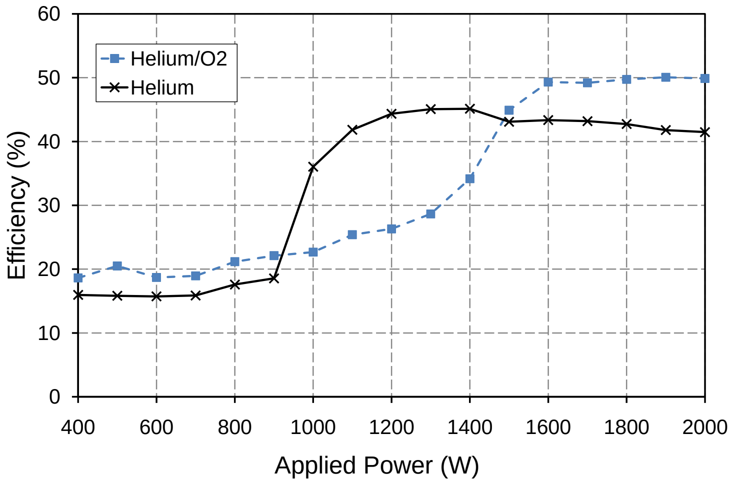

Figure 4.5: *Discharge efficiency of He and and He/O_2 plasmas with increasing applied power*

with discharge efficiency from 24 kHz to 16 kHz in both plasma chemistries. In the He plasma an abrupt frequency change occurs between 900 and 1000 W while in the He/O_2 plasma the greatest variation occurs gradually between 1300 and 1600 W. The maximum voltage dropped across the electrodes (figure 4.6b) shows similar trends with increased applied power. However, above the transition points (c. 900W in He and c. 1500W in He/O_2) the maximum voltage across the electrodes increases with increasing applied power, whilst the drive frequency remains approximately constant.

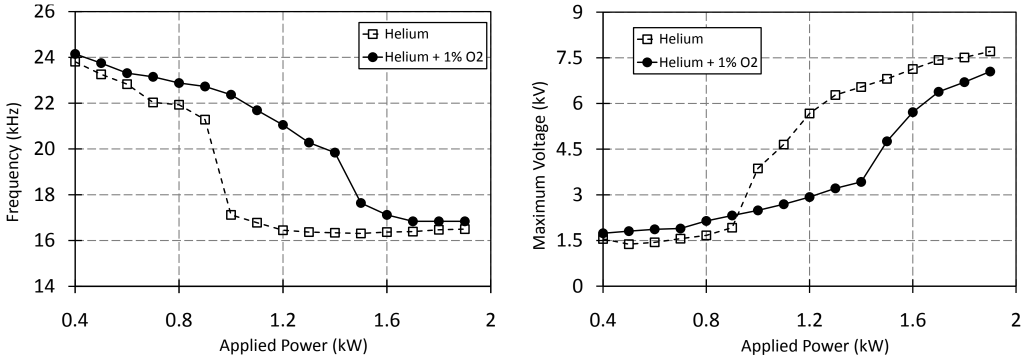

(a) Frequency Variation **(b)** Maximum Voltage Variation

Figure 4.6: *Variation in (a) operation frequency and (b) maximum applied voltage with increasing applied power*

Discharge structure and electrical waveforms

The distinct frequency, power efficiency and maximum voltage drop transitions are associated with distinct variations in the visual structure of the discharge and the electrical and optical signals. In figure 4.7 the discharge electrical and PMT signals are shown together with images of the discharge through the transparent electrodes for both plasma chemistries at 500W applied power.

Whilst the electrical and PMT signals in figures 4.7a and 4.7b reveal that the discharge is temporally periodic, the images in figures 4.7c and 4.7d show that the discharge is not spatially homogeneous. The discharge appears to be diffuse outside of the polymer web in the He discharge and there are patches of localised filamentary structures and dark regions over the polymer web.

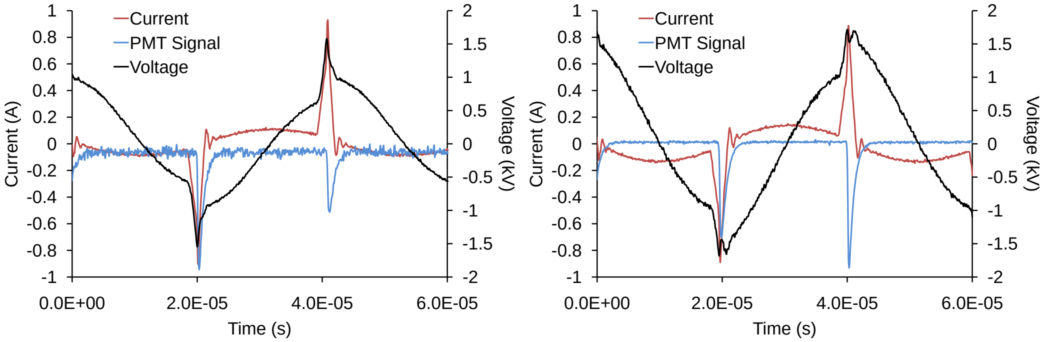

(a) Helium 500W **(b)** Helium/O_2 500W

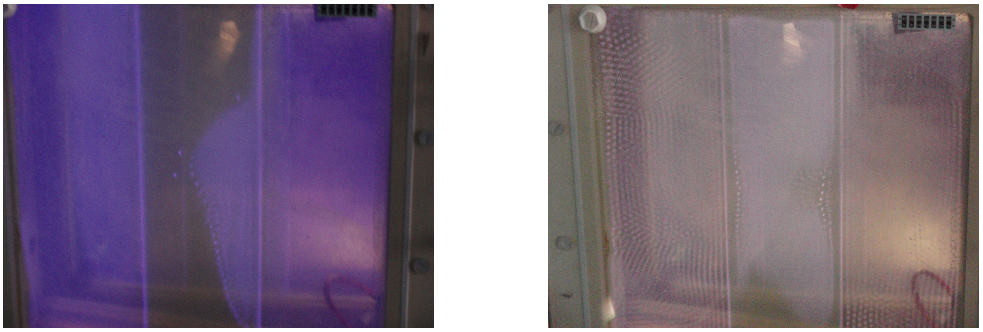

(c) Helium 500W **(d)** Helium/O_2 500W

Figure 4.7: *In the figure (a) and (b) correspond to electrical (voltage (black), current (red) and PMT (blue)) signals of Helium and Helium/O_2 discharges at 500W applied power. The images in (c) and (d) were taken of the discharge corresponding to (a) and (b) respectively*

In the He/O_2 discharge, however, the region outside of the web is occupied by filamentary structures and the web is occupied mostly by diffuse plasma regions with localised filaments and dark patches. In both cases the discharge is characterised by a single current pulse (F.W.H.M. ~ 2μs) per half cycle of the applied voltage, resulting in a sharp drop of some 100's of volts in the voltage signal. This current pulse is synchronous with a similar peak in the PMT signal. It is noteworthy that this type of current pulse and PMT signal, with a rise time of some ns and a much longer falling time in the μs range, together with a voltage drop due to charge deposition on the dielectric electrodes, is usually associated with a glow mode of the atmospheric pressure discharge [22].

A further increase in the applied power, to the point just before the abrupt transitions of figure 4.6, results in the discharge electrical waveforms and structures shown in figure 4.8. Here it is seen as the applied power increases, another distinct breakdown occurs per half cycle of the applied voltage in both discharge chemistries. In the helium discharge (figures 4.8a and 4.8c), almost the entire gap is filled with a homogeneous discharge with localised filaments over the polymer web. In the helium/O_2 discharge (figures 4.8b and 4.8d) the filaments become more numerous and densely packed. There are also regions where the filaments begin to organise into striped domains. These self-organised structures have been noted in dielectric barrier discharges previously [81, 82].

At applied powers above the point at which an abrupt shift occurs in the drive frequency and discharge efficiency (1100W in He and 1600W in He/O_2), the localised discharges appear to coalesce and the plasma becomes homogeneous over the entire electrode area (see figure 4.9). At this point the number of discharge events per half cycle increases linearly with applied

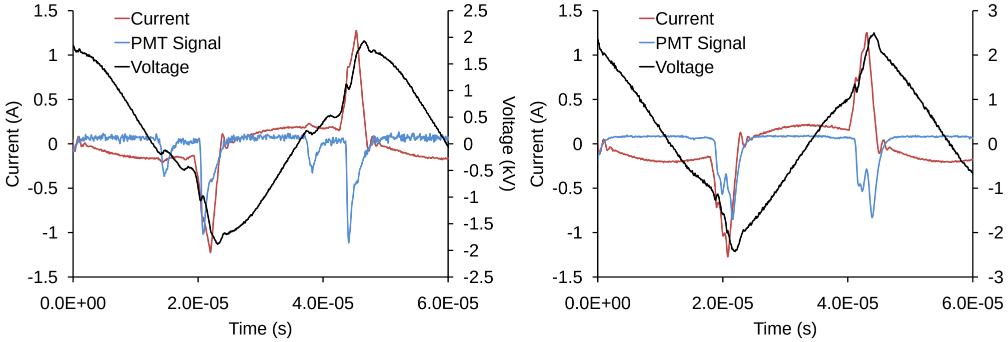

(a) Helium 800W

(b) Helium/O_2 1100W

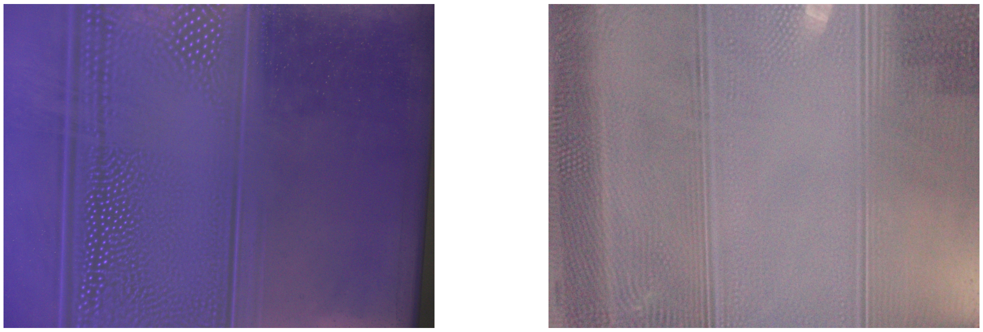

(c) Helium 800W

(d) Helium/O_2 1100W

Figure 4.8: *In the figure (a) and (b) correspond to electrical (voltage (black), current (red) and PMT (blue)) signals of Helium and Helium/O_2 discharges at 800W (He) and 1100W (He/O_2) applied power. The images in (c) and (d) were taken of the discharge corresponding to (a) and (b) respectively*

power. The number of discharge events at maximum applied power (2000W) in both chemistries is around thirteen per half cycle. The number of distinct discharge events occurring per half cycle of the applied voltage is detailed in figure 4.10. Here it can be seen that the number of breakdown pulses (current peaks) per half cycle is intimately linked to the decrease in the drive frequency and increase in the maximum amplitude of the applied voltage of figure 4.6.

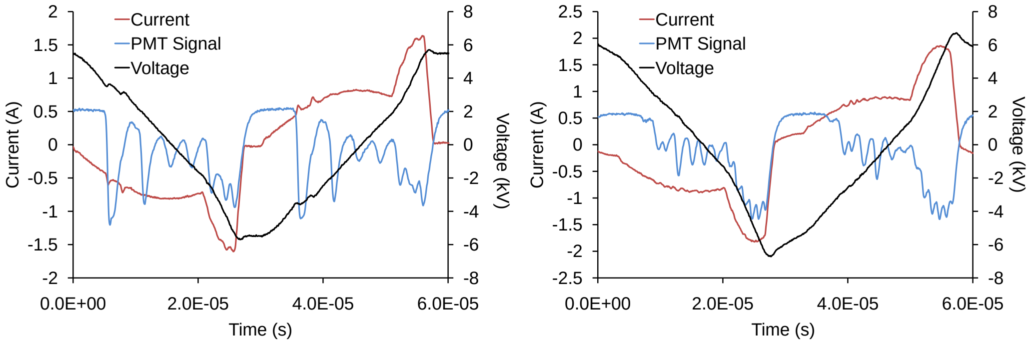

(a) Helium 1100W

(b) Helium/O_2 1600W

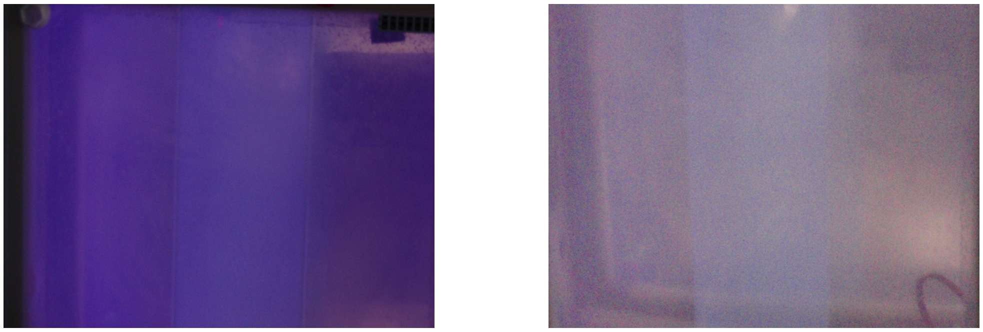

(c) Helium 1100W

(d) Helium/O_2 1600W

Figure 4.9: *In the figure (a) and (b) correspond to electrical (voltage (black), current (red) and PMT (blue)) signals of Helium and Helium/O_2 discharges at 1000W (He) and 1600W (He/O_2) applied power. The images in (c) and (d) were taken of the discharge corresponding to (a) and (b) respectively*

It must be stated that the current waveforms and PMT signals were highly periodic, with each discharge event occurring at the same point per half cycle and of similar amplitude. This indicates that the plasma mode in both chemistries is not of a filamentary or spark type, where the current waveforms display multiple discharge pulses of varying intensities and amplitudes, and do not necessarily occur at the same point per half cycle [2]. This type of discharge in which there are several temporally periodic discharge events occurring per each half cycle of the applied voltage was termed 'pseudoglow' in [38, 74]. Another feature of the pseudoglow discharge is that the discharge extinguishes upon the voltage reversal [38], this is also clearly the case here.

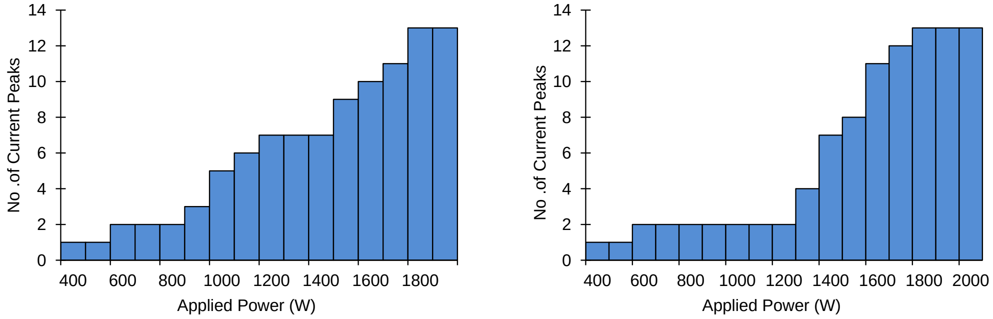

(a) Helium Discharge

(b) Helium/O_2 Discharge

Figure 4.10: *Number of discharge events occurring per half cycle of the applied voltage in Helium and Helium/O_2 discharges*

4.3.2 Discharge optical emission spectroscopy

Emission Spectra

Typical spectra for the He and He/O_2 discharges are shown in figure 4.11 for the spectral range 200-900 nm. The spectra were taken with an integration time of 125 ms and the analysis was performed on spectra which represent three averages of each spectrum.

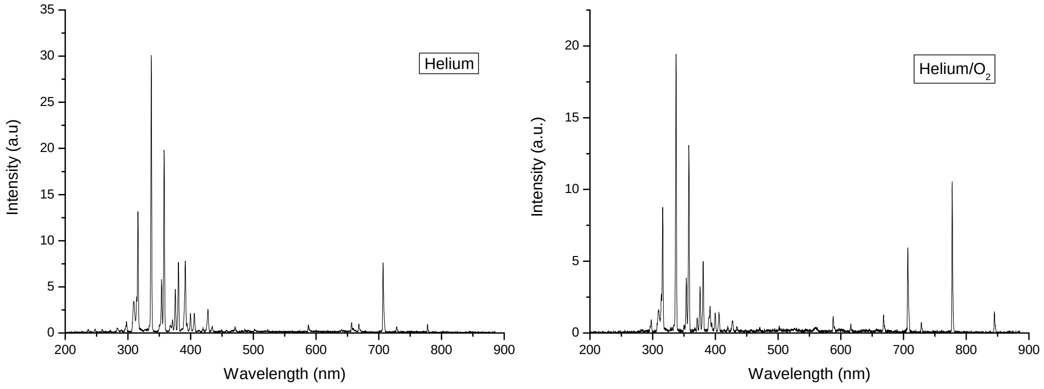

(a) Helium Discharge **(b)** Helium/O_2 Discharge

Figure 4.11: *Typical optical emission spectra for (a) Helium and (b) Helium/O_2 discharges in the 200-900 nm spectral range*

The discharge emission spectra consisted of atomic helium lines (667.8 nm, 706.5 nm and 728.2), emission from the second positive system of molecular nitrogen (337.1 nm, 399.8 nm and 405.9 nm), emissions from atomic oxygen (777.2 nm and 844.4 nm), atomic hydrogen (656.2 nm) and bands of the hydroxyl molecule (306 - 309 nm). The strong emission from the nitrogen, OH and hydrogen impurities are as a result of the diffusion of air into the plasma chamber. It was observed that, upon the addition of oxygen into the discharge, the overall emission from the other gaseous species was seen to decrease significantly whilst those of atomic oxygen showed a tenfold increase. The emission lines and systems considered in this analysis, together with the energies of the upper excited states, are listed in table 4.1 [83, 84].

TABLE 4.1: OPTICAL EMISSION SPECIES AND WAVELENGTHS

Species	Transition	Wavelength (nm)	E_B (eV)
He	$3^3S_1 \rightarrow 2^3P_{0,1,2}$	706.5	22.7
N_2	$C\ ^3\Pi_u \rightarrow B\ ^3\Pi_g$	337.1	11.1
N_2^+	$B\ ^2\Sigma_u^+ \rightarrow X\ ^2\Sigma_g^+$	391.4	18.7
O	$3p^5\ P \rightarrow 3s^5\ S^0$	777.2	11.0
OH	$A\ ^2\Sigma \rightarrow X\ ^2\Pi$	306 - 309	4.2

Variation in peak emission intensities with calculated discharge power

In this section the optical emission transitions of the atomic and molecular species within the two discharge chemistries are examined with respect to the power coupled through the discharge. The power coupled through the discharge was determined by the method set out in section 4.3.1. Figure 4.12 details the observed peak emission intensities of the optical transitions in table 4.1 with respect to the computed discharge power. The secondary vertical axis to the right in figure 4.12 corresponds to the emission from N_2 at 337.1 nm.

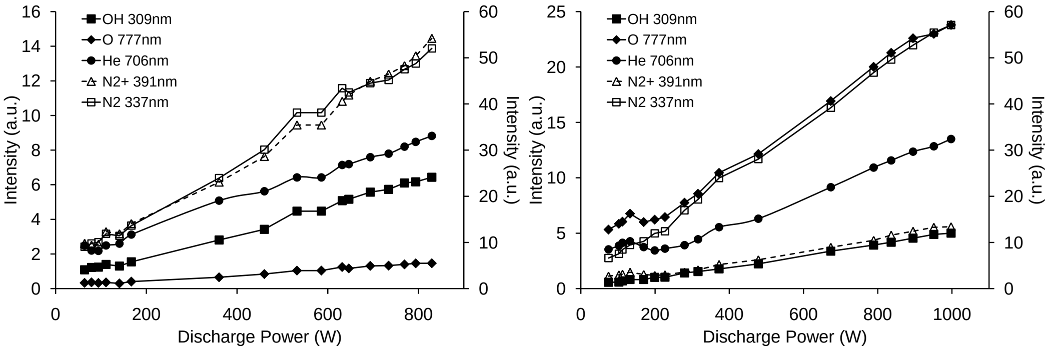

(a) Helium Discharge

(b) Helium/O_2 Discharge

Figure 4.12: *Variation in selected peak emission line intensities with computed discharge power in (a) Helium and (b) Helium/O_2 discharges: The secondary vertical axis to the right corresponds to the emission intensity of N_2 at 337.1 nm*

A linear least squares fitting was performed on the data presented in figure 4.12 to evaluate correlations between the evaluated discharge power and the discharge species optical emission. This fitting was divided into two parts. Below a discharge power of 200 W in the helium plasma corresponds to the point before the discharge is seen to undergo a change into a homogeneous operating mode (as discussed in section 4.3.1). Accordingly, a discharge power below approx. 400 W corresponds to the respective point in the helium/oxygen plasma. Therefore separate least squares fittings were performed on the optical emission data below and above these transitions in both plasma chemistries. The evaluated slopes and R^2 values of the fittings for the helium and helium/oxygen discharges are shown in tables 4.2 and 4.3 respectively.

Table 4.2: Linear least squares fit of discharge emission lines in helium discharge before and after transition point

Emission line (nm)	Before transition		After transition	
	Slope	R^2	Slope	R^2
706.5	7.125	0.654	8.032	0.987
337.1	40.83	0.889	55.77	0.965
391.4	11.76	0.820	17.22	0.989
777.2	0.349	0.140	1.765	0.974
306 - 309	3.648	0.797	7.856	0.986

Tables 4.2 and 4.3 reveal some interesting features associated with the mode transitions in both plasmas. Whilst the plasma is in the homogeneous mode, there is a strong linear correlation between the emission from each of the monitored species. This is shown through the R^2 values of the linear fitting in both chemistries. However, whilst the plasmas are in an unstable/filamentary mode, no clear linear correlation exists between the two. Interestingly, in the helium plasma, the emission from atomic oxygen (777.2 nm) shows the least correlation in the unstable mode whilst the emission from helium at (706.5 nm) shows the least correlation in the helium/oxygen plasma.

The slopes of the fitted lines also reveal distinct differences not only between each mode within the two plasma chemistries but also between the separate chemistries in their respective homogeneous modes. The variation in the emission from molecular nitrogen at 337.1 nm with respect to discharge power is similar in both discharges. However, the variations in the emissions from the other plasma species are quite different. Notably, the variation in the emission from the molecular nitrogen ion (N_2^+) at 391.4 nm in the helium plasma is almost three times that of the helium/oxygen plasma and the variation of emission from the atomic oxygen line at 777.4 nm is twenty times that in the 'pure' helium plasma.

Table 4.3: Linear least squares fit of discharge emission lines in helium/oxygen discharge before and after transition point

Emission line (nm)	Before transition		After transition	
	Slope	R^2	Slope	R^2
706.5	3.954	0.406	13.90	0.996
337.1	56.10	0.971	57.35	0.996
391.4	2.573	0.661	6.028	0.993
777.2	14.39	0.838	23.00	0.986
306 - 309	4.164	0.997	5.417	0.997

Determination of the gas temperature

In order to plasma treat temperature sensitive polymers, such as PET, it is of great importance that the plasma remains below temperatures at which polymer damage takes place. With this in mind the effect of increasing the applied power was measured with respect to the gas temperature. A measurement of the gas temperature was not possible in this chamber by conventional means e.g. a thermocouple, due to the tool modifications which would be involved and potential arcing problems due to a metallic probe being in the conducting gas. Therefore the gas temperature was measured by means of fitting of the rotational and vibrational spectrum of the high resolution spectrum of the N_2^+ ion to that of a simulated spectrum using the spectral simulation software LIFBASE [85]. An example of this spectral fitting is shown in figure 4.13.

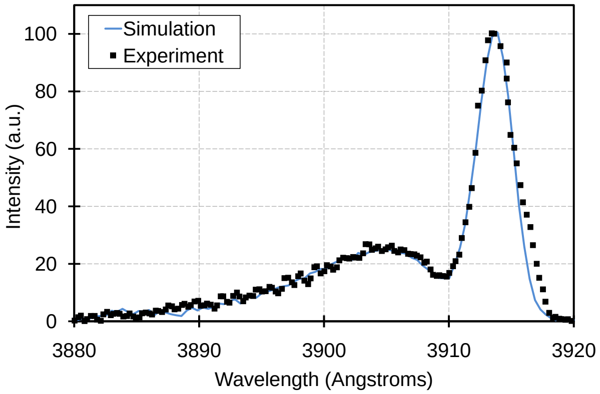

Figure 4.13: *Rotational Temperature Comparison*

Here it was assumed, due to the high collisionality of the heavy species at atmospheric pressure, that the ionic rotational temperatures and gas temperature are in equilibrium [86, 87]. Due to the reduced emission of the nitrogenous species at lower applied powers within the helium/oxygen discharge, it was not possible to perform the aforementioned curve fitting. However, the mea-

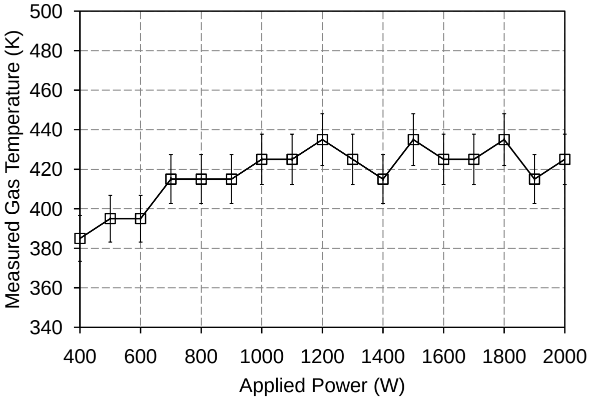

Figure 4.14: *Gas temperature versus applied power for helium discharge*

sured gas temperature is shown in figure 4.14 for the helium discharge. It was found that the gas temperature did not exceed 440 K, even at quite high input powers. This may represent an overestimation of the gas temperature as it was shown in [87] that the contribution to the rotational temperature can be influenced by charge exchange and metastable reaction with helium (equations 4.3 and 4.4. In [87] they found that the rotational temperature found by this method could be overestimated by approximately 30-60 K from that of the ground state nitrogen molecule, therefore a maximum gas temperature of 380-410 K may be more realistic.

4.4 Discussion

The results of the previous section show that two clear modes of operation of the plasma tool can be determined in both discharge chemistries. These can be divided into a microdischarge dominated, unstable mode at low powers, followed by a transition in which the microdischarge structures become more densely packed, through to a homogeneous mode where the microdischarges appear to coalesce. These modes have an effect on both the discharge chemistry and the electrical characteristics of the tool operation. Here explanations of these effects are proposed.

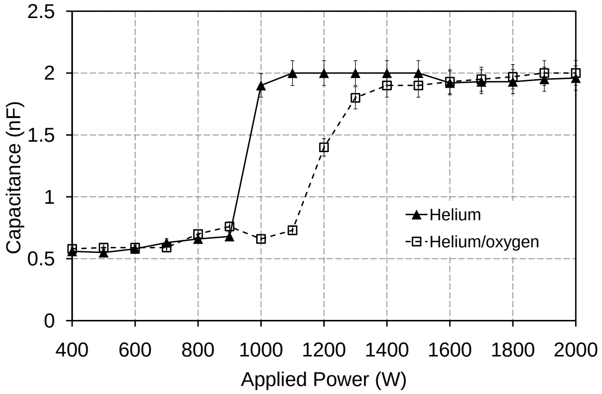

Figure 4.15: *Measured stray and dielectric capacitances versus applied power for the two discharge chemistries*

With respect to the input power into the system, there is a clear offset between the two discharge chemistries at which the transition from filamentary/microdischarge mode into a homogeneous mode occurs (cf. section 4.3.1). This transition takes place quite abruptly in the helium plasma (c. 900 W) and gradually (c. 1100 - 1500 W) in the helium oxygen plasma. The transition is accompanied by a shift in operating frequency of the tool as the frequency impedance matching occurs. The frequency shift can be explained by examination of the Lissajous traces of each of the plasma chemistries with respect to the applied power. From figure 4.3, the sum of the stray and dielectric capacitances may be determined from the slopes of lines (1 - 4) and (2 - 3) [79, 80]. The stray capacitance, due to cables etc. is assumed not to vary over time. Therefore, in figure 4.15 we have plotted the sum of the stray and dielectric capacitance for the two discharge chemistries.

In the figure, it can be seen that the calculated sum of the two capacitances follows an inverse trend to that of the frequency in figure 4.6a. Therefore the operating frequency decrease is explained by the conjugate matching of the capacitive reactance due to this capacitance variation. The capacitance variation can be explained by the increased charge deposition [75] on the dielectric barriers due to the increased surface density of the discharge as the microdischarges coalesce and the discharge becomes homogeneously distributed over the entire electrode area (see figures 4.7, 4.8 and 4.9). Also, the coupling efficiency of applied power into discharge power is maximised at this point.

Next we turn to the effect of these transitions on the optical emission from the selected plasma species (section 4.3.2 in the two plasma chemistries. In [75], it was proposed that the optical emission from the helium line at 706.5 nm is indicative of the presence of either electrons with energies greater than 2.9 eV or vibrationally excited He_2^+ ions and low energy electrons. Also in [86, 87], it was shown that the emission from the N_2^+ ion can be attributed to the following reactions in helium - air mixtures

$$He^* + N_2 \rightarrow N_2^+(B\ ^2\Sigma_u^+) + He + e \qquad (4.3)$$

and

$$He_2^+ + N_2 \rightarrow N_2^+(B\ ^2\Sigma_u^+) + 2He \tag{4.4}$$

Reaction 4.3 is Penning ionization of N_2 by helium metastables (19.82 eV) and reaction 4.4 is charge transfer between He_2^+ and N_2. Therefore the emission from each of these lines will contain information relating to the populations of the helium metastable states and molecular helium ions. Given that the emission intensities of the 706.5 nm line are similar in both discharges and the emission intensities of the 391.4 nm line are very different, we can assume that the populations of these states due to He_2^+ are not common to both.

An examination of figure 4.12 shows that in both discharge chemistries the dominant emission line is that of the emission of N_2 at 337.1 nm. The upper state of this transition is 11 eV and is populated by electron collisions with the ground state [75]. In the helium discharge, the dominant transitions other than the 337.1 nm line are those of the 706.5 nm and 391.4 nm lines, with weak emissions from the 777.2 nm oxygen line. In the helium/oxygen discharge, the emission from N_2^+ at 391.4 nm is much reduced whilst the 777.2 nm atomic oxygen line is the next dominant transition to the 337.1 nm line.

Looking to tables 4.2 and 4.3 we can see how the variation of the power coupled into the discharge effects the rate of change of emission intensity from the above emission lines. It has previously been proposed [22], that the helium metastables produced during a breakdown event are important in sustaining a homogeneous discharge in subsequent breakdowns due to the seed electrons generated through reaction 4.3 and the slowing down of streamer formation.

Also, Radu stated that helium metastable states lifetimes, at atmospheric pressure can be of the order 5μs [38]. This could provide an explanation for the non-homogeneity in the discharge of both chemistries at low powers, where the time between subsequent breakdown events is of the order of 20μs (cf. figure 4.7). However, whilst the discharge is operating in the homogeneous mode (figure 4.9, the maximum time between discharge pulses is c. 5μs.

The difference in the emission from the 777.2 nm line between both plasma chemistries indicates a greater dissociation of O_2 in the helium/oxygen discharge. In [27], it was proposed that the dissociation channel is through impact by metastable helium atoms. Helium metastable states can also be quenched through ionising interactions with both atomic and molecular oxygen [88]. This explains the difference in the rate of increase of the 777.2 nm line emission and 391.4 nm emission in both chemistries. We can assume a greater abundance of oxygen in the helium/oxygen discharge than nitrogen, therefore the helium metastables are more efficiently quenched by their interactions with the oxygen species. Given that oxygen forms negative ions quite readily, due to its high electronegativity, the discharge will be depleted of surplus electrons between successive breakdowns. This could explain why the microdischarge dominated plasma state persists in the helium/oxygen plasma to much higher input powers. This feature of helium discharges with added oxygen has been verified in numerical simulations by Lee et al. [89].

The rate of emission from the 706.5 nm, 337.1 nm line and OH molecule show similar trends in both chemistries. If the upper state of the 706.5 nm line is mainly populated through electron collisions with the ground state or excitation of helium metastables, we can assume that the electron temperature is not too dissimilar between the two chemistries. However, this cannot be easily confirmed due to the large contribution of heavy body collisions to the discharge spectra.

4.5 Conclusions

In this chapter we have applied a multi-diagnostic methodology, incorporating electrical and optical diagnostics, in order to characterise a pilot industrial scale atmospheric pressure plasma tool. The study was performed in both a helium plasma with a gas flow of 10 lmin^{-1} and with 1% oxygen additive. Through this study, two clear modes of operation of the tool were identified in both helium (He) and helium with 1% added oxygen (He/O_2) plasma chemistries. The discharge was seen to undergo a transition from a non-homogeneous to a homogeneous mode at input powers of 900W (He) and 1500W (He/O_2). These transitions were accompanied by corresponding transitions in the electrical and optical emission characteristics of the two discharges. Through analysis of the diagnostic results, explanations for the mode transitions and the corresponding variations in the discharge electrical and optical characteristics have been proposed. The efficiency of the power coupling into the discharge was found to be linked to the transition in operating modes. The variation in operating frequency of the tool has been attributed to increased surface charge deposition on the dielectric electrodes and a corresponding increase in the system capacitance due to a shift from non-homogeneous to homogeneous operating modes, through the use of charge-voltage Lissajous figures. Analysis of the discharge optical emission spectra revealed a transition from non-linear to linear variations of the emission spectra, with respect to applied power, attributable to the two operating modes. The optical emission spectra revealed that the Penning ionization of N_2 was suppressed in the He/O_2 and the dominant emission was from atomic oxygen. It was proposed that the increased production of atomic oxygen and quenching of helium metastable states accounted for the persistence of the non-uniform He/O_2 plasma mode to higher powers as opposed to that of the He discharge. Gas temperature measurements were performed by fitting of the high resolution rotational-vibrational experimental spectra to a simulated spectrum of the N_2^+ ion, under the assumption that the gas and rotational temperatures are in equilibrium. It was found that the gas temperature did not exceed 380-410 K in the helium discharge. Given the melting point of the PET material used here (c. 533K), the gas temperature should not be sufficient to cause polymer damage whilst being treated. The results presented here hold importance in the application of this tool to polymer surface modifications.

CHAPTER 5

Development of a real time diagnostic and multivariate method for long term characterization of atmospheric dielectric barrier discharges in various atmospheres

5.1 Introduction

Since pioneering work by Okazaki et al [21], research into atmospheric pressure dielectric barrier discharges has concentrated on the stability of the homogeneous or, so called, atmospheric pressure glow discharge (APGD), under various operating conditions. The discharge is generally initiated and maintained by a low frequency [21, 22] or pulsed DC voltage [90] applied across metallic electrodes, of which one or both are covered by thin dielectric material. The introduction of a dielectric barrier between the electrodes and the discharge gap prevents the formation of a thermal arc through current limitation [2, 14].

The stability, homogeneity and efficiency of helium based APDBDs have been shown to be sensitive to: the frequency of the applied voltage [3, 22, 38, 45, 91, 92], dielectric barrier thickness and material [37, 45], the amplitude of the voltage applied to the gas gap [23, 38, 45, 92], gas impurity and gas mixture concentrations [66, 89, 91, 93–97], gas flow rates [75, 98] and external circuit effects [45]. The experimental parameters are generally examined through post analysis of the experimental results and using bivariate correlative techniques [22, 67, 75].

Frequently, plasma treatments do not involve a single chemical species or process step [7], therefore a study of the dynamics of the discharge behaviour over time is necessary to ascertain the impact of the plasma produced species and gas or chemical admixtures on the electrical parameters and vice versa. Such studies provide system identification and facilitate future process control measures together with aiding reproducibility.

Whilst extensive research has been carried out into the factors presented above, little work has been performed in monitoring longer term temporal effects associated with APGDs, with notable exceptions being a recent study by Shin and Raja [47] and that of Gherardi et al [99]. In [47], no spectroscopic evidence was presented to evaluate variations in the electrical current characteristics, which were attributed to changing surface properties. Their arguments were verified by changing the effective secondary electron emission coefficient of a zero dimensional model [90] to correlate with varying surface properties. The variations presented in [99] were evaluated over relatively shorter time scales and were performed solely in nitrogen gas.

Consequently, in keeping with the ethos of exploiting the APDBD properties, i.e. reduced costs and ease of continuous materials processing [1, 2], this study presents the design of a low cost, real time, PC based optical and electrical monitoring diagnostic. The PC based diagnostic is used to extract latent electrical and optical information associated with the temporal operation of a APGD source over time and in various atmospheres. The electrical and optical parameters of an APDBD in helium gas and helium with admixtures of both nitrogen and oxygen are synchronously monitored over a period of 30 minutes in order to evaluate changes in discharge electrical and optical parameters.

Although multivariate and machine learning techniques have been routinely employed in low pressure plasma processing for many years [100, 101] and more recently fusion reactors [102] with much success, little work has been done using such techniques in atmospheric pressure systems. Therefore included in this work, is the novel implementation of multivariate principles to examine mutual correlations between each of the measured optical and electrical datasets of the APDBD also to enable rapid characterisation of the discharge from large datasets. Finally, we compare the results of these investigations to previous modelling work and experimental results to establish reasons behind the correlations extracted by the multivariate principles.

5.2 Experimental apparatus and diagnostic set up

5.2.1 Experimental apparatus

The experimental apparatus which was examined in this work is detailed in figure 5.1 and as discussed in chapter 3. The circular, planar electrodes are made of stainless steel and are 44 mm in diameter. The top electrode can be adjusted in the vertical plane, in order to vary the gas gap whereas the bottom electrode was fixed. In the present work, the gas gap was fixed at a distance of 5 mm. The surface of each of the electrodes was covered by a 1 mm thick, 96%, alumina dielectric barrier, which extended over the surface of the electrodes to prevent arcing between the metallic electrodes underneath.

The dielectric barriers were coupled to the metallic electrodes using vacuum grease thus preventing microdischarges from occurring between the minute gaps between the electrode-dielectric interfaces. The electrode assembly was housed in an air tight, stainless steel chamber. Helium gas (99.9996% purity, Air Products) may be flowed through the chamber, by means of a mass flow controller, from 0.5 to 20 standard litres per minute (slm). A second mass flow controller (0-0.5 slm) is used to flow admixtures of 0.1% nitrogen and

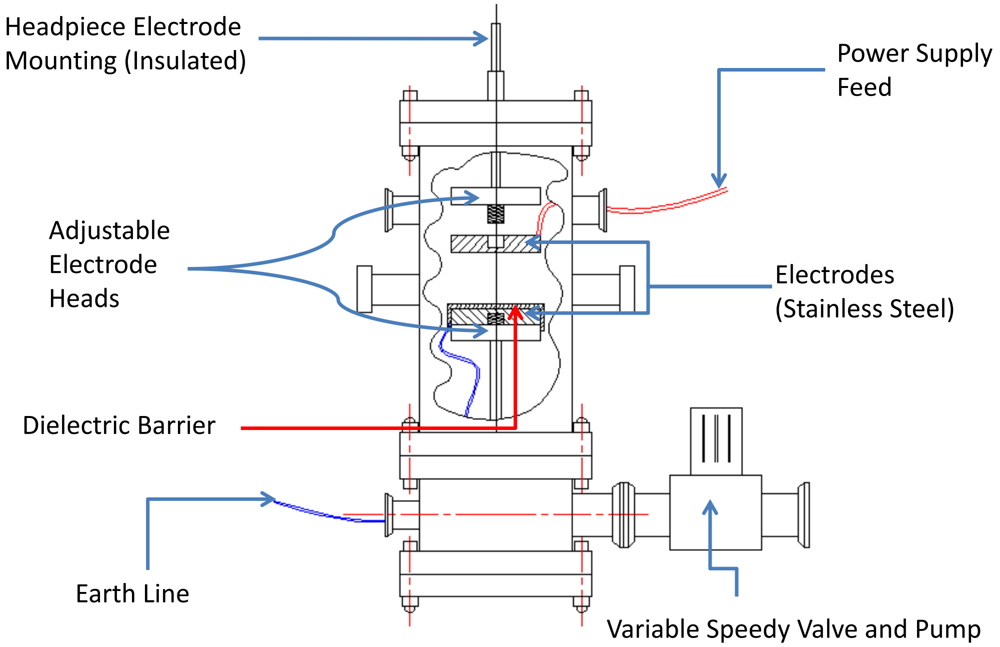

Figure 5.1: *APDBD chamber construction*

0.1% oxygen also.

5.2.2 Diagnostic set up

The power supply was used to apply a sinusoidal high voltage (5-60 kHz, 0.7-3 kV) to the driven electrode, whilst the lower electrode was grounded. The applied voltage was measured by means of a high voltage probe whilst the total discharge current was measured across a 50 Ω resistance in series with ground. The current and voltage signals were transferred to an oscilloscope (Tektronix 3034B, 400 MHz and 3 GSs^{-1}) which was connected to a data acquisition PC

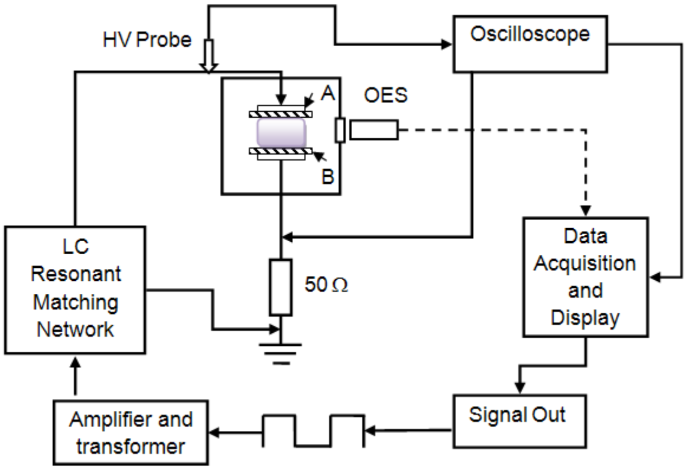

Figure 5.2: *Diagnostic set up of dielectric barrier discharge chamber*

to analyse and process the signals in real time. Light emission signals from the plasma bulk were coupled through a 500 μm optical fibre to an Ocean Optics USB4000 spectrometer, set to an integration time of 500ms, (spectral range 300-1100nm, and spectral resolution 0.75nm) which was interfaced to the data acquisition PC in order to monitor the time averaged discharge spectral light emission in real time also. Together with optical emission, images of the discharge were taken using a Nikon digital SLR 3000 camera with a 1 ms shutter speed to determine the time averaged structure of the discharge, over a number of cycles, under the varying operating conditions. The diagnostic set up is detailed in figure 5.2.

5.3 PC based real time diagnostic monitor

5.3.1 Discharge electrical model

In references [3, 22, 23], it was shown that APDBDs are characterised by a single current pulse per half cycle of the applied voltage to the discharge. The temporal evolution of the current pulse is associated with the breakdown of the gas gap, formation of the APDBD and extinguishing of the APDBD through an opposing field generated by the deposition of electrons on the anode.

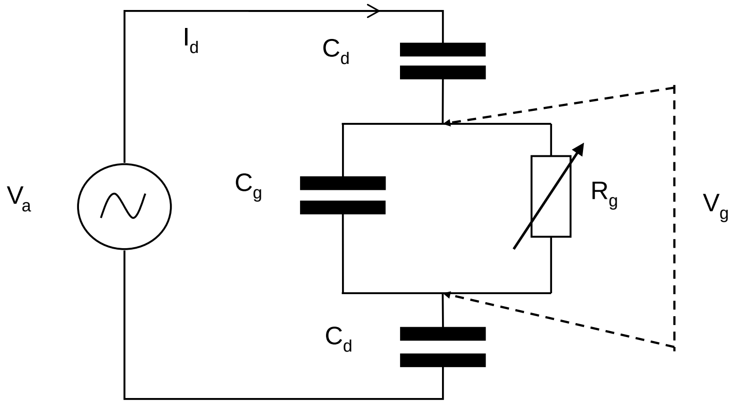

Figure 5.3: *Equivalent electrical circuit of the APDBD*

With knowledge of these characteristics, the discharge can be modelled as the electric circuit shown in figure 5.3. In the figure , V_a is the applied voltage, C_d represents the capacitance due the dielectric barrier, C_g is the capacitance due to the discharge gap and R_g is the dynamic resistance associated with the change in conductivity of the gas gap. I$_d$ is the discharge current. The resistance of the gap decreases dramatically when the gas gap breaks down and is significantly greater whilst the discharge is not in the breakdown phase.

The gas gap voltage, V$_g$, is found by following the method set out in reference [22], since this is not directly measurable in the system. The voltage across the gas gap is given by

$$V_g(t) = V_a(t) - V_m(t) \tag{5.1}$$

Where V$_a$(t) is the applied voltage and V$_m$(t) is the memory voltage across the dielectric barriers which can be found from

$$V_m(t) = \frac{1}{C_{tot}} \int_t^{t+T} I(t)dt + V_m(t_0) \tag{5.2}$$

In equation 5.2, C$_{tot}$ is the capacitance due to the series combination of the dielectric barriers, I$_d$(t) is the discharge current and V$_m$(t$_0$) is the memory voltage due to charge deposition during the previous discharge, which is calculated by ensuring that the average of the gas voltage over a number of cycles reduces to zero. The integral is performed over each cycle of the discharge current.

The capacitance of the dielectric barriers, in the present work, was determined by assuming the applied voltage was coupled to the dielectric through the electrode-dielectric interface. Given that the relative permittivity, ϵ_r, of the alumina was equal to 8.5, an electrode radius, r, of 22mm and dielectric thickness, d, of 1 mm, the total capacitance of the series dielectric barriers is found by

$$C_{tot} = \frac{\epsilon_r \epsilon_0 \pi r^2}{2d} \tag{5.3}$$

where ϵ_0 is the permittivity of free space and C_{tot} is found to be approximately 57pF. This calculation was validated by measuring the capacitance by means of a capacitance meter with the electrode faces placed flush against each other.

5.3.2 Real time discharge monitor and electron density estimation

In section 5.2.2 it was illustrated that within the current experiments, the applied voltage and discharge current are monitored and transferred to the oscilloscope by means of a high voltage probe and 50 Ω resistor. A number of current voltage cycles are read and transferred to a PC, by means of an IEEE interface, from which the discharge characteristics are determined and displayed using a specially written LabVIEW™ software program.

The applied voltage, discharge current, memory voltage and gas gap voltage are displayed on the graphical user interface (GUI) through the solution of equations 5.1 and 5.2 in real time. Typical electrical waveforms are shown in figure 5.4. Initial observation and monitoring of these waveforms is used to determine the mode of operation of the plasma i.e. glow [22], filamentary [22, 37] or pseudoglow [38]. Also, through monitoring of the gap voltage, the overvoltage condition can be identified and the magnitude of the driving voltage may be reduced to prevent the over voltage to filamentary/multipeak

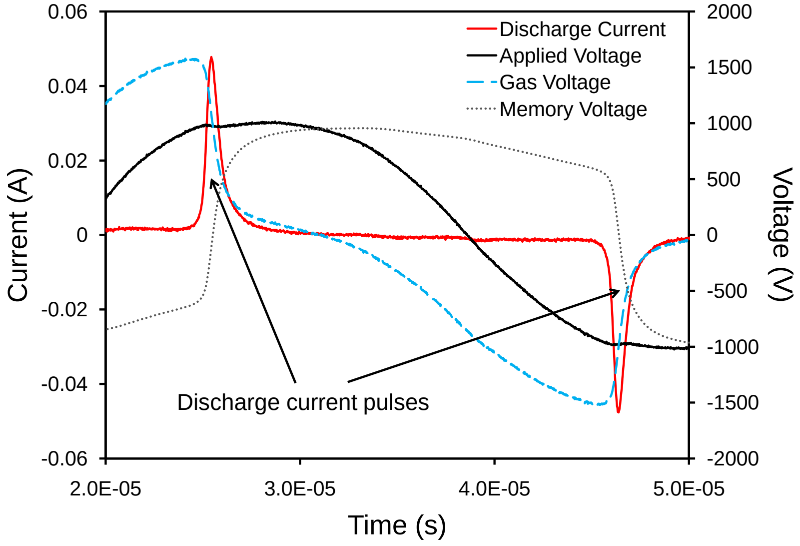

Figure 5.4: *LabVIEW™ example figure*

discharge transition [92]. This enables the first stage of control over the discharge homogeneity.

Once the gas voltage has been determined the average discharge power, P_d, over one period, T, may be calculated using

$$P_d(t) = \frac{1}{T}\int_t^{t+T} V_g(t)I_d(t)dt \tag{5.4}$$

In order to estimate the volume averaged electron density, n_e, within the discharge we use equation 5.5 [2, 12], under the assumption that the majority of electrons dissipate energy through elastic collisions within the volume.

$$\frac{P_d}{V} = \frac{J^2}{\sigma} = \frac{m_e \nu_c}{e^2 n_e} J^2 \Rightarrow n_e = \frac{m_e \nu_e V}{e^2 P_d} J^2 \tag{5.5}$$

In 5.5 , V is the discharge volume, σ the bulk conductivity, m_e the electron mass, e the electronic charge, ν_c the electron collision frequency in helium, at atmospheric pressure, ($\sim 1.8 \times 10^{12} s^{-1}$ [1]), and J is the discharge current density. The electron densities ranged from approximately 2x10^{9}cm^{-3} to 5x10^{10}cm^{-3} through the course of the experiments.

5.4 Characterization of the APDBD source

5.4.1 Electrical and optical characteristics

To evaluate the temporal electrical characteristics of the APDBD system it was chosen to monitor and examine variations in the applied power, the average discharge power, the peak discharge power, the applied voltage which results from the original voltage drop across the electrodes, the gas breakdown voltage, the memory voltage, the peak discharge current, the peak electron density and the operating frequency. In the experiments the frequency was initially maintained at 26 kHz but was seen to vary as the discharge operated over time.

The optical emission characterization is performed by analyzing fluctuations in the Helium transitions at 706.5 nm, 668 nm and 728 nm, the second positive system (SPS) of molecular nitrogen N_2 ($C^3\Pi \rightarrow B^3\Pi$) transitions at 337.1 nm, 353.6 nm, 357 nm 375 nm and 380 nm, emissions from atomic oxygen O at 777.4 nm and 844 nm, hydrogen H at 656.2 nm and the hydroxyl radical OH ($A \rightarrow X$) transition at around 309 nm [7, 103]. We also monitor the first negative system (FNS) N_2^+ $(B^2\Sigma_u^+, \nu_B = 0) \rightarrow N_2^+(X^2\Sigma_g^+, \nu_X = 0)$ transitions at 391.4 nm and 427.5 nm [86]. A typical emission spectrum is shown in figure 5.5. Data was also collected on the ratio of the line emissions between the 391.4 nm line and the 337.1 nm line (N_2^+/N_2). A typical optical emission spectrum is shown in figure 5.5.

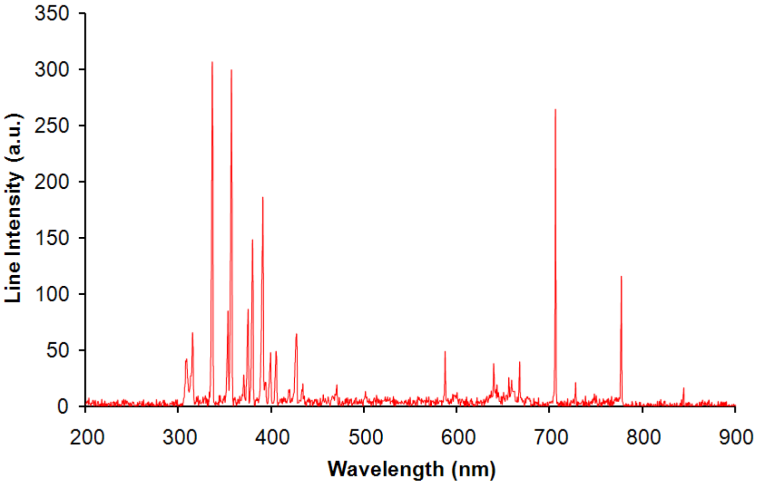

Figure 5.5: *Typical optical emission spectrum from the APDBD chamber*

Initially, the chamber was evacuated to a base pressure of 50 mTorr before the introduction of helium gas, which was allowed to flow for 30 minutes at a flow rate of 20 slm. The flow was then reduced to 6 slm before a 5 kV peak to peak sinusoidal high voltage was applied to the electrodes and the discharge formed. The value of 5 kV was chosen as a stable discharge occurred when this voltage was used across all of the experimental conditions. This process was repeated before the addition of the gas admixtures of 0.1% nitrogen and 0.1%

oxygen also. Each of these experimental conditions were repeated four times and data taken from the moment the discharge was struck for a period of 30 minutes (or 30 minutes from the addition of the gas admixtures when used). As has been shown previously [47] and in shown in figure 5.6, the discharge parameters evolve over periods of some tens of minutes (although the residence time in the 1.6 litre chamber here is approximately fifteen seconds), therefore the current experiments are designed to examine the temporal variations of these parameters both under steady state conditions and as the gas admixtures fill the chamber.

Each data capture was performed at an interval of 500 ms, the value of which was determined by the integration time of the spectrometer giving a total of 3600 data captures per experiment.

5.4.2 Determination of correlation coefficients

Given the large amount of variables and datasets, the analysis of the experimental data through bivariate techniques would be extremely difficult. We have recently shown that multivariate techniques can prove extremely useful in atmospheric pressure plasma diagnostics [104]. Therefore the data is analyzed according to the following. The entire datasets for each experiment are used to build a $m \times n$ matrix with each column, n, representing the variables and each row, m, an observation. The correlation coefficients between each variable are then used in establishing the dependence of two variables relative to one another.

The covariance of two data sets, X and Y, of length, n and mean values, $\bar{X}$ and $\bar{Y}$ is given by

$$cov(X,Y) = \frac{\sum_{i=1}^{n}(X_i - \bar{X})(Y_i - \bar{Y})}{(n-1)} \tag{5.6}$$

The covariance matrix, $C^{n\times n}$, between several sets of data is then found by computing the covariance between each individual dimension (columns) of the data, Dim_i i.e.

$$C^{n\times n} = c_{i,j} = cov(Dim_i, Dim_j) \tag{5.7}$$

However the covariance matrix does not consider the relative contribution of each set of values i.e. large values contribute more to the magnitude of the covariance value. To obviate such effects a normalization procedure is used which establishes the correlation coefficient matrix, $R_{i,j}$.

$$R_{i,j} = \frac{c_{i,j}}{\sqrt{(c_{i,i})(c_{j,j})}} \tag{5.8}$$

The correlation coefficient matrix elements, $R_{i,j}$, describe the strength of the dependence between Dim_i and Dim_j of the original dataset. The values of $R_{i,j}$ range from -1 to 1 with a score of 1 indicating a positive dependence i.e. as one quantity increases or decreases so does the other, whilst a score of -1 indicates a negative dependence i.e. as one quantity increases the other decreases or vice versa. A score of zero indicates that either the two datasets are completely unrelated or the relationship is non-linear or complex [105]. This analysis allows us to rapidly establish correlations amongst the measured parameters.

5.5 Results and discussion

Here results are presented of the experiments described above. Although all of the discharge electrical parameters detailed in section 5.4.1 were monitored through the course of the experiments, the analysis presented here involves what we consider to be the most important parameters associated with the operation of the discharge i.e. the gas breakdown voltage, the peak discharge current, the average discharge power and estimated electron density and their correlations to the optical emissions discussed in the previous section. Throughout the analysis we will differentiate between admixture and impurity in the sense that impurity level is not a controlled parameter and is expected to be present in the 10-100 ppm range whilst the admixture is controlled and exists in the 100-1000 ppm range.

Furthermore, it is immediately obvious from figure 5.7 that, in the case of the helium discharge, the correlation scores for the optical emissions are extremely similar across each of electrical parameters. This would imply that arguments presented for the reasons behind these scores are similar across the range. However it is also clear that this is not the case of helium discharge with gas admixtures.

The justification for the use of the correlative scores can be seen in the examples of figure 5.6 in which comparisons between the peak discharge current in a He discharge (correlative score close to -1) and the breakdown voltage in a He/N_2 discharge (correlative score close to 1) to the evolution of the emissions from the SPS of N_2.

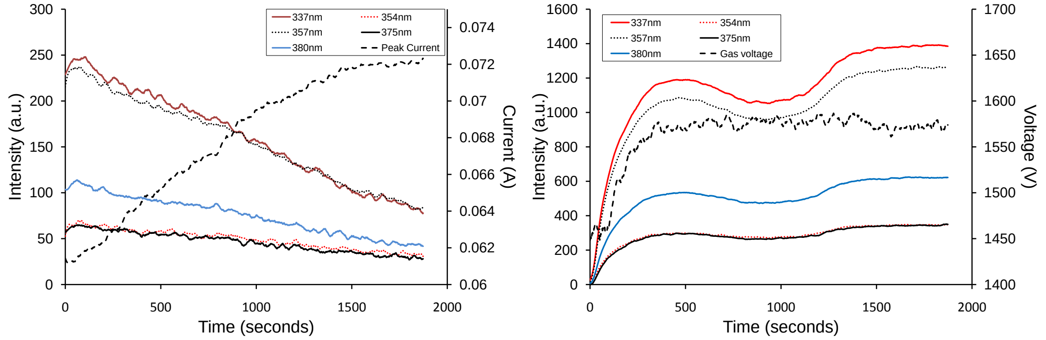

(a) Peak current and SPS emissions in helium **(b)** Gas voltage and SPS emissions in He/N_2

Figure 5.6: *Variation in the current, in a He discharge, and gas voltage, in a He/N_2 discharge with respect to emission from the SPS of N_2*

In order to evaluate the results, knowledge of how the respective species emissions are produced in the discharge is necessary. The excited OH radicals are produced through heavy body collisions through the following reactions [96]

$$He_2^+ + H_2O \rightarrow OH(A) + He^+ + He + H \tag{5.9}$$

$$e + H_2O^+ \rightarrow OH(A) + H \tag{5.10}$$

Where the H_2O^+ ion is created either by molecular or atomic helium metastables according to

$$He_2^* + H_2O \rightarrow 2He + H_2O^+(X, A, B) + e \tag{5.11}$$

$$He^* + H_2O + He \rightarrow 2He + H_2O^+(X, A, B) + e \tag{5.12}$$

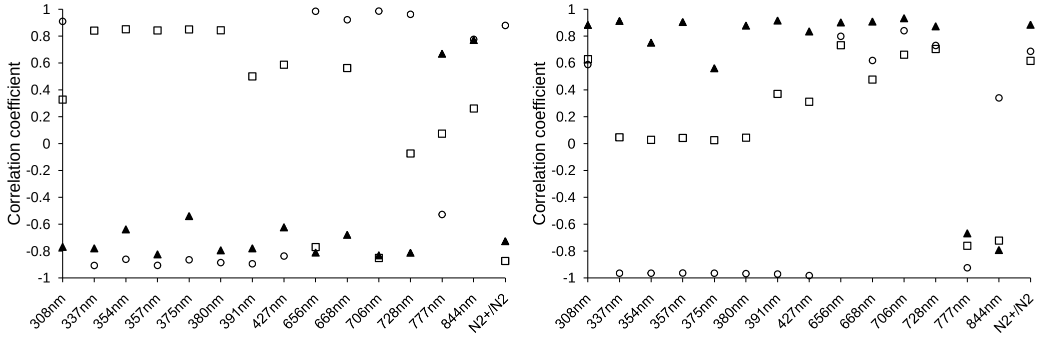

(a) Gas breakdown voltage scores **(b)** Peak discharge current scores

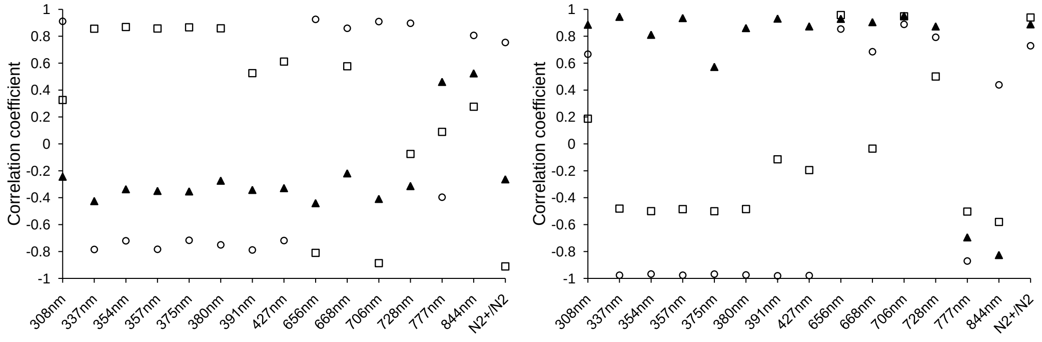

(c) Average discharge power scores **(d)** Electron density scores

Figure 5.7: *Correlation coefficient scores between the APDBD electrical and optical parameters and the gas breakdown voltage. In the figure, ○, represents the 'pure' helium coefficients, □, the He/N_2 scores and, ▲, the He/O_2 scores. The respective plasma emission lines on the horizontal axis are as described in section 5.4*

The upper level of the 706.5 nm emission line is populated either through direct electron excitation, metastable collisions or through dissociative recombination of molecular helium ions [75] i.e.

$$He_2^+ + e \rightarrow He^* + He \rightarrow 2He + h\nu \tag{5.13}$$

In discharges of excess helium with nitrogen additives the molecular nitrogen ions are created efficiently through the Penning process [86]

$$He_m + N_2 \rightarrow N_2^+(B^2\Sigma_u^+) + He + e \tag{5.14}$$

and through charge charge exchange reactions with molecular helium ions [86]

$$He_2^+ + N_2 \rightarrow N_2^+(B^2\Sigma_u^+) + 2He \tag{5.15}$$

5.5.1 Average gas breakdown voltage

In this section analysis is presented for the results of the correlation coefficients from the set of experiments for the average gas breakdown voltage. From figure 5.7 it is clear that, in the case of the He and He/N_2 chemistries, the lines of the SPS of nitrogen (337 - 380 nm) score almost equally and can therefore be considered collectively whilst, in the case of the He/O_2 chemistry, some lines score more heavily than others. Also it is obvious that the increased emissions from each of these lines coincide with a decrease in the gas breakdown voltage in the case of the He and He/O_2 chemistries whilst the converse is true of the He/N_2 discharge.

In the He discharge, the breakdown voltage increases along with the N_2^+/N_2 ratio. In [75] the gas voltage maximum approximately coincides with the

N_2^+/N_2 maximum also. They attributed the N_2^+/N_2 maximum to an increase in the charge transfer reaction 5.15 thus depleting the molecular nitrogen concentration. The breakdown voltage shows a strong positive correlation to the emissions from He, OH and the 844 nm line of atomic oxygen in the helium discharge whilst there exists a negative correlation to the He and OH emissions in He/O_2 and positive correlations to the oxygen emission lines. The results for the He/N_2 discharge show decreases in the gas voltage coincident to increases in emissions from the 656 nm and 706.5 nm lines. The relation between the other parameters in the discharge emission spectra score quite low and a non-linear or null relation may be involved.

Given the large helium excitation energies, the He lines, He metastables, He ions and OH production is favored by large electron temperatures under higher fields. The initial production of the He ions and metastables occurs just after breakdown [75, 96] and hence an increased breakdown voltage correlates with the increases in the emissions from the helium lies, N_2^+/N_2 ratio and OH and H lines in the helium discharge.

However, with the increased concentration of molecular gases in the helium admixtures a decrease in these lines may be indicative of decreased atomic and molecular helium metastable/ionic production. The N_2^+ is rapidly converted to N_4^+ in higher N_2 concentrations [66] and a similar reaction occurs in He/O_2 [97]. These ions are subject to rapid dissociative recombination under low fields [66, 97] and decrease the concentration of electrons as the next discharge occurs. The high electronegativity of oxygen will also obviously have a part to play here as the production of negative ions in the discharge is increased by one to two orders of magnitude when increasing the O_2 content from 100 ppm to 1000 ppm [97]. The surplus electrons produced by the metastable species in the afterglow can facilitate subsequent breakdowns under lower fields in helium/impurity mixtures [22] and hence the correlation is negative. Indeed in the model of Martens [66] it is shown that, as the amount of N_2 is increased from 100 ppm to 1000 ppm, the gas breakdown voltage is increased by some 200 V. Moreover, the smaller score for the emission from the hydroxyl radical in He/N_2 may be attributed to the competing mechanism of a large amount of molecular nitrogen excitations in this region of the spectrum.

5.5.2 Average discharge power

The trends for the He, He/N_2 and He/O_2 discharge optical emissions with respect to the average discharge power are similar to those for the breakdown voltage for each of the species examined (c.f. figure 5.7). There are slight differences however in the case of the He/O_2 discharge where the correlation scores tend further towards zero. However this implies that, particularly in the He and He/N_2 discharges, similar interactions amongst the chemical species within each of the discharges are common to variations in each of these electrical parameters.

As with the gas breakdown voltage, the production of excited species immediately following the gas breakdown and in the afterglow, following the main current pulse, will clearly impact on the average discharge power coupling. Here the high score for the relation between the SPS in the He/N_2 discharge is indicative of increased power coupling into collisions with the molecular gas and its vibrational states, which can occur under both low and high field conditions [7]. This would explain the positive score for the atomic oxygen lines in the He/O_2 discharge together with the negative dependency on the other emission lines, as under increased oxygen addition it would be expected that a significant amount of the energy from excited species and electrons will be coupled into elastic and vibrational collisions together with quenching of metastable states [7, 88]. Furthermore, the overall average discharge power, over the course of the experiments, increased by an average of 11% and 19% in the helium and He/N_2 discharges respectively whilst it increased by only 3.5% in the He/O_2 discharge and hence the correlative score is less strong in the He/O_2 discharge.

5.5.3 Peak discharge current

Next we turn to the results of the correlation coefficient scores for the emission lines with respect to the peak discharge current. Interestingly, the correlation scores for the SPS emissions in the case of the He/N_2 discharge are all close to zero whilst for the He/O_2 discharge a strong positive correlation exists. Another interesting feature of figure 5.7 is that the correlation scores for the bulk of the species emissions in the He/O_2 plasma are inverted to the corresponding case for the gas breakdown voltage scores. Therefore, in the case of the He/O_2 discharge, the maximum peak discharge current corresponds to when there is a lesser oxygen content in the discharge and is most probably due to increased electron attachment under increasing oxygen content together with metastable quenching [88].

High positive scores are seen in the case of the N_2^+/N_2 emission ratio, OH, 706.5 nm line and H line for each discharge chemistry also. In Stalder's model [95], it was shown that for a discharge in 300 Torr helium with 850 ppm of air, the peak He^+, He_2^+ and N_2^+ production occurs around 1-2μs after the gas breakdown and hence approximately coincides with the current peak. Therefore the positive scores for the lines mentioned above, with respect to the peak discharge current, can be attributed to reactions 5.9, 5.13 and 5.15.

The almost zero scores for the SPS of nitrogen in the He/N_2 discharge can be analyzed through inspection of figure 5.8 in which the current is primarily observed to decrease upon addition of nitrogen into the chamber but then increases and approximately maps to the SPS emissions after a rather long time scale of around 1000 seconds.

5.5.4 Peak electron density

It has been shown through time resolved optical emission spectroscopy [96] that the most intense emissions from the FNS and SPS spectral lines in a helium discharge with nitrogenous impurities coincides with the maximum

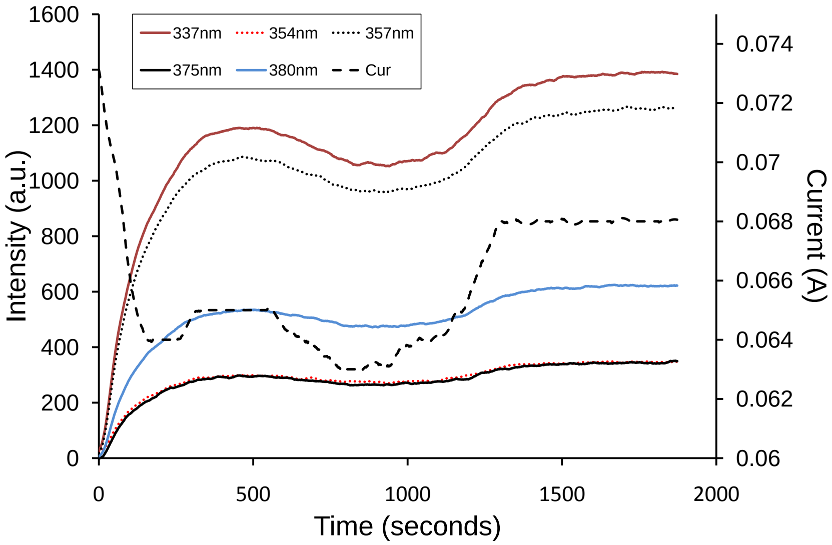

Figure 5.8: *Variation in peak discharge current in the He/N_2 discharge with respect to emissions from the SPS of N_2*

generation of charged species and hence the peak in the current pulse, whilst the emissions from the helium lines slightly precede these. Therefore the maximum in the N_2^+/N_2 ratio is indicative of the most efficient production of molecular nitrogen ions from the available molecular nitrogen and hence as this is maximized so too will be the electron density in low impurity helium discharges.

The electron density is maximised when the nitrogenous impurity levels of the helium discharge are low. Also increased amounts of nitrogen in the He/N_2 discharge, from 100 ppm to around 300 ppm, have been shown to slightly increase the electron density whereafter it begins to fall [66]. This can explain why the correlation between the emission of the SPS in the admixed nitrogen does not have as low a correlative score.

In [97], it is shown that the addition of around 100 ppm of oxygen to a helium discharge coincides with the maximum in the electron density and above 200 ppm or greater causes the electron density to decrease due to the destruction of metastable species which create positive ions and electrons through the Penning reaction

$$He_m + O_2 \rightarrow O_2^+ + He + e \tag{5.16}$$

At elevated levels of O_2 addition, attachment becomes the primary electron loss mechanism and impact ionization the primary electron generating mechanism [97]. Therefore a coincidence is seen between the scores for emission from the nitrogenous impurities and the helium excited states together with the emission from the OH radical through the reactions in section 5.5.

There are two further details associated with the scores in each part of figure 5.7. The clustering of the first negative system (391.4 nm and 427.5 nm) line scores and that of the 668 nm emission of helium in the He/N_2 discharge is interesting. It was shown by Arkhipenko [76] the n=2 states of excited helium are efficiently quenched and contribute to the N_2^+ density which in turn emits into the FNS at N_2 admixtures of the same order here. Therefore similar scores reflect the contribution of the 668 nm line to the N_2^+ density in the admixed nitrogen discharge. Indeed, it was found by inspecting these emissions that they followed the same trends.

Also, in the helium discharge, the scores for the 777 nm line and 844

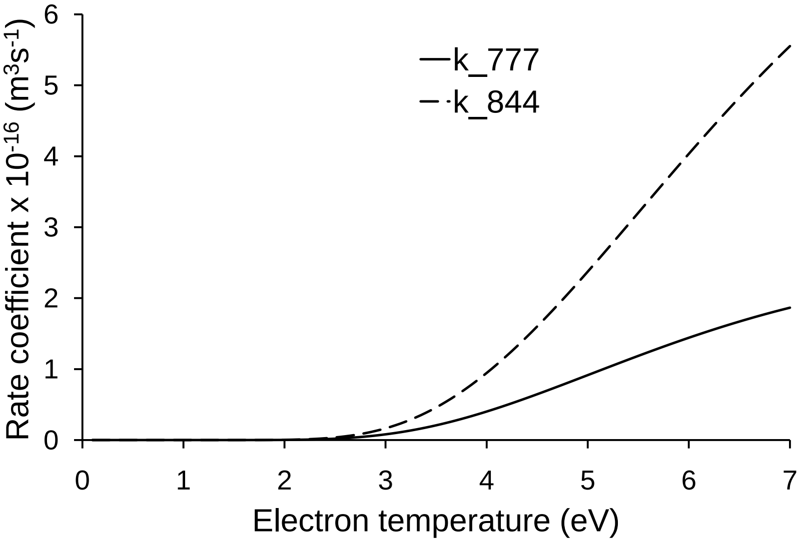

Figure 5.9: *Rate coefficients for the electronic excitation of the upper levels of the 777 nm and 844 nm lines of atomic oxygen assuming a Druyvestynian EEDF*

nm lines are very different. The 844 nm emission appears to be correlated to increased emissions from the helium excited species and the N_2^+/N_2 ratio whilst the converse is true of the 777 nm emission.

This could be attributed to the temperature dependency of the rate coefficient for the electronic excitation of the upper state of the respective transitions, which is shown for a Druyvesteynian electron energy distribution [12] in figure 5.9. The cross sections were taken from [106]. It can be seen in this figure that the excitation of the upper state of the 844 nm transition is favored over the 777 nm upper state at increasing electron temperatures. Given that elevated electron temperatures are expected at low impurity and high helium concentrations (c.f. section 5.5.1) it would seem reasonable to assume that this would account for the difference.

5.6 Conclusions

In this chapter a real time PC based optical and electrical parameter monitoring diagnostic for atmospheric pressure discharges has been developed. The efficacy of the diagnostic methodology has been demonstrated, through characterization of the temporal behavior of a helium dielectric barrier discharge in 'pure' helium gas and in helium with 1% admixtures of both N_2 and O_2 respectively, over a period of 30 minutes. It was found that establishing correlations amongst the large experimental datasets to be efficiently expedited through the novel application of multivariate statistical anlaysis on the data groupings. Comparison of the results of these correlations with current modelling work and past experimental results, together with other analyses demonstrates the effectiveness of the approach.

The extension of the technique to process monitoring and characterization in other gases, particularly in industrial atmospheric plasma systems, is natural and would facilitate efficient run to run comparison, process identification and correlation with process outputs. These will be the expected outcomes of future work and development of the diagnostic.

CHAPTER 6

Passive acoustic diagnostics of an atmospheric pressure linear field jet including analysis in the time-frequency domain

6.1 Introduction

Contemporary studies of APLFJs have focused on the effects variations in the discharge parameters, particularly the gas flow rate, applied voltage and voltage pulse width, have on the linear field jet plume and its chemistry [50, 57–60, 62–64, 107]. Traditional diagnostics of the plasma jets generally incorporate ICCD imaging [57, 62, 107], current and voltage analysis [59, 63, 107] and optical emission spectroscopy [55, 60, 62–64].

However, such diagnostics also have certain drawbacks. ICCD imaging is costly and relatively difficult to realize, whilst some systems, particularly those in an industrial setting, may not facilitate the installation of current and voltage probes to monitor the discharge electrically. Optical emission spectroscopy is non-invasive and is routinely implemented in both low and atmospheric pressure plasma tools, but spectroscopy systems are relatively expensive and require direct access to the plasma active volume. For these reasons, passive acoustic diagnostics represent a far more favorable alternative to the foregoing diagnostic methodologies as they are low cost, truly non-invasive and can be performed in real time without plasma tool modification or down time [108].

Acoustic emissions are known to have been produced by electrically modulated gaseous discharges since the late nineteenth century [109]. The periodic addition of energy into the discharge produces acoustic waves associated with both the charged [12, 110] and neutral [111, 112] components of the discharge.

Reciprocal to these effects is the influence the plasma components have on the passage of an acoustic wave through the plasma bulk. Theoretical and experimental works have shown that acoustic dispersion can result in amplification [112–114], increased velocity [115], attenuation [116] and reflection [117] of acoustic waves depending on the wave frequency.

The majority of works concerning acoustics in atmospheric pressure plasmas have focussed on the interaction between acoustic waves and the plasma (active techniques) and the resulting effects on the plasma state/chemistry

[118–121].

Although, recently, acoustic diagnostics have been applied to atmospheric pressure plasma systems, the analysis of the plasma acoustic emissions has solely been confined to the frequency domain through the use of the Fourier transform [122]. However the Fourier transform is not suited to the analysis of highly transient signals [123], such as those usually found in pulse powered plasma jets [50, 57–60, 62–64, 107]. A more appropriate tool for inspecting signals which contain transients is the wavelet transform as it offers multi-resolution in the time and frequency domains simultaneously [123, 124].

Therefore, in this chapter, the plasma produced acoustic signals are analysed and compared, within an APLFJ system, with flowing helium, in the time, frequency and time-frequency domains. This work includes the novel implementation of the wavelet transform in the analysis of the plasma jet acoustic emissions.

6.2 Acoustic signal processing techniques

6.2.1 Fourier Transform and Short Term Fourier Transform

To extract frequency information from a time domain signal, the Fourier transform is commonly used. The Fourier transform, $F(\omega)$, of a time domain signal is defined as [125]

$$F(\omega) = \frac{1}{\sqrt{2\pi}} \int_{-\infty}^{\infty} f(t) e^{-j\omega t} dt \tag{6.1}$$

where $\omega = 2\pi f$ and f is the frequency of the signal. The application of the fourier transform involves convolution of a complex exponential with the time domain signal to return a set of weighted coefficients, at each frequency, which are used to represent the frequency content of the signal.

It is clear from the definition of the Fourier transform that no temporal resolution of the signal is possible as the integral is evaluated from -∞ to ∞ over the whole time domain signal. Obviously, this is not preferable when the extraction of the frequency content of transients in the signal are involved.

An extension of the Fourier transform to the *time-frequency* domain is the short term Fourier transform (STFT) [126], which is defined by

$$F(\tau, \omega) = \int_{-\infty}^{\infty} f(t) w(t-\tau) e^{-j\omega t} dt \tag{6.2}$$

The function, $w(t-\tau)$, is a windowing function (usually, although not exclusively Gaussian) which may be shifted along the signal in the time domain. Through this shifting, the frequency content of the windowed time domain signal may be evaluated through computation of the Fourier transform (equation 6.1) of the windowed signal at each successive value of τ. An example of a windowed cosine ($f = 3Hz$) function, which may be thought of as the real part of the convolution, is shown in figure 6.1. The general equation of a Gaussian windowing function is

$$w(t-\tau) = ae^{-(t-\tau)^2/2\sigma^2} \tag{6.3}$$

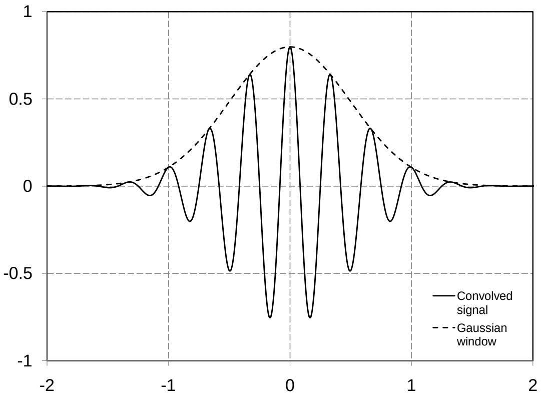

Figure 6.1: *Short Term Fourier Transform windowing function example*

With reference to figure 6.1, the constants in equation 6.3 are $a = \frac{1}{\sigma\sqrt{2\pi}}$, $\tau = 0$ and $\sigma = 0.5$.

A limitation of using the STFT is that only a single resolution of the convolution is used. A large value of σ implies a large window area and hence poor temporal resolution of most higher frequency components, whereas a narrow window will improve temporal resolution but lead to the loss of lower frequency components [124]. This is analogous to the Heisenberg uncertainty principle in quantum mechanics, where momentum and position are analogous to time and frequency . For this reason the multiresolution Wavelet Transform was developed.

6.2.2 The Wavelet Transform

In the previous section it was shown that the choice of a single windowing function in the STFT limited the resolution capabilities of the transform. The features of this resolution limitation are large windows lead to poor temporal resolution whilst narrow windows lead to poor frequency resolution. The wavelet transform overcomes this by providing multiresolution. This multiresolution is invoked through scaling the frequency *together* with the width of the windowing function. This procedure is carried out by introducing the concept of a *wavelet*.

The general definition of a wavelet, which may be real or complex, is [123]

$$\Psi_{a,\tau}(t) = \frac{1}{\sqrt{a}}\Psi\left(\frac{t-\tau}{a}\right) \tag{6.4}$$

Here it can be seen that the wavelet is a function of τ and a parameter a known as the *scaling parameter*. The wavelet transform (WT) is then defined as

$$WT_f(a,\tau) = \frac{1}{\sqrt{a}}\int_{-\infty}^{\infty} f(t)\Psi^*\left(\frac{t-\tau}{a}\right)dt \tag{6.5}$$

In equation 6.5 the constant outside of the integral is a normalisation constant. The difference between the WT and STFT is best illustrated by an example. The example used here, the *Morlet* wavelet, is the transforming wavelet which is used in these experiments. It is given by

$$\Psi(a,\tau) = \frac{1}{\pi^{\frac{1}{4}}}e^{-\frac{1}{2}[(t-\tau)^2/a^2]}e^{i\omega_0(t-\tau)/a} \tag{6.6}$$

and the corresponding transform by [124]

$$WT(a,\tau) = \int_{-\infty}^{\infty} x(t)\frac{1}{\pi^{\frac{1}{4}}}e^{-\frac{1}{2}[(t-\tau)^2/a^2]}e^{-i\omega_0 (t-\tau)/a}dt \tag{6.7}$$

Comparing the convolution function of equation 6.7 with that of the convolution function of equation 6.2 we can see that as a a is varied in 6.7, both the width of the window and the internal frequency, $\omega = {}^{\omega_0}/_{a}$, change in 6.7 whilst the window is fixed and ω is varied in 6.2. This is illustrated for various values of a in figure 6.2 (note that the frequency and scale are inversely related). It is through this property of the convolution function that multiresolution is achieved. The multiresolution is intuitive given that as the window is enlarged, the frequency is reduced i.e. the convolution is performed over a larger portion of the time domain signal in order to convolve low frequency signals. Whilst the converse is necessary for high frequency transients. In the experimental work considered here, both the Fourier Transform and (Morlet) Wavelet Transform were used to analyse the acoustic signals in the frequency

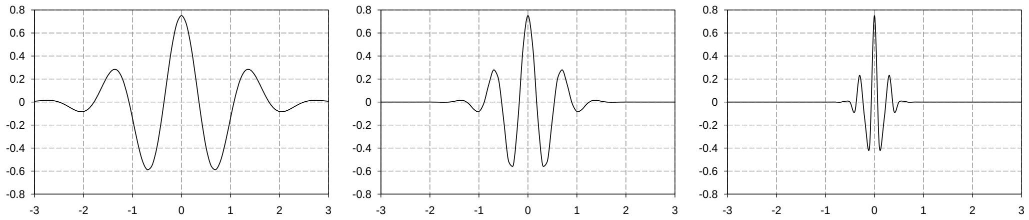

(a) a = 1 **(b)** a = 0.5 **(c)** a = 0.2

Figure 6.2: *Effect of varying the scaling parameter, a, on the Morlet convolution function (a) a = 1 (b) a = 0.5 (c) a = 0.2*

and time-frequency domains. The Morlet Transform was chosen as it provides the best time-frequency resolution properties for acoustic signals [124].

6.3 Atmospheric pressure linear field jet (APLFJ) diagnostics

The diagnostics were carried out on the APLFJ described in chapter 3, section 3.3. Here the square wave modulation feature was not used to exclude the analysis of highly complex acoustic and electrical waveforms. The resonant primary drive circuit was configured to operate at a fixed frequency of approximately 3.6 kHz. The diagnostic set-up is detailed in figure 6.3.

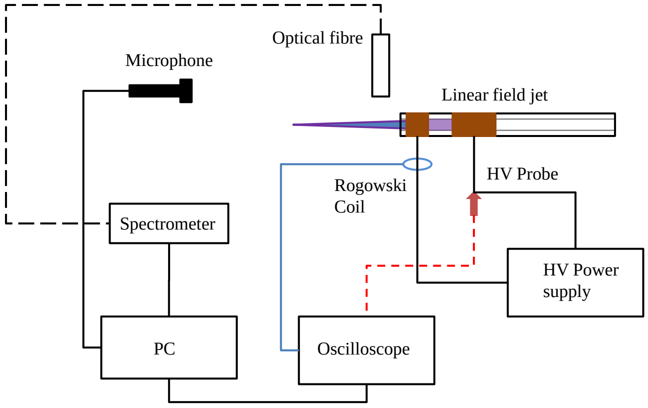

Figure 6.3: *Schematic of the experimental setup. The microphone and optical fiber were placed parallel to the the discharge axis setup*

The applied voltage was measured by means of a high voltage probe whilst the total discharge current was measured using a Bergoz CT-B1.0 current transformer (500 MHz, 0.7 ns rise time, 1V/A). The current and voltage signals were transferred to an oscilloscope (Tektronix 3034B, 500 MHz and 3 GSs^{-1}), coupled through a GPIB interface, to a data acquisition PC to analyse and process the signals in real time.

A 200 μm, 1.5 m length optical fiber was mounted perpendicularly to the plume axis at a distance of 5 mm from the termination of the tube. Optical emission spectra were taken at an integration time of 200 ms using a Ocean Optics HR4000 USB spectrometer.

A Yoga EM-01 microphone (frequency response 20 - 22 kHz) was mounted 100 mm downstream of the plasma plume and off the plume axis to avoid disturbing the gas flow and capture the spherical acoustic pulses generated by the discharge at the tube opening [127]. The acoustic signals were captured continuously at a sampling rate of 96 kS/s and analyzed in the time, frequency and time-frequency domains using a virtual instrument based on the NI LabVIEW Advanced Signal Processing Toolkit. The signal processing of the acoustic emissions was performed in quasi real time owing to the computational expense of the wavelet transform algorithm, whilst the electrical signals were monitored in real time. The results of the wavelet convolution are represented graphically on an intensity map known as the *wavelet scalogram.*

In time-frequency analyses, the wavelet transformations were carried out using 800 frequency scales and 500 time translations on the acoustic signals.

6.4 Results and discussion

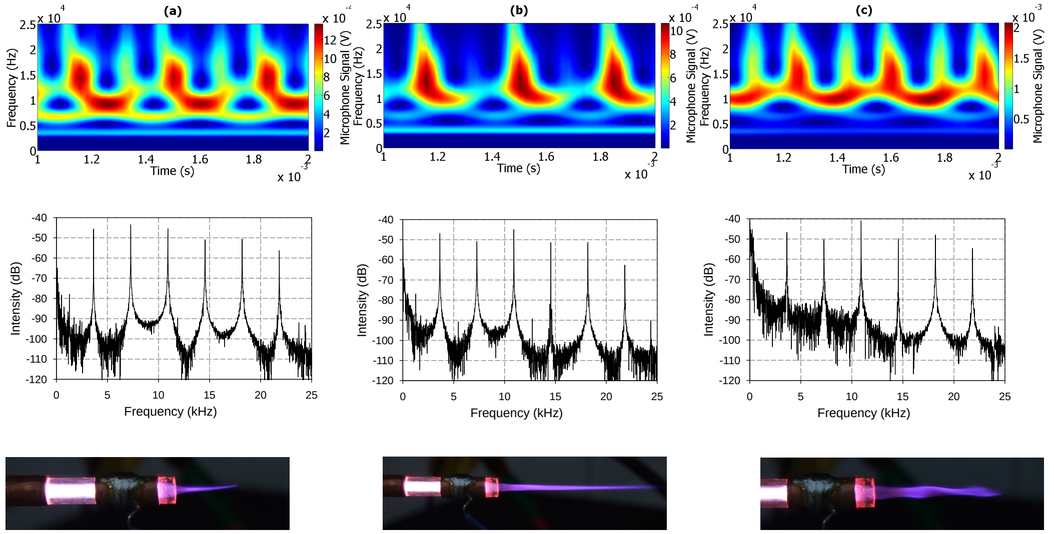

Figure 6.4: *Wavelet scalograms, Fast Fourier Transforms and images of (a) Buoyant plasma plume (Q=0.5 lpm, Re=45,* $Ri = 1.7 \times 10^{-2}$*) (b) Laminar and transitional plume(Q=3 lpm, Re=271,* $Ri = 4.1 \times 10^{-4}$*) and (c) Turbulent plume (Q=7 lpm Re=633* $Ri = 9.1 \times 10^{-5}$*)*

6.4.1 Acoustic emission scalograms

As shown in [57, 59, 64], one of the principle methods to increase the length of the plasma plume is to increase the gas flow rate into the plasma jet device. However, beyond a certain flow rate and hence gas exit velocity, the plasma undergoes a transition from a laminar to turbulent regime, resulting in a

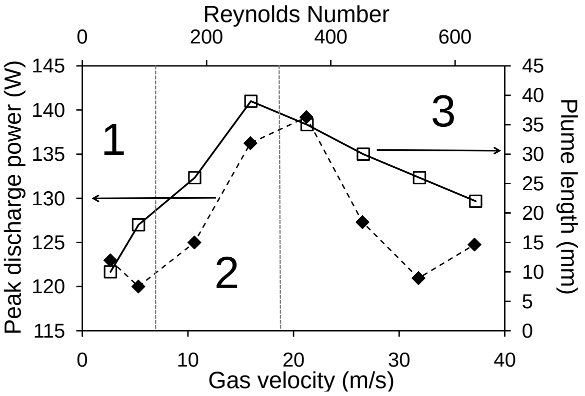

Figure 6.5: *Variation in the peak dissipated power and plume length extension with respect to gas exit velocity and pipe flow Reynolds number. The figure is divided into (1) Buoyant regime, (2) Laminar-transitional regime and (3) Turbulent regime.*

shortened, nonuniform plume structure [57, 62] (see figures 6.5 and 6.4). To evaluate the effect the changing gas flow rate has on the acoustic signatures the gas flow rate was initially set to 0.5 litres per minute (lpm). The flow rate was then set to 1 lpm and increased to 7 lpm in 1 lpm steps. The applied voltage amplitude was maintained at approximately 5.4 kV throughout.

Three operating modes, associated with the gas flow rate can be identified in the images of figure 6.4. The flow regimes can be separated into those that are buoyancy dominated (figure 6.4 (a)) and the reactive plume follows the helium mole fraction [57], laminar, momentum dominated flow (figure 6.4 (b)) [57], and turbulent flow (figure 6.4 (c)).

Inspection of figure 6.4 reveals that, whilst it is difficult to differentiate between the flow modes of operation of the jet through the Fourier trans-

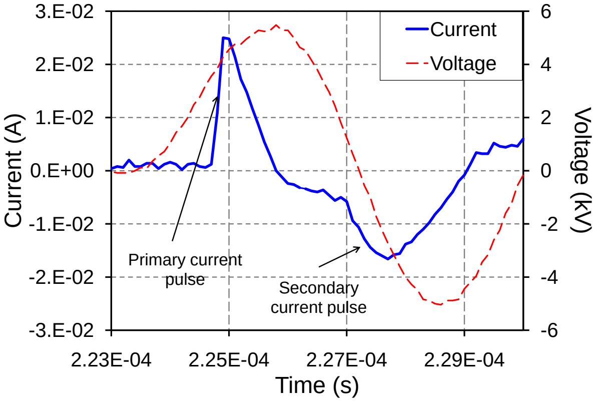

Figure 6.6: *Current voltage characteristics of the APLFJ source. There are two breakdown events - one on the voltage rise (primary current pulse) and one as the voltage changes polarity (secondary current pulse)*

form (with the exception of an increase in the low frequency noise floor in the turbulent mode), each flow mode produces a unique wavelet scalogram. Although, in the figure, three cycles of the scalogram are produced for clarity, the periodicity of the scalograms remained over each 1 second sample interval, with the exception of the turbulent mode (part (c) of figure 6.4), which is discussed later. An example of this periodicity is shown in figure 6.8 where the laminar and turbulent flows are compared (Note how the constant drive frequency presence is disturbed in the turbulent regime).

There is a qualitative correlation between the scalogram structures of figure 6.4 and the electrical signals. There were two breakdown events per cycle , one on the voltage rise and another as the voltage pulse changed polarity (see figure 6.6). The amplitude of the second current peak did not change

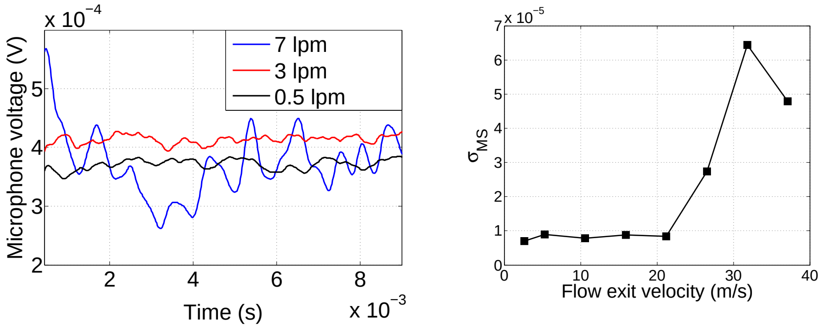

Figure 6.7: *Time frequency analysis of the first harmonic of the acoustic emission from the APLFJ. As the jet undergoes a transition from the laminar to fully turbulent regime the first harmonic amplitude becomes heavily modulated by low frequency disturbances. The standard deviation of the modulation,* σ_{MS}*, around the mean value of the time baserd harmonic amplitude is minimized until this point*

significantly in each mode and was approximately equal to 16 mA. Each successive breakdown is characterized by a strong broadband acoustic emission in the wavelet scalogram which is associated with the instantaneous delivery of energy into the discharge followed by the rapid expansion of the gas. In the buoyant mode, the peak current (~ 20 mA) through the discharge during the first breakdown event is less than that for the laminar-transitional regime (~ 25 mA) and hence the second breakdown event does not appear so strong in the broadband acoustic emission of the second pulse in the laminar regime. When the flow becomes turbulent, again the primary current pulse is decreased (~ 19.5 mA) and the broadband acoustic emission of the second pulse shows significant presence in the scalogram once more (Note: the scalo-

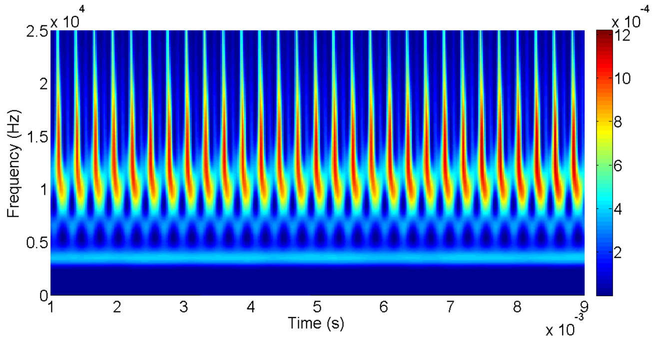

(a) Laminar flow wavelet

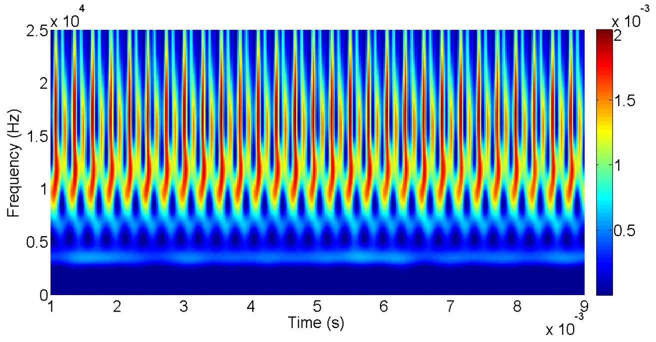

(b) Turbulent flow wavelet

Figure 6.8: *Comparison between long term periodicities in (a) Laminar flow and (b) Turbulent flow acoustic wavelet transforms*

grams are not phase matched to each other and the most intense broadband acoustic emission is that of the primary current pulse for each mode).

These flow regimes have been shown to be weakly dependent on the flow Reynolds number, Re, and more strongly dependent on the flow Richardson number,Ri[128–131]. the respective Re and Ri for each of the regimes are included in figure 6.4. The Richardson number may be defined by [132]

$$Ri_1 = \frac{gd(\rho_\infty - \rho_0)}{\rho_0 U^2} \tag{6.8}$$

where ρ_∞, ρ_0, d, g, U denote the density of the surrounding air, the density of helium, the hydraulic (inner) diameter of the tube, the acceleration due to gravity and the mean velocity of the gas respectively. The Reynolds number, *Re*, is given by [128, 132]

$$Re = \frac{Ud}{\nu} \tag{6.9}$$

where ν is the kinematic viscosity of helium , 1.17×10^{-4} m^{2}s^{-1} [132]. The gas velocity was determined using $U = 4Q/\pi d^2$, where Q is the volumetric flow rate. The jet Strouhal number, which is elated to the frequency of self excited oscillations of the jet, is given by [132]

$$St = \frac{fd}{U} \tag{6.10}$$

In equation 6.10 f is the frequency of self excited oscillations of the exiting plume. The values for *Re* and *Ri* for each of the flow modes are included in figure 6.4. In reference [129] a modified Richardson number, Ri_1, for helium jets expanding into ambient air, was defined by replacing ρ_0 with ρ_∞ in the denominator of equation 6.8. An expression was then found between Ri_1 and St given by $St = 0.8Ri_1^{0.38}$ for $Ri_1 < 100$. Further inspection of the wavelet scalograms reveal that as the plume undergoes the transition into the fully turbulent regime low frequency oscillation bursts (c. 180 Hz) are present for time spans of some milliseconds (see figure 6.9). Using the expression in equation 6.10 to determine the predicted frequency of oscillation of the plume from the above relation for Ri_1 gives a value of 200 Hz for an Ri_1 value of 1.21×10^{-5}. This value correlates well with the value observed within the scalogram. Also noteworthy, is that these oscillations were not present over the whole data collection interval and so did not appear as a well defined peak within the Fourier transform.

As the APLFJ undergoes the transition into the fully turbulent mode it was noticed that the first harmonic of the acoustic signal becomes more heavily modulated by low frequency oscillations. These oscillations are related to the appearance of the low frequency signal described above. A time history of the amplitude of the first harmonic is shown in the left of figure 6.7 for the three modes outlined above. The figure to the right of figure 6.7 shows calculations for the standard deviation of the amplitude of the first harmonic around its mean value, σ_{MS} for all of the flow rates inspected. It is clear from this figure that the turbulent transition, at which the plume length and dissipated power are reduced, can be identified through measurement of σ_{MS} of the first harmonic which shows a steep rise above a gas exit velocity of 20 ms^{-1}.

6.4.2 Anomalous spark detection

Anomalous sparking or arcing of the plasma jet can lead to local overheating and substrate or tissue damage [2, 133]. A spark event leads to a rapid overheating and expansion of the surrounding gas which can be modeled as

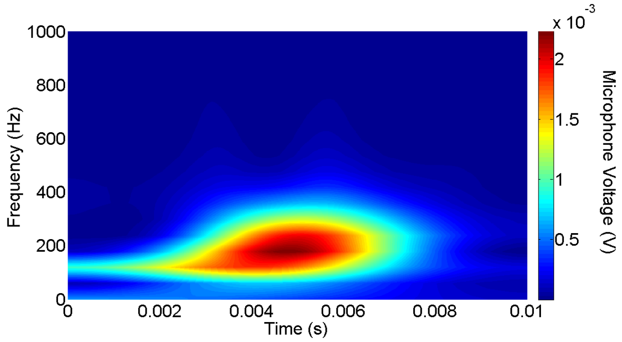

Figure 6.9: *Zoom on the low frequency content of the wavelet scalogram whilst the flow is turbulent over a period of 10 ms. There are bursts of low frequency oscillations around 180 Hz which persist for 7 ms.*

a delta like pressure pulse. The Fourier transform of an ideal delta pulse is equal to unity, therefore all frequencies are present at the same magnitude in such signals. Indeed it is this feature of spark gaps that are invoked in determining the frequency response of acoustic transducers [127].

In figure 6.10 a discrete acoustic event was captured during the foregoing experiments characterized by an intense signal, the magnitude of which was approximately an order of magnitude greater than previous acoustic signals and whose magnitude was approximately even across the entire frequency content of the scalogram. This was not detected by either the electrical or optical diagnostics. Given the content of the acoustic signal it was most likely the detection of an anomalous spark which may have occurred across the two outer electrodes or within the discharge bulk.

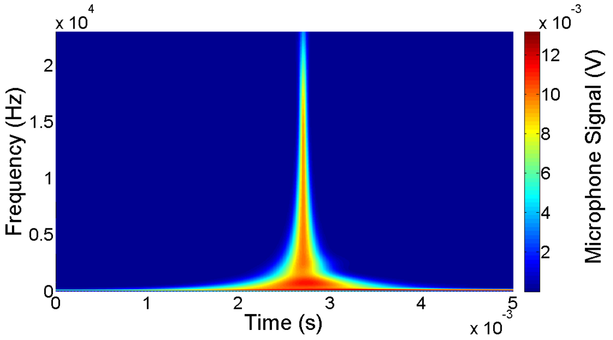

Figure 6.10: *Wavelet scalogram capturing an anomalous sparking event whilst the plume was in operation*

6.4.3 Remote power measurements

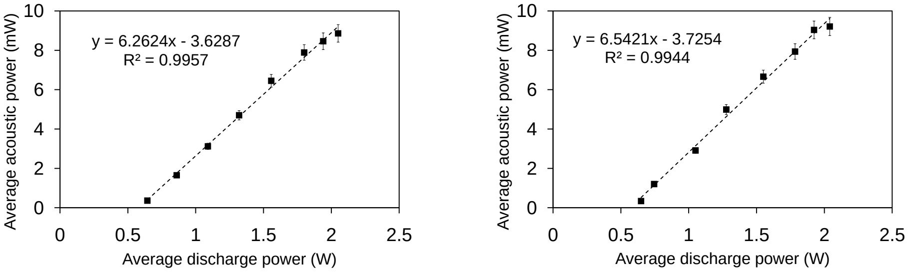

Figure 6.11: *Remote average discharge power measurement using passive acoustic sensing at gas flow rates of 4 lpm (left) and 2 lpm (right).*

In this section the results of measurements of the average acoustic power sensed by the microphone are compared to the average power dissipated in the discharge over a number of cycles, n. The average acoustic power sensed by the microphone, $\bar{P}_{acoustic}$, and the average power dissipated in the discharge,

$\bar{P}_{discharge}$ may be found using equations 6.11 and 6.12 respectively.

$$\bar{P}_{acoustic} = \frac{1}{nT}\int_{t}^{t+nT}\frac{V_A(t)^2}{Z}dt \tag{6.11}$$

$$\bar{P}_{discharge} = \frac{1}{nT}\int_{t}^{t+nT}V_D(t)I_D(t)dt \tag{6.12}$$

In equations 6.11 and 6.12, $V_A(t)$ and $V_D(t)$ are the voltages measured with the microphone and high voltage probe respectively, Z is the impedance of the microphone and sound card (1 kΩ), $I_D(t)$ is the discharge current and T is the pulse repetition period. The applied voltage to the discharge was increased from 3.5 kV to 7 kV in 0.5 kV steps. Each electrical and acoustic power measurement was performed through averaging over n=30 cycles of the electrical and acoustic waveforms. The results of these measurements are presented for two different gas flow rates of 4 lpm (left) and 2 lpm (right) in figure 6.11.

It can be seen that for both flow rates there is a very similar linear relationship between the average power dissipated in the discharge and the average acoustic output power. The slopes and intercepts of the linear relationship between the two operating modes are approximately equal. These results imply that for a given distance of the microphone placement from the discharge a non invasive measurement of the discharge power can be performed through the acoustic sensing whilst the discharge is operating in the laminar mode with a constant of proportionality approximately equal to $1/(6.4\times10^{-3})$. This however was not the case for the turbulent mode as a significant amount of the acoustic power is represented by the pressure oscillations due to the turbulent break up of the gas jet and hence the measurement is not solely due to the discharge acoustic emissions.

These results are not surprising as they may be interpreted using the theory of Morse and Ingard [110] for acoustic wave generation by a gas discharge. In their work it was proposed that the sound pressure wave, p, produced by plasma is related to the source term by [110]

$$\frac{1}{c^2}\frac{\partial^2 p}{\partial t^2} - \nabla^2 p = \frac{\gamma - 1}{c^2} e \frac{\partial}{\partial t}(N_e b_e E^2) \tag{6.13}$$

In equation 6.13, c, is the wave velocity, γ, the ratio of the specific heats, e, the electronic charge, N_e, the electron density, b_e, the electron mobility and E the electric field. As the power is coupled into the discharge both the electric field and density increase proportionately and hence so does the acoustic wave amplitude, therefore we expect the average powers to be proportional to each other as long as the other contributions to the acoustic output from the jet are relatively unimportant. Given that the noise output due to the jet turbulence is of the same order as that from the power coupled into the discharge this contributes to the acoustic power also and hence the method does not work for turbulent jets.

6.4.4 Optical emission spectroscopy

The analysis of the optical emission spectra consisted of monitoring the N_2 emission at 337.1 nm, the N_2^+ line at 391.4 nm, the 706.5 nm helium emission line and the hydroxyl radical, OH, emission at around 309 nm. The results of the variation of these emission lines with respect to increasing gas velocity are presented to the left of figure 6.12.

The emissions from the 706.5 nm and 391.4 nm lines monotonically increase with gas exit velocity until the flow becomes fully turbulent and a plateau is reched whilst the 337.1 nm line decreases as the gas velocity increases. More interestingly is the development of the emission from the 309 nm emission line. Initially the intensity drops with increasing gas exit velocity but begins to increase again as the gas velocity increases from 10 ms^{-1} to 15 ms^{-1}. This could be either attributed to an increase in the electron temperature due to excess helium in the discharge (the first excitation energy of helium ~ 20 eV) or as a result of water vapour being dislodged from the gas line walls as the gas velocity within the discharge gas feed lines increases.

The increased presence of the emission from the 391.4 nm is due to the Penning ionization reaction ($He^* + N_2 \rightarrow He + N_2^+ + e$)[86] and is indicative of the increase in the metastable helium density as the fraction of air in the gas stream is reduced. This is verified by comparison between the ratio of the emission from the 337 nm line to the 391.4 nm line in the right of figure 6.12 which shows an approximately linear dependence on the gas exit velocity indi-

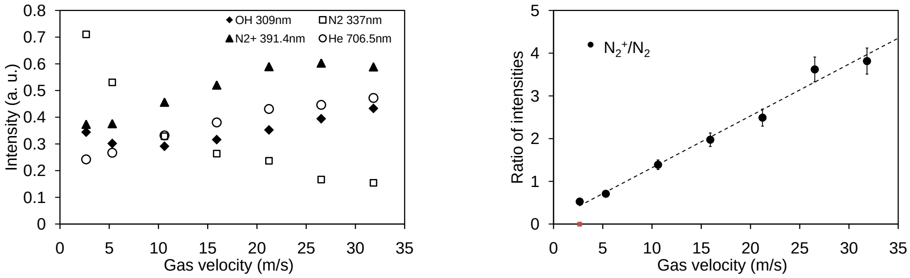

Figure 6.12: *Bulk OES measurements (left) at a point 8 mm downstream of the exit of the glass tube and ratio of the emissions from the molecular nitrogen ion, N_2^+, at 391.4 nm to the molecular nitrogen emission, N_2, at 337.1 nm (right)*

cating a more efficient metastable production from the surrounding nitrogen impurities.

6.5 Conclusions

We have presented the implementation and analysis of passive acoustic diagnostics in an atmospheric pressure linear field jet system operating in flowing helium. Three flow modes were identified through images taken of the plume whilst in operation *viz.* a buoyant mode, a laminar-transitional mode and a turbulent mode. The maximum power coupling into the discharge from the power supply correlated with the maximum extension of the plasma jet plume.

It was found that differentiating the three modes, acoustically, in the frequency domain, through the use of the Fourier transform was relatively difficult. However, analysis of the acoustic emissions in the time-frequency domain through the use of the wavelet transform showed that each flow mode produced an easily distinguishable, unique scalogram. Each unique scalogram qualitatively represented the electrical characteristics of the distinct breakdown events in the corresponding plasma mode.

Further inspection of the low frequency content of the wavelet scalograms revealed that low frequency oscillation bursts of c. 180 Hz frequencies were present over periods of some milliseconds. These oscillations correlated well with the frequency dependence on the flow Richardson number proposed in reference [129]. Alternatively, we have shown that the transition into the fully turbulent regime of operation of the jet can be identified by taking the standard deviation of the mean of the modulation of the first harmonic of the acoustic signal in the time-frequency domain. It was further revealed that anomalous sparking either between the discharge electrodes or within the plasma bulk could be detected through analysis of the wavelet scalograms also.

Comparisons between the average discharge power and the average acoustic power output from the jet whilst in the laminar flow regime showed a linear correlation for a set microphone location distance from the discharge exit orifice for two gas flow rates. These results correlate well with the theory of Morse and Ingard for the acoustic pressure wave generated by gas discharge. The reason for no such correlation existing whilst the jet becomes turbulent has been attributed to the increased flow induced noise contribution by the jet.

Finally, the optical emission spectra shows emission from both the 706.5 nm line and the 391.4 nm line increase monotonically until the jet becomes fully turbulent whilst the reciprocal happens to the 337.1 nm line. Monitoring of the emission from the hydroxyl radical at 309 nm reveals that the emission goes through an inflection at a gas velocity of 10 ms^{-1} which may be attributed to either condensation being freed from the inner walls of the tube or an increase in electron temperature due to the increase in the mole fraction of helium in the discharge.

These results show that passive acoustic diagnostics, together with the novel application of multi-resolution analysis, can be effectively used as a low cost diagnostic in long term, real time monitoring of plasma jet discharges across a variety of power and gas flow ranges.

CHAPTER 7

Atmospheric plasma surface functionlisation for biosensor applications

7.1 Introduction

The relatively new field of lab-on-chip biomedical and environmental diagnostics offers a lower cost, quicker and highly reliable alternative to current chemical and biological diagnostic techniques used in bioassays and environmental pollution detection. Typical devices generally use surface modified plastics together with fluorescent transduction to sample small amounts of biocompounds such as proteins or disease related biomarkers [134–136]. The current state of the art in lab-on-chip or point-of-care biomedical diagnostics is to reduce cost and enhance the analytical performance through the utilisation of cheap, disposable polymer substrates, reduction of non-specific binding [137, 138] and refinement/enhancement of fluorescent sampling methodologies [136, 139].

Bioimaging techniques predominantly involve broadband excitation of wavelength specific biomolecular structures, *fluorophores*. Each molecular fluorophore is characterised by its absorption spectrum which depends on the particular state the molecule (or molecular fragment) is in, i.e. it is sensitive to changes in molecular dipole moment etc.[140]. Thus the fluorescence spectrum is influenced by the molecular state and the spectrum not only facilitates molecular identification but can also be used to study time resolved kinetics of the molecular specie [140].

However, such fluorescent signals in low concentrations may be extremely weak. Localised surface plasmon resonance (SPR) at an attached metal nanoparticle (NP) molecule interface leads to the phenomenon of plasmonic enhancement that can result in a multiple fold enhancement of the signal obtained from fluorescence based biosensors chips. Since the excitation enhancement is proportional to the square of the amplitude of the electric field [140, 141] a maximum enhancement is achieved if the metallic nanoparticle plasmon resonance wavelength coincides with the fluorophore absorption band. The plasmon resonance band depends on the size, shape and distribution of metal nanoparticles on the surface [141].

Reduction of non-specific binding of proteins to polymers in bioassays is a key challenge [138, 142]. Long chain polyehtylene glycol (PEG) is known to be an efficient protein repellent [137, 138]. Therefore the incorporation of PEG functionality into a biosensor facilitates control of protein adherence to the sensor. However, the deposition of long chain PEG molecules cannot be realised in low pressure plasma tools due to its high vapour pressure and the large heating which would be required to vapourise the liquid.

Both the signal amplification and reduction in non specific binding in bioassays remain key goals in the field of biosensors. The current state of the art in both functionalisations requires either wet chemical means [138, 139] or, when aerosols are used, high temperatures [143], both of which are time consuming. This chapter seeks to address these two problems by providing a novel and efficient solution to the functionalisation of disposable plastics through aerosol assisted cold atmospheric pressure plasma deposition using a linear field jet.

7.2 Experimental setup

The experimental setup is detailed in figure 7.1 and uses the linear field jet configuration and power supply described in chapter 3. The depositions were performed using 40 nm and 80 nm spherical gold nanoparticle colloids and a PEG1000 solution (Sigma Aldrich). Both mechanical and ultrasonic nebulisation methods were used to inject aerosols into the plasma jet depending on the surface modification being performed. The reasons for using two nebulisation methods shall be discussed in the results section.

MFC1 served as the primary plasma producing gas flow whilst MFC2 was used to introduce small volumes of aerosol into the plasma volume. Throughout, helium gas was used as both the primary and secondary flow gases. In the case of ultrasonic nebulisation, the secondary gas was allowed to flow through the aerosol mist and into the primary flow once all of the colloid was nebulised in the conical flask. The volume density of aerosols introduced into the plasma volume may be determined from the two gas flow rates and the initial quantity of colloid in the conical flask together with the flask volume. For all of the experiments involving nanoparticle deposition, the initial volume of colloid was 2 mL.

The gold nanoparticles were deposited on to mercapto silane coated Zeonor® and silicon substrates whereas the PEG solution was deposited on Zeonor® [144], both of which were initially placed 1 cm downstream of the plasma plume. Zeonor® is used as it has excellent optical properties which are particularly suited to low cost biosensors whilst silicon was used in order to achieve good images under inspection in the scanning electron microscope. The mercapto silane coating, which was deposited on the substrates using low pressure PECVD, acts as a binding layer for the gold NP.

As in chapter 6, the electrical diagnostics consisted of a high voltage probe on the driven electrode together with a Rogowski coil on the ground path to measure the power coupling through a real time LabVIEW virtual instrument.

It was found that operation of the discharge was extremely sensitive to variations in the applied voltage when aerosols were introduced into the plasma

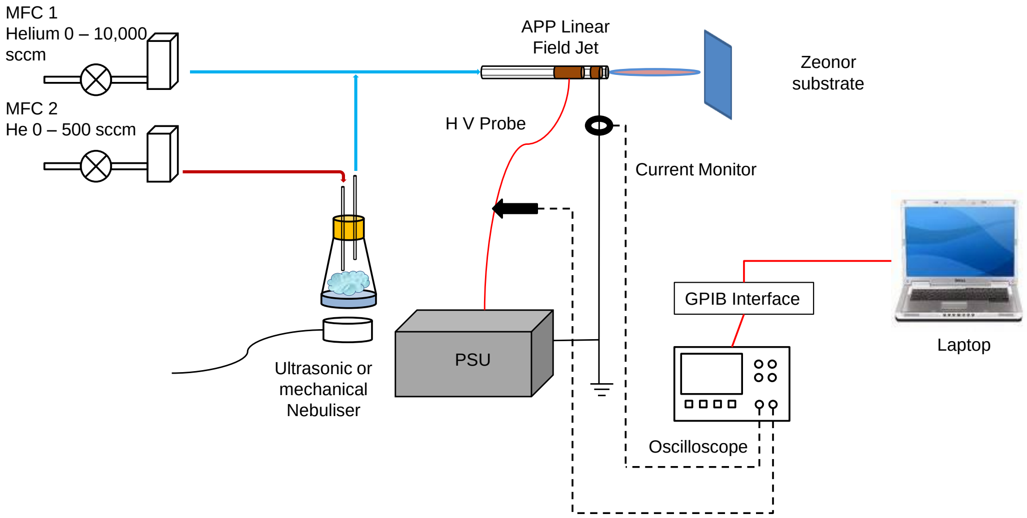

Figure 7.1: *Deposition experimental set up. The apparatus is as described in chapter 3. The substrates were placed on the x-y stage 1 cm downstream of the plasma plume.*

volume. In the case where a low voltage (or voltage modulation) was used, the plasma periodically extinguished or did not strike at all. If the voltage was raised above a certain value then spark formation occurred. Therefore, in order to maintain similar discharge conditions across each of the depositions, a common value for each was found to be a drive voltage of 8 kV pk-pk, with full modulation, corresponding to a power input density of approximately 23 Wcm^{-3}, which was determined by evaluating the power coupled into the discharge volume.

The surface treatment outcomes were examined using scanning electron

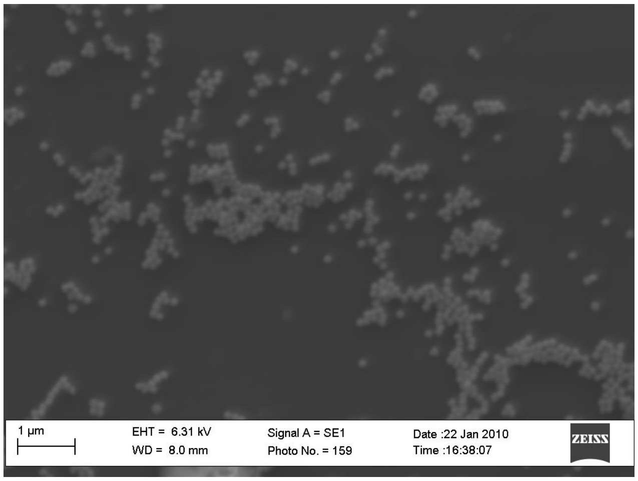

Figure 7.2: *SEM image of non-monodisperse deposition of 80 nm gold nanoparticles on a mercapto silane coated silicon substrate.*

and atomic force microscopy (SEM and AFM), UV-Vis absorption spectroscopy and, in the case of the PEG functionality, through a fluorescent dye technique.

7.3 Results and discussion

7.3.1 Tailoring NP plasmonic enhancement

Initially, the mechanical nebuliser was used to introduce 80 nm nanoparticle colloid aerosols into the plasma jet flow. Whilst adhesion to the substrate did occur, the nanoparticles were found to be arranged in localised aggreagated units around the substrate (see figure 7.2). Testing of the absorption due to plasmonic effects resulted in no absorption peak occurring in this particular

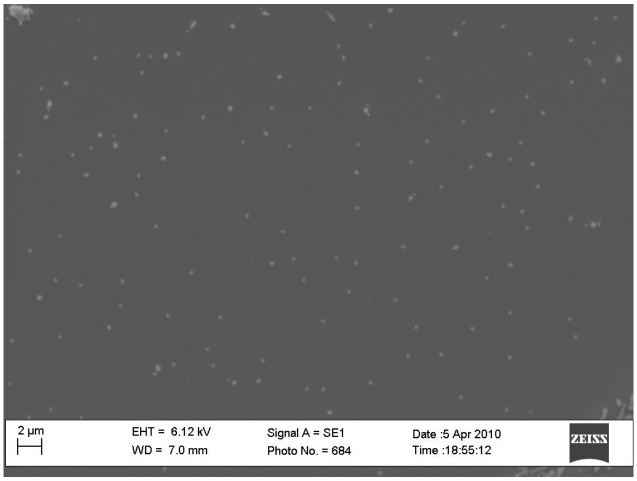

Figure 7.3: *SEM image of monodisperse deposition of 80 nm gold nanoparticles on a mercapto silane coated silicon substrate.*

surface outcome and no change could be observed through variation of the other process parameters.

Using the ultrasonic nebulisation system however, it was found that monodisperse NP coatings could be achieved as shown in figure 7.3. However, under these conditions, the packing density was quite low.

Whilst maintaining the secondary flow into the nebulisation system, the primary jet flow was varied from 5 lpm down to 3lpm (these values correspond to when a continuous, laminar discharge could be maintained) and the packing density shown in figure 7.4 resulted. Depositions were then performed using the 40 nm gold colloid under the same conditions. The results of the UV-VIS absorption spectra for both of these depositions are shown in the left of figure

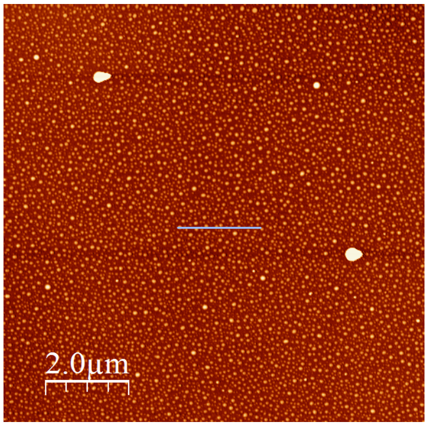

Figure 7.4: *AFM image of monodisperse deposition of 80 nm gold nanoparticles on Zeonor® substrate. Here it can be seen that the density has been much increased*

7.5. Here it can clearly be seen that the plasmonic enhancement absorption has been shifted lower in the wavelength range by approximately 40 nm when 40 nm gold nanoparticles were deposited with comparable areal density to those of the 80 nm particles.

To the right in figure 7.5 is a graph of two absorption spectra taken from mercapto coated Zeonor® deposited 40 nm gold nanoparticles of two different areal densities (N.B. an exact figure was not measured but was found by visual inspection c.f. figures 7.3 and 7.4. The graphs show that the plasmonic band had shifted by approximately 15 nm as the density of packing increased.

These results can be interpreted using the Mie theory for the extinction, $E(\lambda)$, i.e. sum of the light aborption and scattering due to a nanoparticle in

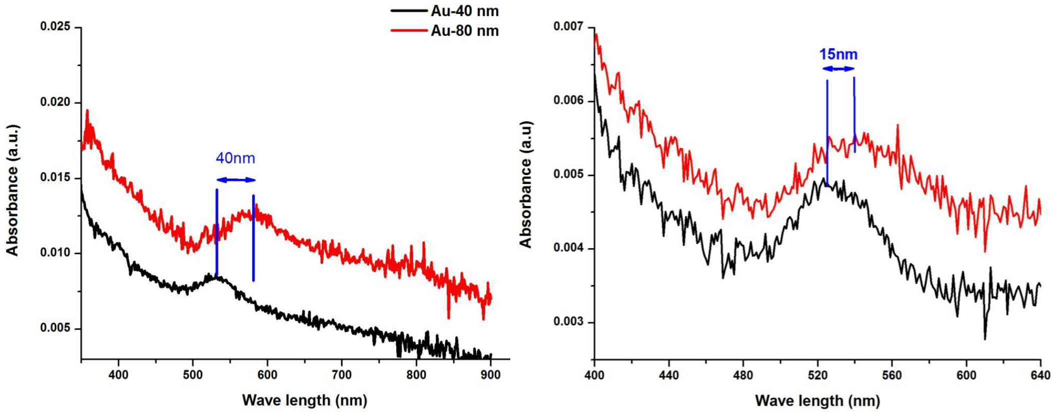

Figure 7.5: *UV-Vis spectroscopic image of (left) 40nm and 80nm gold nanoparticles deposited on to mercapto silane coated Zeonor® (right) 40nm gold nanoparticles with different density of packing. Varying particle size and intermetallic distance results in shift in plasmonic band that can be precisely controlled.*

a dielectric medium is given by [145]

$$E(\lambda) = \frac{24\pi N_A a^3 \epsilon_m^{\frac{3}{2}}}{\lambda ln(10)} \left[\frac{\epsilon_i}{(\epsilon_r + \chi\epsilon_m)^2 + \epsilon_i^2} \right] \tag{7.1}$$

In equation 7.1, N_A is the areal density of particles, a the particle radius, ϵ_m the dielectric constant of the surrounding medium, λ the absorbing wavelength, ϵ_r and ϵ_i the real and imaginary parts of the nanoparticle dielectric function (the real part being negative [146])and χ is a ratio that describes the aspect ratio of the particle (2 for a sphere [145]).

From equation 7.1 it is clear that, for gold nanoparticles, the absorption on a substrate and hence the fluorescent amplification can be tailored by varying both the nanoparticle size and density of packing. The results presented above qualitatively correlate with the Mie theory i.e. as the nanoparticle size is reduced with similar areal density, the plasmon resonance is reduced whilst a decrease in the areal density will decrease the plasmonic enhancement also. In this way fluorescent amplification of specific biomarker flourophores can be tailored on biomedical devices.

7.3.2 Deposition of protein repellent coating

Converse to the deposition requirements of NP on the substrates, in the case of the high molecular weight PEG solution it was found that the ultrasonic nebulisation system was ineffectual in creating a suitable aerosol mist for depositions. Therefore, the mechanical nebulisation system was necessary. Deposition treatments were carried out using the same power and gas flow conditions as used in the case of the nanoparticle depositions.

Here depositions were carried out on specific areas (approximately 2 mm and 3 mm in width) of the Zeonor® slide in order to compare the protein repellent functionality with that of the non-treated portions of the substrate. The homogeneous treatment was produced by moving the x-y stage in the horizontal, x, direction at a constant speed. The different treatment areas were produced by varying the jet to substrate distance thus producing a smaller treatment spot size on the substrate.

To determine the effect of the plasma treatment on the substrate, the

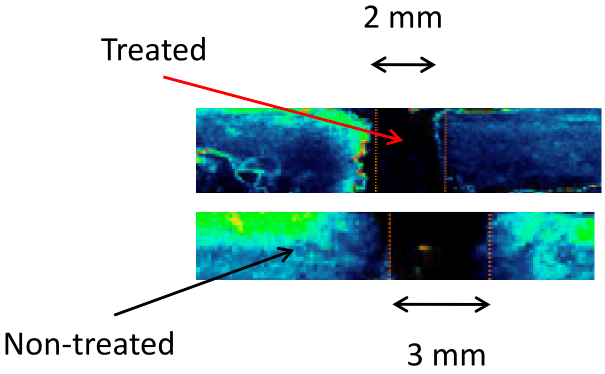

Figure 7.6: *Fluorescence intensity image of Cy5 labeled anti-HCG protein and NIR 664 labelled nanoparticle containing anti HCG protein attached to untreated Zeonor® and PEG1000 coated Zeonor®*

Zeonor® slide was coated with a dye doped protein (Cy5- anti HCG) and a protein containing a dye doped nanoparticle and fluorescence measurements were performed. Figure 7.6 displays images of the substrate fluorescence, whilst figure 7.7 presents the results of the fluorescent intensity measurements. Both clearly shown the site specific protein repelling outcome of the treatments.

This demonstrates that the plasma functionalisation of polyethylene glycol groups can be carried out to much reduce the non specific binding on the substrate.

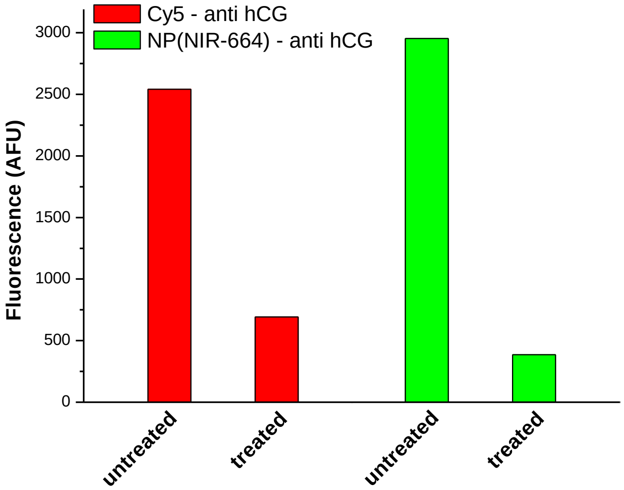

Figure 7.7: *Fluorescence intensity of Cy5 labeled anti-HCG protein and NIR 664 labelled nanoparticle containing anti HCG protein attached to untreated Zeonor® and PEG1000 coated Zeonor®*

7.4 Conclusions

In this chapter the novel application of atmospheric pressure linear field jet plasma treatments to enhance biomedical device functionality has been demonstrated. Through injection of suitable aerosol precursors into the discharge volume and by varying the process parameters, it was found that both plasmonically enhanced and protein repellent disposable plastic surfaces could be produced in a novel and facile way.

In the case of plasmonic enhancement, it has been shown that by varying the gas flow into the discharge volume, and hence the density of aerosols reaching the substrate, that the monodisperse nanoparticle packing density on the device could be tailored to produce wavelength specific plasmonic outcomes. Furthermore it has been demonstrated that, by injecting spherical gold nanoparticles of different diameters, the plasmonic band enhancement could be shifted in the wavelength range also.

Deposition of high molecular weight, long chain organic precursors is not possible using low pressure PECVD as the precursor need to be heated to a significant extent before evaporation. Polyethylene glycol (PEG) is known to be an efficient protein repellent. Through mechanical nebulisation of a long chain form of PEG (PEG1000), into the discharge volume, it has been shown that the protein repellent functionality is retained on the device surface through fluorescence measurements and that by varying the treatment spot size, site specific protein repellent areas could be functionalised onto the biomedical device.

The deposition of site specific protein repellents is not only limited to tailoring biomedical device non-specific binding functionality but could also be used to produce anti-bacterial coatings for other biomedical applications [147].

In conclusion it has been demonstrated that aerosol assisted atmospheric pressure linear field jet treatments can be used as a highly versatile, facile and controllable tool in tailoring disposable plastic surfaces for nano-biophotonic devices.

CHAPTER 8

Conclusions and further work

A set of original diagnostic investigations, on various atmospheric pressure plasma systems, has been performed within the course of work for this thesis. Furthermore, novel polymer surface modifications have been carried out also. The main conclusions and proposals for further developments of this work follows.

8.1 Industrial scale tool diagnostics

Comprehensive electrical and optical diagnostics have been carried out on an industrial scale atmospheric pressure plasma tool. The results of the experiments reveal that the discharge homogeneity and power coupling efficiency are closely coupled to the power supply operating frequency.

Charge-voltage Lissajous measurements reveal that these features are directly influenced by the charge deposition on the electrodes in both helium and helium/oxygen chemistries. The optical diagnostics further demonstrate that the the discharge species emissions and hence the discharge chemistry are effected whereby the discharge emissions scale non-linearly with power, in the inhomogeneous mode, to scaling linearly with power as the discharge becomes spatially homogeneous. The gas temperature measurements, through comparison of the simulated band of the N_2^+ rotational band head at 391.4 nm, show that in the helium discharge chemistry, the gas temperature stays much below the point at which most temperature sensitive plastics may be damaged.

These results are clearly important in identifying process windows in which homogeneous surface treatments are required and in which power ranges these treatments may be performed. Furthermore, the gas temperature measurements are necessary in establishing *a priori* which materials may be treated in the chamber.

The experiments could be extended to include the subsequent effects the varying discharge parameters have on surface treatment outcomes.

8.2 PC based real time diagnostic

The PC based diagnostic methodology presented in chapter 5 has been shown to be instrumental in concisely and economically establishing trends amongst the large experimental datasets resulting from long term characterisations of a laboratory dielectric barrier discharge. A particularly interesting outcome of this work is that the electrical and optical parameters of the discharge evolve over very long timescales which poses questions over how reproducible multi-step (i.e. those that involve various chemistries) processes may be achieved in atmospheric pressure DBDs.

Further applications of the method would include analysis of industrial scale systems, such as that examined in chapter 4 and applying the method to establish correlations between the varying discharge parameters and surface treatments, gas abatement and biomedical applications.

8.3 Acoustic diagnostics

In chapter 6 it has been demonstrated that passive acoustic sensing can be used as a truly non-invasive method for analysing the operation of plasma jets.

The ability to distinguish between different flow mode regimes and to establish the point of maximal power coupling into the jet discharge, through multi resolution signal processing, is particularly useful where access of other diagnostic methods may not be permitted. Similarly, a non-invasive method for power measurement of the jet, through passive acoustic sensing, represents a far more attractive alternative to electrical measurements whereby tool modification or access to the power leads is necessary.

Given that there is a burgeoning drive towards using these systems in the field of plasma medicine, it would be interesting to direct future work towards applying and developing the method to analyse the acoustic emissions due to plasma-tissue and plasma-biofilm interactions as well as interactions of the plasma plume with modified surfaces.

8.4 Biosensor applications

In chapter seven we have demonstrated that aerosol assisted, atmospheric pressure plasma linear field jets may be used to suitably and controllably tailor the surface properties of disposable plastics for biomedical device applications. Future work here would focus on the production of a functioning biosensor incorporating both the surface plasmon resonance and non specific binding capabilities. Moreover scope exists for using PEG depositions to prevent the adherence of bacteria to surfaces after sterilization operations have been carried out on them.

APPENDIX A

List of Publications

A.1 Journal Publications

N O'Connor, V Milosavljevic and S Daniels, 2011. Development of a real time monitor and multivariate method for long term diagnostics of atmospheric dielectric barrier discharges (ADBDs): Application to He, He/N_2 and He/O_2 discharges. *Review of Scientific Instruments*, 82, 083501.

N O'Connor and S Daniels, 2011. Passive acoustic diagnostics of an atmospheric pressure linear field jet including analysis in the time-frequency domain. *Journal of Applied Physics*, 110, p013308.

V J Law, B Twomey, N O Connor, D P Dowling and S Daniels. 2009. Visualization of Atmospheric Pressure Plasma Electrical Parameters. *Topics of*

Chaotic Systems: Selected Papers of Chaos 2008 International Conference., pp204-213.

V. J. Law, V. Milosavljevic, N. O Connor, J. F. Lalor and S. Daniels. 2008. Hand-held Flyback driven coaxial dielectric barrier discharge: development and Characterization. *Review of Scientific Instruments*, 79, 9, pp094707-1-094707-10.

A.2 Conference Proceedings

N O'Connor and S Daniels, Passive and active acoustic diagnostics of atmospheric pressure plasma systems, *37th European Physical Society Conference on Plasma Physics*, 21st - 25th JUNE 2010, Dublin City University, Dublin, Ireland.

N O'Connor, J. F. Lalor, V. Milosavljevic, V. J. Law and S. Daniels, Extraction of Salient Electro-Optical Atmospheric Pressure Plasma (APP) Parameters in Real Time, *Annual Precision Group Meeting*, 30th - NOV 2009, NCPST, Dublin City University.

V J Law, B Twomey, N O'Connor, D P Dowling and S Daniels., Multivariate analysis of an industrial atmospheric pressure glow discharge., *61st An-*

nual Gaseous Electronics Conference, 14-OCT-08 - 17-OCT-08, Dallas, Texas, USA.

V J Law, N O'Connor, and S Daniels, Radio frequency metrology for mobile atmospheric pressure plasma devices, *Progress in Electromagnetic Research Symposium*, 02-JUL-08 - 07-JUL-08, Cambridge, USA, 26 - 30.

V J Law, B Twomey, N O'Connor, D P Dowling and S Daniels , Visualization of Atmospheric Pressure Plasma Electrical Parameters, *In: Christos H Skiadas ed.1st Chaotic Modeling and Simulation International conference (CHAOS 2008).*, 03-JUN-08 - 06-JUN-08, Chania, Crete, Greece, p42.

V J Law, B Twomey, N O'Connor, D P Dowling, W G Graham and S Daniels, Object recognition within Atmospheric pressure plasma, emphIn: Hosted by NCPST, Dublin City University ed. IPBPG Conference 2008, 08-MAY-08 - 09-MAY-08, Dublin City University, Ireland.

N O'Connor, B Twomey, V J Law D P Dowling and S Daniels, Optimisation of an In-line Atmospheric Pressure Plasma Process., *In: Hosted by NCPST, Dublin City University ed.IPBPG Conference 2008*, 08-MAY-08 - 09-MAY-08, Dublin City Universty, Ireland.

N O'Connor, B Twomey, D Dowling, S Daniels and V J Law, Current pulse width modulation spectroscopy as an atmospheric pressure plasma diagnostic technique., *In: poster 29 ed.Technological Plasma Workshop*, 18-DEC-07 - 19-DEC-07, Belfast, UK, p53.

V J Law, N O'Connor, J F Lalor and S Daniels, Development of the Flyback coaxial dielectric barrier discharge, *Technological Plasma Workshop*, 18-DEC-07 - 19-DEC-07, Belfast, UK, 45.

A.3 Other Presentations

N O'Connor, Parameter monitoring and electron density measurement in atmospheric pressure plasma in real time, *NCPST Seminar*, 15-SEPT-2009.

N O'Connor, Real time passive diagnostics for atmospheric pressure plasma processing tools, *University College Dublin Seminar*, 7-AUG-2009.

N O'Connor, Optimisation of an in-line atmospheric pressure plasma process, *University College Dublin Seminar*, 10-MAY-2008.

Bibliography

[1] Roth J R. *Inustrial Plasma Engineering : Volume 2 Applications to Nonthermal Plasma Processing.* Taylor and Francis, London, 2001.

[2] Fridman A A and Kennedy L A. *Plasma Physics and Engineering.* Taylor and Francis, New York, 2004.

[3] Roth J R, Rahel J, Dai X, and Sherman D M. The physics and phenomenology of One Atmosphere Uniform Glow Discharge Plasma (OAUGDP™) reactors for surface treatment applications. *J. Phys. D: Appl. Phys.*, 38:555, 2005.

[4] Chichina M, Hubicka Z, Churpita O, and Tichy M. Measurement of the Parameters of Atmospheric-Pressure Barrier-Torch Discharge. *Plasma Process. Polym.*, 2(6):501–506, 2005. ISSN 1612-8869.

[5] Hutchinson I H. *Principles of Plasma Diagnostics.* Cambridge University Press, New York, 1994.

[6] Langmuir I. Oscillations in ionized gases. *Proc. Nat. Acad. Sci. USA,*, 14(8):627, 1928.

[7] Fridman A A. *Plasma Chemistry.* Cambridge, New York, 2008.

[8] Roth J R. *Inustrial Plasma Engineering : Volume 1.* Taylor and Francis, London, 1995.

[9] Biederman H. *Plasma polymer films.* Imperial College Press, 2004.

[10] Roth J R. Potential industrial applications of the one atmosphere uniform glow discharge plasma operating in ambient air. *Phys. Plasmas*, 12(5):57103, May 2005.

[11] Kogelschatz U, Eliasson B, and Egli W. From ozone generators to flat television screens: history and future potential of dielectric-barrier discharges. *J. Pure and Appl. Chem.*, 71(10):1819–1828, 1999.

[12] Lieberman M A and Lichtenberg A J. *Principles of Plasma Discharges and Materials Processing.* Wiley, New Jersey, second edition, 2005.

[13] Kunhardt E E. Generation of large-volume, atmospheric-pressure, nonequilibrium plasmas. *IEEE Trans. Plasma Sci.*, 28(1):189–200, 2000.

[14] Raizer Yu P. *Gas Discharge Physics.* Springer-Verlag, Berlin, 1991.

[15] Braithwaite N S J. Introduction to gas discharges. *Plasma Sources Sci. Technol.*, 9:517, 2000.

[16] Raizer Y P, Shneider M N, and Yatsenko N A. *Radio-frequency capacitive discharges*. CRC Press, Boca Raton, 1995.

[17] Paschen F. Ueber die zum funkenübergang in luft, wasserstoff und kohlensäure bei verschiedenen drucken erforderliche potentialdifferenz. *Annalen der Physik*, 273(5):69–96, 1889.

[18] Meek J M. A theory of spark discharge. *Phys. Rev.*, 57(8):722–728, 1940.

[19] Loeb L B. Significance of formative time lags in gaseous breakdown. *Phys. Rev.*, 113(1):7–12, 1959.

[20] Palmer A J. A physical model on the initiation of atmospheric-pressure glow discharges. *Appl. Phys. Lett.*, 25:138, 1974.

[21] Okazaki S, Kogoma M, Uehara M, and Kimura Y. Appearance of stable glow discharge in air, argon, oxygen and nitrogen at atmospheric pressure using a 50 Hz source. *J. Phys. D: Appl. Phys.*, 26:889, 1993.

[22] Massines F et al. Experimental and theoretical study of a glow discharge at atmospheric pressure controlled by dielectric barrier. *J. Phys. D: Appl. Phys.*, 83:2950, 1998.

[23] Golubovskii Y B, Maiorov V A, Behnke J, and Behnke J F. Modelling of the homogeneous barrier discharge in helium at atmospheric pressure. *J. Phys. D: Appl. Phys.*, 36:39, 2003.

[24] Griem H R. Principles of plasma spectroscopy. *Proc. of the Phys. Soc.*, 1, 2005.

[25] Kogelschatz U. Dielectric-barrier discharges: Their history, discharge physics, and industrial applications. *Plasma Chem. Plasma Proc.*, 23 (1):1–46, 2003.

[26] Schutze A, Jeong J Y, Babayan S E, Park J, Selwyn G S, and Hicks R F. The atmospheric-pressure plasma jet: A review and comparison to other plasma sources. *IEEE Trans. Plasma Sci.*, 26(6):1685–1694, 1998. ISSN 0093-3813.

[27] Yokoyama T, Kogoma M, Moriwaki T, and Okazaki S. The mechanism of the stabilisation of glow plasma at atmospheric pressure. *J. Phys. D: Appl. Phys.*, 23:1125, 1990.

[28] Meng X, Zhang H, and Zhu J J. A general empirical formula of current–voltage characteristics for point-to-plane geometry corona discharges. *J. Phys. D: Appl. Phys.*, 41:065209, 2008.

[29] Eliasson B and Kogelschatz U. Modeling and applications of silent discharge plasmas. *IEEE Trans. Plasma Sci.*, 19(2):309–323, 2002.

[30] Neely W C, Newhouse E I, Clothiaux E J, and Gross C A. Decomposition of complex molecules using silent discharge plasma processing. *NATO ASI SERIES G ECOLOGICAL SCIENCES*, 34:309–309, 1993.

[31] Pochner K, Neff W, and Lebert R. Atmospheric pressure gas discharges for surface treatment. *Surf. Coat Technol.*, 74:394–398, 1995.

[32] Falkenstein Z. Frequency dependence of photoresist ashing with dielectric barrier discharges in oxygen. *J. Phys. D: Appl. Phys.*, 83:5095, 1998.

[33] Yagi S and Kuzumoto M. Silent discharges in ozonisers and CO2 lasers. *Austr. Jour. of Phys.*, 48:411, 1995.

[34] Kogelschatz U. Silent-discharge driven excimer UV sources and their applications. *Appl. Surf. Sci.*, 54:410–423, 1992.

[35] Weston G F. Gas discharge displays. *Physics in Technology*, 11:218, 1980.

[36] Kogelschatz U. Filamentary, patterned, and diffuse barrier discharges. *IEEE Trans. Plasma Sci.*, 30(4):1400–1408, 2003.

[37] Mangolini L, Anderson C, Heberlein J, and Kortshagen U. Effects of current limitation through the dielectric in atmospheric pressure glows in helium. *J. Phys. D: Appl. Phys.*, 37:1021, 2004.

[38] Radu I, Bartnikas R, and Wertheimer M R. Frequency and voltage dependence of glow and pseudoglow discharges in helium under atmospheric pressure. *IEEE Trans. Plasma Sci.*, 31(6 Part 2):1363–1378, 2003.

[39] Deng X T and Kong M G. Frequency range of stable dielectric-barrier discharges in atmospheric He and N_2. *IEEE Trans. Plasma Sci.*, 32(4): 1709–1715, 2004. ISSN 0093-3813.

[40] Shi J J and Kong M G. Mode transition in radio-frequency atmospheric argon discharges with and without dielectric barriers. *Applied Physics Letters*, 90:101502, 2007.

[41] Aldea E, Peeters P, De Vries H, and Van De Sanden MCM. Atmospheric glow stabilization. Do we need pre-ionization? *Surface and Coatings Technology*, 200(1-4):46–50, 2005. ISSN 0257-8972.

[42] Kanazawa S, Kogoma M, Moriwaki T, and Okazaki S. Stable glow plasma at atmospheric pressure. *J. Phys. D: Appl. Phys.*, 21:838, 1988.

[43] Massines F, Segur P, Gherardi N, Khamphan C, and Ricard A. Physics and chemistry in a glow dielectric barrier discharge at atmospheric pressure: diagnostics and modelling. 174:8–14, 2003. ISSN 0257-8972.

[44] Massines F, Gherardi N, Naude N, and Ségur P. Glow and Townsend dielectric barrier discharge in various atmosphere. *Plasma Phys. Contr. Fusion*, 47:B577, 2005.

[45] Maiorov V A and Golubovskii Y B. Modelling of atmospheric pressure dielectric barrier discharges with emphasis on stability issues. *Plasma Sources Sci. Technol.*, 16:S67, 2007.

[46] Golubovskii Y B, Maiorov V A, Behnke J, and Behnke J F. Influence of interaction between charged particles and dielectric surface over a homogeneous barrier discharge in nitrogen. *J. Phys. D: Appl. Phys.*, 35: 751, 2002.

[47] Shin J and Raja L L. Run-to-run variations, asymmetric pulses, and long time-scale transient phenomena in dielectric-barrier atmospheric pressure glow discharges. *J. Phys. D: Appl. Phys.*, 40:3145, 2007.

[48] Li M, Li C, Zhan H, Xu J, and Wang X. Effect of surface charge trapping on dielectric barrier discharge. *Appl. Phys. Lett.*, 92(3):031503, 2009. ISSN 0003-6951.

[49] Laroussi M and Akan T. Arc-free atmospheric pressure cold plasma jets: a review. *Plasma Process. Polym.*, 4(9):777–788, 2007. ISSN 1612-8869.

[50] Lu X P, Jiang Z H, Xiong Q, Tang Z Y, Hu X W, and Pan Y. An 11 cm long atmospheric pressure cold plasma plume for applications of plasma medicine. *Appl. Phys. Lett.*, 92:081502, 2008.

[51] Laroussi M and Lu X. Room-temperature atmospheric pressure plasma plume for biomedical applications. *Appl. Phys. Lett.*, 87(11):113902, 2009. ISSN 0003-6951.

[52] Laroussi M. Low-temperature plasmas for medicine? *IEEE Trans. Plasma Sci.*, 37(6):714–725, 2009. ISSN 0093-3813.

[53] Fridman G, Friedman G, Gutsol A, Shekhter A B, Vasilets V N, and Fridman A. Applied plasma medicine. *Plasma Process. Polym.*, 5(6): 503–533, 2008. ISSN 1612-8869.

[54] Kong M G, Kroesen G, Morfill G, Nosenko T, Shimizu T, Dijk J, and Zimmermann J L. Plasma medicine: an introductory review. *New J. Phys.*, 11:115012, 2009.

[55] Walsh J L and Kong M G. Contrasting characteristics of linear-field and cross-field atmospheric plasma jets. *Appl. Phys. Lett.*, 93(11):111501, 2009. ISSN 0003-6951.

[56] Teschke M, Kedzierski J, Finantu-Dinu E G, Korzec D, and Engemann J. High-speed photographs of a dielectric barrier atmospheric pressure plasma jet. *IEEE Trans. Plasma Sci.*, 33(2):310–311, 2005. ISSN 0093-3813.

[57] Karakas E, Koklu M, and Laroussi M. Correlation between helium mole fraction and plasma bullet propagation in low temperature plasma jets. *J. Phys. D: Appl. Phys.*, 43:155202, 2010.

[58] Li Q, Li J T, Zhu W C, Zhu X M, and Pu Y K. Effects of gas flow rate on the length of atmospheric pressure nonequilibrium plasma jets. *Appl. Phys. Lett.*, 95(14):141502, 2009. ISSN 0003-6951.

[59] Xiong Q, Lu X, Ostrikov K, Xiong Z, Xian Y, Zhou F, Zou C, Hu J, Gong W, and Jiang Z. Length control of He atmospheric plasma jet

plumes: Effects of discharge parameters and ambient air. *Physics of Plasmas*, 16:043505, 2009.

[60] Ye R and Zheng W. Temporal-spatial-resolved spectroscopic study on the formation of an atmospheric pressure microplasma jet. *Appl. Phys. Lett.*, 93:071502, 2008.

[61] Lu X P and Laroussi M. Dynamics of an atmospheric pressure plasma plume generated by submicrosecond voltage pulses. *Appl. Phys. Lett.*, 100:063302, 2006.

[62] Mericam-Bourdet N, Laroussi M, Begum A, and Karakas E. Experimental investigations of plasma bullets. *Journal of Physics D: Applied Physics*, 42:055207, 2009.

[63] Xiong Q, Lu X, Xian Y, Liu J, Zou C, Xiong Z, Gong W, Chen K, Pei X, Zou F, et al. Experimental investigations on the propagation of the plasma jet in the open air. *Journal of Applied Physics*, 107(7):073302, 2010. ISSN 0021-8979.

[64] Zhu W C, Li Q, Zhu X M, and Pu Y K. Characteristics of atmospheric pressure plasma jets emerging into ambient air and helium. *Journal of Physics D: Applied Physics*, 42:202002, 2009.

[65] Mangolini L, Orlov K, Kortshagen U, Heberlein J, and Kogelschatz U. Radial structure of a low-frequency atmospheric-pressure glow discharge in helium. *Appl. Phys. Lett.*, 80:1722, 2002.

[66] Martens T, Bogaerts A, Brok W J M, and van Dijk J. The influence of impurities on the performance of the dielectric barrier discharge. *Appl. Phys. Lett.*, 96:091501, 2010.

[67] Law V J, Milosavljević V, O'Connor N, Lalor J F, and Daniels S. Handheld Flyback driven coaxial dielectric barrier discharge: Development and characterization. *Rev. Sci. Instrum.*, 79:094707, 2008.

[68] Fairchild Semiconductors. LM555 timer datasheet, November 2002. URL `http://www.fairchildsemi.com/ds/LM%2FLM555.pdf`.

[69] International Rectifiers. IRF540 datasheet, March 2001. URL `http://www.irf.com/product-info/datasheets/data/irf540n.pdf`.

[70] Herbert C G and Johnstone R A W. *Mass spectrometry basics*. Boca Raton.

[71] Shenton M J. Adhesion enhancement of polymer surfaces by atmospheric plasma treatment. *J. Phys. D: Appl. Phys.*, 34:2754–2760, 2001.

[72] Hopfe V and Sheel D W. Atmospheric-pressure plasmas for wide-area thin-film deposition and etching. *Plasma Process. Polym.*, 4(3):253–265, April 2007.

[73] Yi C, Lee Y, Woo Kim D, and Yeom G. Characteristic of a dielectric barrier discharges using capillary dielectric and its application to photoresist etching. *Surf. Coat Technol.*, 163:723–727, 2003.

[74] Radu I, Bartnikas R, Czeremuszkin G, and Wertheimer M R. Diagnostics of dielectric barrier discharges in noble gases: atmospheric pressure glow and pseudoglow discharges and spatio-temporal patterns. *IEEE Trans. Plasma Sci.*, 31(3):411, 2003.

[75] Nersisyan G and Graham W G. Characterization of a dielectric barrier discharge operating in an open reactor with flowing helium. *Plasma Sources Sci. Technol.*, 13:582–587, 2004.

[76] Arkhipenko V I, Kirillov A A, Simonchik L V, and Zgirouski S M. Influence of the nitrogen–helium mixture ratio on parameters of a self-sustained normal dc atmospheric pressure glow discharge. *Plasma Sources Sci. Technol.*, 14:757, 2005.

[77] Twomey B, Rahman M, Byrne G, Hynes A, O'Hare L A, O'Neill L, and Dowling D P. Effect of plasma exposure on the chemistry and morphology of aerosol-assisted, plasma-deposited coatings. *Plasma Process. Polym.*, 5(8):737–744, 2008.

[78] Ramamoorthy A, Rahman M, Mooney D A, Don MacElroy J M, and Dowling D P. Thermal stability studies of atmospheric plasma deposited siloxane films deposited on Vycor™ glass. *Surf. Coat Technol.*, 202(17): 4130–4136, 2008.

[79] Manley T C. The electric characteristics of the ozonator discharge. *Trans. Electrochem. Soc*, 84(1):83–95, 1943.

[80] Falkenstein Z and Coogan J J. Microdischarge behaviour in the silent discharge of nitrogen-oxygen and water-air mixtures. *J. Phys. D: Appl. Phys.*, 30:817, 1997.

[81] Boyers D G and Tiller W. Plasma bubble domains: a magnetic bubble analog. *Appl. Phys. Lett.*, 41(1):28–31, 1982.

[82] Muller L, Punset C, Ammelt E, Purwins H G, and Boeuf J P. Self-organized filaments in dielectric barrier glow discharges. *IEEE Trans. Plasma Sci.*, 27(1):20–21, 1999.

[83] Yu Q S and Yasuda H K. An optical emission study on expanding low-temperature cascade arc plasmas. *Plasma Chem. Plasma Process.*, 18 (4):461–485, 1998.

[84] Machala Z, Janda M, Hensel K, Jedlovskı I, Lestinska L, Foltin V, Martisovits V, and Morvova M. Emission spectroscopy of atmospheric pressure plasmas for bio-medical and environmental applications. *Journal of Mol. Spectr.*, 243(2):194–201, 2007.

[85] Luque J and Crosley D R. LIFBASE; Database and Spectral Simulation Program (Version2. 0. 53). *SRI International Report MP*, pages 99–009, 1999.

[86] Bibinov N K, Fateev A A, and Wiesemann K. On the influence of metastable reactions on rotational temperatures in dielectric barrier discharges in He-N2 mixtures. *J. Phys. D: Appl. Phys.*, 34:1819, 2001.

[87] Bibinov N K, Fateev A A, and Wiesemann K. Variations of the gas temperature in He/N2 barrier discharges. *Plasma Sources Sci. Technol.*, 10:579, 2001.

[88] Bell K L, Dalgarno A, and Kingston A E. Penning ionization by metastable helium atoms. *J. Phys. B: Atom. Mol. Phys.*, 1:18, 1968.

[89] Lee D, Park J M, Hong S H, and Kim Y. Numerical simulation on mode transition of atmospheric dielectric barrier discharge in helium-oxygen mixture. *IEEE Trans. Plasma Sci.*, 33(2 Part 3):949–957, 2005.

[90] Shin J and Raja L L. Dynamics of pulse phenomena in helium dielectric-barrier atmospheric-pressure glow discharges. *J. Appl. Phys.*, 94:7408, 2003.

[91] Zhang P and Kortshagen U. Two-dimensional numerical study of atmospheric pressure glows in helium with impurities. *J. Phys. D: Appl. Phys.*, 39:153, 2006.

[92] Akishev Y S, Dem'yanov A V, Karal'Nik V B, Pan'kin M V, and Trushkin N I. Pulsed regime of the diffusive mode of a barrier discharge in helium. *Plasma Physics Reports*, 27(2):164–171, 2001.

[93] Wang Y and Wang D. Influence of impurities on the uniform atmospheric-pressure discharge in helium. *Phys. Plasmas*, 12:023503, 2005.

[94] Martens T, Bogaerts A, Brok W J M, and Dijk J V. The dominant role of impurities in the composition of high pressure noble gas plasmas. *Appl. Phys. Lett.*, 92:041504, 2008.

[95] Stalder K R, Vidmar R J, Nersisyan G, and Graham W G. Modeling the chemical kinetics of high-pressure glow discharges in mixtures of helium with real air. *J. Appl. Phys.*, 99(9):093301, 2006. ISSN 0021-8979.

[96] Ricard A, Décomps P, and Massines F. Kinetics of radiative species in helium pulsed discharge at atmospheric pressure. *Surf. Coat Technol.*, 112(1-3):1–4, 1999. ISSN 0257-8972.

[97] Liu D X, Rong M Z, Wang X H, Iza F, Kong M G, and Bruggeman P. Main Species and Physicochemical Processes in Cold Atmospheric-pressure He+ O2 Plasmas. *Plasma Process. Polym.*, 2010. ISSN 1612-8869.

[98] Luo H, Liang Z, Wang X, Guan Z, and Wang L. Effect of gas flow in dielectric barrier discharge of atmospheric helium. *J. Phys. D: Appl. Phys.*, 41:205205, 2008.

[99] Gherardi N, Gouda G, Gat E, Ricard A, and Massines F. Transition from glow silent discharge to micro-discharges in nitrogen gas. *Plasma Sources Sci. Technol.*, 9:340, 2000.

[100] Hong S J, May G S, and Park D C. Neural network modeling of reac-

tive ion etching using optical emission spectroscopy data. *IEEE Trans. Semiconductor Manufacturing*, 16(4):598–608, 2003. ISSN 0894-6507.

[101] Shadmehr R, Angell D, Chou P B, Oehrlein G S, and Jaffe R. Principal component analysis of optical emission spectroscopy and mass spectrometry: Application to reactive ion etch process parameter estimation using neural networks. *J. Electrochem. Soc*, 139(3):907–914, 1992.

[102] González S, Vega J, Murari A, Pereira A, Ramírez J M, Dormido-Canto S, and J.E.T.E. Contributors. Support vector machine-based feature extractor for L/H transitions in JET. *Rev. Sci. Instrum.*, 81:10E123, 2010.

[103] Banwell C N and McCash E M. *Fundamentals of molecular spectroscopy.* McGraw-Hill London, 1966.

[104] Law V J, OConnor N, Twomey B, Dowling D P, and Daniels S. Visualization of atmospheric pressure plasma electrical parameters. In *Topics on Chaotic Systems: Selected Papers from Chaos 2008 International Conference*, page 204. World Scientific Pub Co Inc, 2009. ISBN 9814271330.

[105] Kleinbaum D G, Kupper L L, and Muller K E. *Applied regression analysis and other multivariable methods.* Duxbury Pr, 2007. ISBN 0495384968.

[106] Laher R R and Gilmore F R. Updated excitation and ionization cross sections for electron impact on atomic oxygen. *J. Phys. Chem. Ref. Data*, 19(1):277–305, 1990.

[107] Shashurin A, Shneider M N, Dogariu A, Miles R B, and Keidar M. Temporal behavior of cold atmospheric plasma jet. *Appl. Phys. Lett.*, 94:231504, 2009.

[108] O'Connor N and Daniels S. Passive and active acoustic diagnostics of atmospheric pressure plasma systems. In *37th EPS Conference on Plasma Physics*, page 2.309. Dublin City University, 2010.

[109] Revans R W. The Transmission of Waves Through an Ionized Gas. *Phys. Rev.*, 44(10):798–802, 1933.

[110] Morse P M C and Ingard K U. *Theoretical acoustics.* Princeton Univ Pr, 1986.

[111] Kortshagen U. On the use of dust plasma acoustic waves for the diagnostic of nanometer-sized contaminant particles in plasmas. *Appl. Phys. Lett.*, 71:208, 1997.

[112] Ingard U. Acoustic wave generation and amplification in a plasma. *Phys. Rev.*, 145(1):41–46, 1966.

[113] Galechyan G A and Mkrtchyan A R. Acoustic wave amplification in a

plasma of a molecular gaseous discharge. *Acoust. Phys.*, 48(3):268–272, 2002.

[114] Ishii T and Inuishi Y. Amplification of neutral acoustic waves in gaseous plasmas. *Jap. J. Appl. Phys*, 8:1531–1534, 1969.

[115] Sakuntala M and Jain V K. Acoustic wave interaction with plasma. *J. Phys. D: Appl. Phys.*, 11:1925, 1978.

[116] Stepaniuk V, Tarau C, Otugen V, Sheverev V, Soukhomlinov V, and Raman G. Acoustic Wave Attenuation Through Glow Discharge Plasma. *AIAA paper*, 2433, 2002.

[117] Soukhomlinov V, Sheverev V A, and Tarau C. Reflection of sound by glow discharge plasma. *J. Phys. D: Appl. Phys.*, 39:3653, 2006.

[118] Bálek R, Pekárek S, and Bartáková Z. Power ultrasound interaction with DC atmospheric pressure electrical discharge. *Ultrasonics*, 44:e549–e553, 2006.

[119] Nakane T, Miyajima T, and Otsuka T. Current waveforms of electric discharge in air under high-intensity acoustic standing wave field. *Jpn. J. of Appl. Phys.*, 43(no. 5 b):2852–2856, 2004.

[120] Pekárek S and Bálek R. Ultrasound and airflow induced thermal instability suppression of DC corona discharge: an experimental study. *Plasma Sources Sci. Technol.*, 15:52, 2006.

[121] Pekárek S and Bálek R. Ozone generation by hollow-needle to plate electrical discharge in an ultrasound field. *J. Phys. D: Appl. Phys.*, 37: 1214, 2004.

[122] Tynan J, Law V J, Ward P, Hynes A M, Cullen J, Byrne G, Daniels S, and Dowling D P. Comparison of pilot and industrial scale atmospheric pressure glow discharge systems including a novel electro-acoustic technique for process monitoring. *Plasma Sources Sci. Technol.*, 19:015015, 2010.

[123] Chui C K. *An Introduction to Wavelets.* Elsevier Science, San Diego, 1992.

[124] Addison P S. *The Illustrated Wavelet Transform Handbook.* Institute of Physics Publishing, 2002.

[125] Stroud K A and Booth D J. *Advanced engineering mathematics.* Industrial Press, 2003.

[126] McGillem C D and Cooper G R. *Continuous and discrete signal and system analysis.* Saunders College Publications, 1991.

[127] Rossing T D. *Springer handbook of acoustics.* Springer Verlag, 2007. ISBN 0387304460.

[128] Nakamura T. *Flow-induced vibrations: classifications and lessons from practical experiences.* Elsevier Science Ltd, 2008. ISBN 0080449549.

[129] Cetegen B M and Kasper K D. Experiments on the oscillatory behavior of buoyant plumes of helium and helium-air mixtures. *Phys. fluids*, 8 (11):2974–2984, 1996. ISSN 1070-6631.

[130] Satti R P and Agrawal A K. Flow structure in the near-field of buoyant low-density gas jets. *International Journal of Heat and Fluid Flow*, 27 (2):336–347, 2006. ISSN 0142-727X.

[131] Yildirim B S and Agrawal A K. Full-field measurements of self-excited oscillations in momentum-dominated helium jets. *Exp. Fluids*, 38(2): 161–173, 2005. ISSN 0723-4864.

[132] Green D W and Perry R H. *Perry's Chemical Engineers' Handbook (8th Edition).* McGraw Hill, 2008. ISBN 0071542086.

[133] Fridman G, Brooks A D, Balasubramanian M, Fridman A, Gutsol A, Vasilets V N, Ayan H, and Friedman G. Comparison of Direct and Indirect Effects of Non-Thermal Atmospheric-Pressure Plasma on Bacteria. *Plasma Process. Polym.*, 4(4):370–375, 2007. ISSN 1612-8869.

[134] Prasad P N. *Nanophotonics.* Wiley-IEEE, 2004. ISBN 0471649880.

[135] Davies J. *Surface analytical techniques for probing biomaterial processes.* CRC, 1996. ISBN 0849383528.

[136] Nooney R I, Stranik O, McDonagh C, and MacCraith B D. Optimiza-

tion of plasmonic enhancement of fluorescence on plastic substrates. *Langmuir*, 24(19):11261–11267, 2008. ISSN 0743-7463.

[137] Weber N, Wendel H P, and Kohn J. Formation of viscoelastic protein layers on polymeric surfaces relevant to platelet adhesion. *J. Biomed. Mater. Res. Part A*, 72(4):420–427, 2005. ISSN 1552-4965.

[138] Unsworth L D, Sheardown H, and Brash J L. Protein resistance of surfaces prepared by sorption of end-thiolated poly (ethylene glycol) to gold: effect of surface chain density. *Langmuir*, 21(3):1036–1041, 2005.

[139] Nooney R, Clifford A, LeGuevel X, Stranik O, McDonagh C, and MacCraith B D. Enhancing the analytical performance of immunoassays that employ metal-enhanced fluorescence. *Anal. Bioanal. Chem.*, 396 (3):1127–1134, 2010. ISSN 1618-2642.

[140] Prasad P N. *Introduction to Biophotonics*. Wiley, 2003. ISBN 0471287709.

[141] Stranik O, Nooney R, McDonagh C, and MacCraith B D. Optimization of nanoparticle size for plasmonic enhancement of fluorescence. *Plasmonics*, 2(1):15–22, 2007. ISSN 1557-1955.

[142] Mendel C M and Mendel D B. 'Non-specific'binding. The problem, and a solution. *Biochem. J.*, 228(1):269, 1985.

[143] Magnusson M H, Deppert K, Malm J O, Bovin J O, and Samuelson L.

Gold nanoparticles: production, reshaping, and thermal charging. *J. Nanopart. Res.*, 1(2):243–251, 1999. ISSN 1388-0764.

[144] Zeonex Chemicals. Zeonor™. URL `http://www.zeonex.com/applications_bio-diagnostic.asp`.

[145] Haes A J and Van Duyne R P. A unified view of propagating and localized surface plasmon resonance biosensors. *Anal. Bioanal. Chem.*, 379(7):920–930, 2004. ISSN 1618-2642.

[146] Stoller P, V Jacobsen, and Sandoghdar V. Measurement of the complex dielectric constant of a single gold nanoparticle. *Opt Lett.*, 31(16):2474–2476, 2006. ISSN 0146-9592.

[147] Kingshott P, Wei J, Bagge-Ravn D, Gadegaard N, and Gram L. Covalent attachment of poly (ethylene glycol) to surfaces, critical for reducing bacterial adhesion. *Langmuir*, 19(17):6912–6921, 2003.